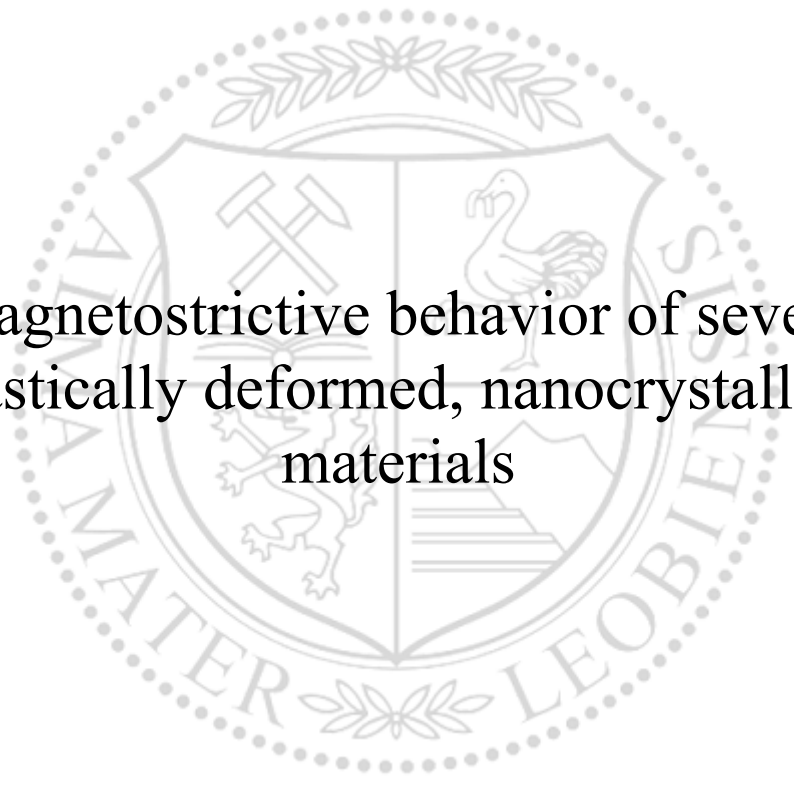Chair of Materials Physics

Master's Thesis

Magnetostrictive behavior of severe plastically deformed, nanocrystalline materials

Alexander Benedikt Paulischin, BSc

May 2021

MONTANUNIVERSITÄT LEOBEN
www.unileoben.ac.at

EIDESSTATTLICHE ERKLÄRUNG

Ich erkläre an Eides statt, dass ich diese Arbeit selbständig verfasst, andere als die angegebenen Quellen und Hilfsmittel nicht benutzt, und mich auch sonst keiner unerlaubten Hilfsmittel bedient habe.

Ich erkläre, dass ich die Richtlinien des Senats der Montanuniversität Leoben zu "Gute wissenschaftliche Praxis" gelesen, verstanden und befolgt habe.

Weiters erkläre ich, dass die elektronische und gedruckte Version der eingereichten wissenschaftlichen Abschlussarbeit formal und inhaltlich identisch sind.

Datum 19.05.2021

_____
Unterschrift Verfasser/in
Alexander Benedikt Paulischin

Acknowledgements

I want to thank Univ. Prof. Dr. Jürgen Eckert and Dr. Andrea Bachmaier for the supervision of my masters thesis.

I want to acknowledge the teamwork with Dr. Martin Stückler, Dipl.-Ing. Lukas Weissitsch, Dipl.-Ing. Michael Zawodzki and especially Dr. Stefan Wurster, who supported me throughout the theoretical and experimental part of this thesis.

In addition, I want to thank all colleagues, who work at the Erich-Schmid-Institute and supported me throughout this thesis. Especially, I want to thank Dipl.-Ing. Arthur Lintner for his assistance concerning the application of the strain gauges.

Furthermore I want to acknowledge the advices of Dr. Martin Kriegisch regarding the evolution of the experimental set-up for the magnetostriction measurements.

Kurzfassung

Die Änderung der Form eines Werkstoffes, die durch ein äußeres Magnetfeld hervorgerufen wird, wird als Magnetostriktion bezeichnet. Werkstoffe, die entweder einen großen oder sehr kleinen magnetostriktiven Effekt aufweisen, sind für bestimmte Anwendungen wünschenswert. Das Hauptaugenmerk dieser Arbeit lag auf der Untersuchung des magnetostriktiven Verhaltens in Abhängigkeit der chemischen Zusammensetzung der zwei Legierungssysteme Fe-Cu und Fe-Cr. Während eine niedrige Magnetostriktion für das System Fe-Cu erwartet wurde, wurde eine hohe Magnetostriktion für das System Fe-Cr vermutet. Pulvermischungen aus Fe und Cu mit nominellen Cu-Gehältern zwischen 5 at % und 30 at % sowie Mischungen aus Fe- und Cr-Granulat mit nominellen Cr-Gehältern von 30 at % bis 70 at % wurden zu festen Proben konsolidiert und anschließend mittels Hochdruck-Torsionsverfahrens (engl. High pressure torsion, HPT) verformt. Die Verformung mittels HPT führte zu außergewöhnlicher Kornfeinung und der Bildung einer nanokristallinen Mikrostruktur. Zusätzlich wurde die Formung übersättigter Mischkristalle erzielt. Die Magnetostriktionsmessungen wurden mithilfe eines neu errichteten Mess-Setups durchgeführt. Um die Genauigkeit dieses Setups zu bestimmen wurde das magnetostrictive Verhalten von Proben aus reinem, ferromagnetischen Co, Ni und Fe mit unterschiedlicher Mikrostruktur gemessen. Die Messwerte zeigten gute Übereinstimmung mit Literaturwerten. Im Falle des Systems Fe-Cu wurde ein Abfall der Beträge der magnetostriktiven Konstanten ermittelt. Im Vergleich zu reinem Eisen zeigte die Ergebnisse der Magnetostriktionsmessungen an Fe-Cr einen deutlichen Anstieg. Zur Messung des magnetostriktiven Verhaltens wurden zwei Messkonzepte verwendet. Die Probe wurde beim ersten Messkonzept entweder parallel, senkrecht oder in einem Winkel von 45° zum angelegten Magnetfeld ausgerichtet, welches während der Messung zwischen 0 T und 2.25 T variiert wurde. Im zweiten Messkonzept wurden die Proben in ein konstantes Magnetfeld von 2 T eingebracht und die Probenorientierung von 0° bis 180° in 10°-Schritten verändert. Neben der Messung des magnetostriktiven Verhaltens wurden mikrostrukturelle Untersuchungen aller Proben durchgeführt. Rasterelektronenmikroskopie, Röntgenbeugungsverfahren sowie Härtemessungen wurden zur Charakterisierung der Mikrostruktur durchgeführt.

Abstract

The change of a materials shape, which is caused by the application of an external magnetic field, is referred as magnetostriction. Materials exhibiting either a high or a very low magnetostrictive effect are desirable for certain applications. The focus of this thesis was the investigation of the magnetostrictive behavior of the two material systems Fe-Cu and Fe-Cr in dependence on their chemical composition. While for the Fe-Cu system a low magnetostrictive behavior was expected, a high magnetostriction was assumed in the case of Fe-Cr. Powder mixtures of Fe and Cu with a nominal Cu-content of 5 at % to 30 at % as well as mixtures of Fe- and Cr-flakes with a nominal Cr-content between 30 at % and 70 at % were consolidated into solid specimens and subsequently deformed using high pressure torsion (HPT). The HPT processing led to an exceptional grain refinement and the formation of a nanocrystalline microstructure. In addition, the formation of supersaturated solid solutions was achieved. The measurements of the magnetostrictive behavior were conducted using a newly built experimental set-up. To examine the accuracy of this set-up, the magnetostrictive behavior of specimens of pure ferromagnetic Co, Ni and Fe with different microstructural states were measured. The results of the magnetostriction measurements were compared with literature values and showed good agreement. In the case of the Fe-Cu system, a decrease of the absolute magnetostrictive constants was determined. Compared to pure Fe, the results of the magnetostriction measurements of the Fe-Cr system showed a significant increase. For the determination of the magnetostrictive behavior, two measurement concepts were used. In the first concept, the specimen was oriented either parallel, perpendicular or in an angle of 45° to the applied magnetic field. The magnetic field was varied between 0 T and 2.25 T during the measurement. In the second concept, a constant field of 2 T was applied while the specimen orientation was varied between 0° and 180° in steps of 10°. Besides the determination of the magnetostrictive behavior, a microstructural investigation of all specimens was conducted. Scanning electron microscopy, X-ray diffraction techniques and the determination of the specimen hardness were conducted for the characterization of the microstructure.

Contents

1 Introduction

When a material is exposed to an external magnetic field, a change of its shape occurs, which is referred as magnetostriction. Pure ferromagnetic materials typically exhibit a magnetostrictive behavior in the order of $10^{-5}\,\frac{\mu m}{m}$. Depending on the actual application, materials with either a low (e.g. in transformers) or a high (for actuation and sensing applications) magnetostriction are desirable. The focus of this thesis is on the influence of the chemical composition on the magnetostrictive behavior of the material systems Fe-Cu and Fe-Cr with the intention to investigate one material of either kind. While Fe-Cu is expected to show a small magnetostrictive response, the opposite should be the case for the Fe-Cr system.

The specimens of both material systems were processed by severe plastic deformation (SPD) prior to the determination of their magnetostrictive behavior. The SPD method high pressure torsion (HPT) gives the possibility to produce and process almost any desired material combination. Powders of the elemental materials are mixed in the desired ratio, compacted and deformed under high hydrostatic pressure. The processing by HPT can lead to a nanocrystalline (NC) microstructure and the formation of supersaturated solid solutions. Additional annealing treatments are conducted on some of the investigated specimens after HPT processing.

The viability and accuracy of the newly built measurement setup is tested by the determination of the magnetostrictive behavior of pure ferromagnetic materials with different microstructural states and the comparison of the results with literature values. Two concepts for the measurement of the magnetostrictive behavior are used for the investigation of all specimens. In the first concept, the specimen is oriented either parallel, perpendicular or at an angle of $45°$ to an applied magnetic field, which is varied between $0\,T$ and $2.25\,T$. Using the second concept, the orientation of the specimen in respect to the magnetic field is varied between $0°$ and $180°$ in a constant magnet field of $2\,T$.

In addition, a characterization of the microstructure is conducted on all specimens using scanning electron microscopy, measurement of the hardness as well as X-ray diffraction techniques.

2 Theory

2.1 Magnetostriction

A ferromagnetic material will change its shape when it is exposed to a magnetic field. The effect describing the change in material shape is called magnetostriction. Several magnetostrictive effects have been observed experimentally. A principal effect is the longitudinal extension or contraction of a material in a magnetic field, also known as Joule magnetostriction. As it is schematically illustrated in figure 2.1 (a), the length L of a material changes by the amount ΔL when a magnetic field H is applied. This change in length is described as a strain and is calculated according to equation (2.1). To distinguish it from a mechanical stress induced strain ϵ, this strain is marked with λ.

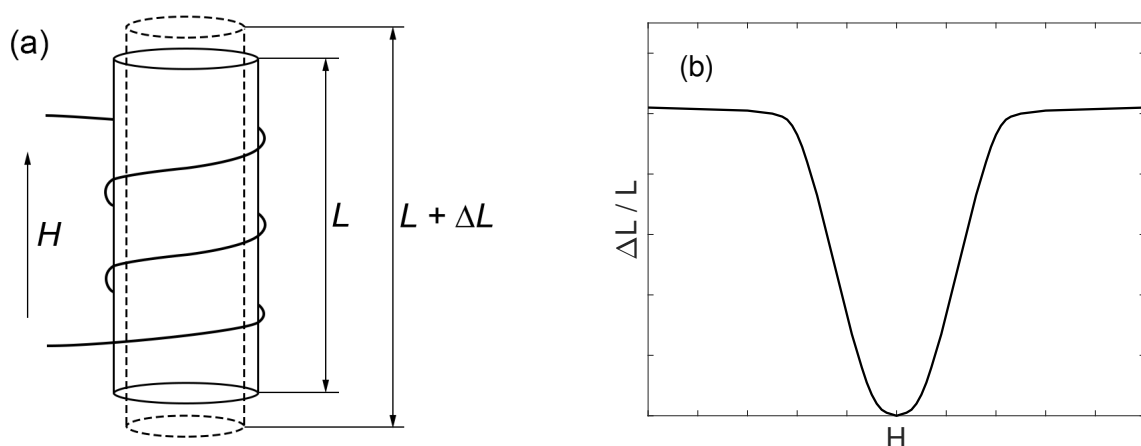$$\lambda = \frac{\Delta L}{L} \tag{2.1}$$

Figure 2.1: Schematic illustration of the magnetostrictive behavior of a material. (a) The material will change its length in the direction of the magnetic field. (b) Magnetostrictive strain λ vs. applied field H. The figure was redrawn according to[1].

While in the given example the material elongates in the direction of the applied magnetic field, it will contract in directions perpendicular to H and the volume of the material will remain constant. The strain $\lambda_\perp$ perpendicular to the applied magnetic field can be calculated according to equation (2.2).

$$\lambda_\perp = -\frac{1}{2} \cdot \lambda \tag{2.2}$$

The magnetostrictive strain λ of the material does not depend on the sign of H, as it is illustrated in figure 2.1 (b). So, a material will either expand or contract in the direction of the magnetic field, independent if a positive or a negative field is applied. Additionally, it is visible, that the value of the magnetostrictive strain depends on the magnitude of the applied field, especially for low fields[1–4].

In the following, the physical origin of the magnetostrictive behavior of polycrystalline materials shall be discussed briefly. As it is schematically illustrated in figure 2.2 (a), a material is in a disordered, paramagnetic state above the Curie temperature T_c. Spontaneous magnetization M_s will occur as the material is cooled down below T_c. Each domain will magnetize to its saturation and orient its magnetic moment in a direction of easy magnetization. The directions of easy magnetization are certain crystallographic directions, along which the magnetic moments of the atoms prefer to orient. This behavior is referred as crystal anisotropy, a kind of magnetic anisotropy. While each domain is magnetized to its saturation, the net magne-

Figure 2.2: Schematic illustration of the magnetostrictive behavior of para- and ferromagnetic materials. (a) The paramagnetic state above T_c. (b) Ferromagnetic state below T_c in the absence of a magnetic field. (c) Magnetostrictive saturation in the presence of a magnetic field H. The figure was redrawn according to[1].

tization of the material remains zero as long as no external magnetic field is applied. Within domains, the magnetic moments of unpaired, outer shell electrons tend to orient in the same direction. The outer electron orbitals of ferromagnetic materials are elongated in one direction with respect to other directions. As the spins and electron orbitals of all atoms within a domain are aligned in the same direction, which takes place due to spin-orbit coupling, the domain changes its length in the direction of the
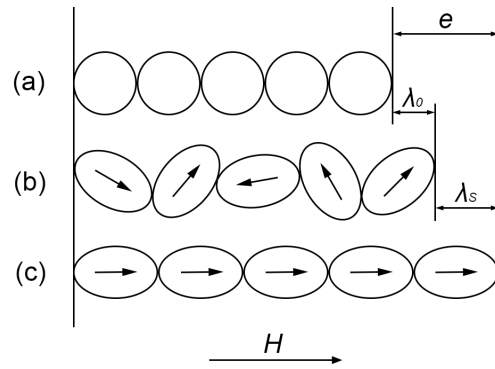
magnetic moment. As a consequence spontaneous mangetostriction λ_0 of the material occurs at zero field, as illustrated in figure 2.2 (b). Since the individual domains are aligned in various orientations, the spontaneous magnetostriction occurs homogeneously in all directions. Hence, the dimensions of the material change, but the shape remains the same.

The net magnetization of the material will increase when an external magnetic field is applied and the individual domains are aligned with the applied field by motion of their domain walls as well as rotation of the domains. All domains and hence all electron orbitals are aligned in the same direction when the saturation magnetization of the material is reached, as illustrated in figure 2.2 (c). The strain of the material at magnetic saturation is denoted as the saturation magnetostriction λ_s. The total strain e of the material, when it is brought from the paramagnetic state to magnetic saturation, is given by λ_0 and λ_s[1–4].

As mentioned before, the volume will remain constant while the material is strained magnetostrictively. This only is valid until saturation magnetization, and hence λ_s, is reached. When the magnetic field strength is increased beyond the saturation field, an additional magnetostrictive strain of the material occurs, as it can be seen in figure 2.3. This forced magnetostriction, which is proportional to H, causes either a small uniform expansion or contraction of the material in all directions. Due to its uniform character, a small volume change of the material occurs and the effect is also referred as volume magnetostriction[3,4].

Figure 2.3: Schematic illustration of the magnetostriction λ depending on the applied magnetic field strength H. The figure was redrawn according to[3].

Various crystal orientations are present in a polycrystalline material. Preferred grain orientation and textured microstructures have an influence on the magnetostrictive behavior as domains tend to orientate along directions of easy magnetization. Due to the various orientations of the individual domains, each domain will strain by a different amount than its neighbors, when an external magnetic field is applied. For cubic crystals, the saturation magnetostriction of a material with isotropic grain orientation can be estimated by averaging over all domain orientations by using equation (2.3). λ_{100} and λ_{111} are determined saturation magnetostrictions of the corresponding directions
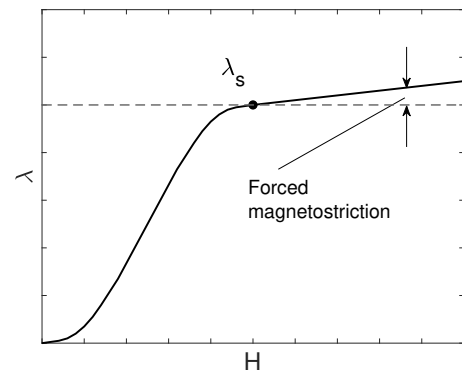
$\langle 100 \rangle$ and $\langle 111 \rangle$.

$$\bar{\lambda}_s = \frac{2}{5} \cdot \lambda_{100} + \frac{3}{5} \cdot \lambda_{111} \tag{2.3}$$

As the exact arrangement of domains has to be known for the application of equation (2.3), the determination of the saturation magnetostriction λ_s of a polycrystalline material can be determined in a second way. The magnetostriction at magnetic saturation is measured parallel to the magnetic field ($\lambda_{s\parallel}$) as well as perpendicular to the magnetic field ($\lambda_{s\perp}$). The saturation magnetostriction can be calculated using equation (2.4).

$$\lambda_s = \frac{2}{3} \cdot \left(\lambda_{s\parallel} - \lambda_{s\perp} \right) \tag{2.4}$$

The saturation magnetostriction of isotropic materials in a direction, that differs from the direction of the magnetic field by the angle θ, can be calculated according to equation (2.5)[1,3,4].

$$\lambda_s(\theta) = \frac{3}{2} \cdot \lambda_s \cdot \left(\cos^2 \theta - \frac{1}{3} \right) \tag{2.5}$$

For the ferromagnetic transition elements, the magnetostrictive effect is generally small and in the magnitude of 10^{-5}. Thermal expansion coefficients of these materials are in a range of 10 to $20 \cdot 10^{-6} \frac{1}{K}$. So small changes in the temperature can cause strains, that are in the magnitude of their magneotstrictive behavior[3].

2.1.1 Measurement of the magnetostrictive behavior

Several techniques can be used to measure the magnetostrictive behavior of a material. These methods can be generally classified in two groups: direct and indirect measurement methods. The length change of a material that is exposed to a magnetic field H, and thus the strain λ is measured directly by using a direct measurement technique. In contrast indirect measurement methods are based on the Villari effect, which describes the change in magnetization of a material due to application of a mechanical stress, and the strain λ is not measured directly. While direct techniques are suitable for the measurement of the material strain depending on the applied magnetic field, indirect methods are appropriate only for the determination of the saturation magnetostriction λ_s[1,2].

A strain gauge is an example for a direct measurement technique, that is commonly used to determine the magnetostrictive behavior of a material. Strain gauges are easy

to handle, but their sensitivity is limited to the range of 10^{-6}. As it is illustrated in figure 2.4 a strain gauge consists of a graticule usually made of constantan, which is embedded in a thin carrier film usually made of polyimide. The strain gauge gets cemented onto the specimen surface and is connected to a bridge circuit. As the specimen changes its shape, the graticule gets strained in the same way as the specimen. This straining causes a change in the electric resistance of the strain gauge, that is proportional to the applied stain. Since such resistance changes are very small, a Wheatstone bridge circuit is used to perform accurate measurements[2,3,5].

Commonly, commercially used strain gauges exhibit a magnetoresistive behavior. Their resistance changes depending on the applied magnetic field. To compensate the magnetoresistive behavior a second dummy gauge can be used, which is exposed to the same magnetic field, but not attached to the specimen. Both strain gauges are connected to a half bridge circuit and their signals are subtracted. When a magnetic field H is applied, the resistance of both gauges will change in the same way. But since the dummy gauge is not cemented onto the

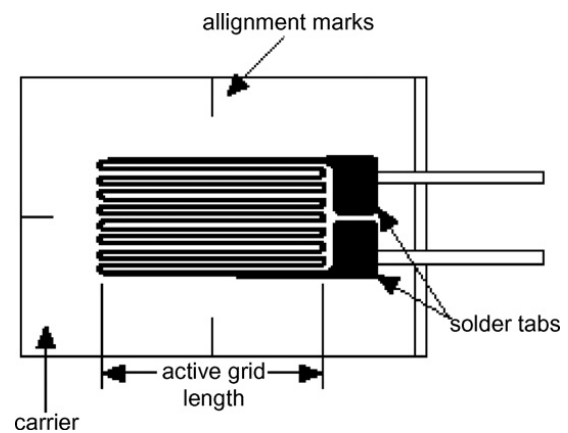

Figure 2.4: Illustration of a strain gauge. Reprinted from[2] with permission from Elsevier.

specimen, it will not experience a magnetostrictive straining. As a result the magnetoresistive changes of both gauges are compensated by the half bridge circuit and only the magnetostrictive behavior of the specimen is measured[2,3].

The usage of a half bridge circuit has another advantage. The resistance of a strain gauge graticule changes when a variation in temperature occurs. Although this change in resistance generally is small, it still is present and can affect the measurements. Additionally, temperature changes cause a thermal expansion of the specimen material as well as the graticule material. Since both materials usually exhibit different thermal expansion coefficient, they will undergo different length changes when a temperature change occurs. This difference of both length changes causes an additional, thermally induced straining of the strain gauge. The two thermally induced contributions of the measured strain signal can be compensated in the same way as the magnetoresistive behavior of the strain gauge graticule. The addition of a dummy strain gauge to a half bridge circuit, that undergoes the same temperature change as the active strain gauge, will cause a compensation of the thermal induced signals at both strain gauges.

Different batches of strain gauges exhibit slight variations in their sensitivity, which is indicated by the k-factor. The k-factor is provided with each batch of strain gauges. To ensure a proper compensation of the magnetoresistive and thermal effects, the strain gauges, that are used in a half bridge circuit, have to be taken from the same batch[5].

2.2 Severe plastic deformation

During the last decades an increasing interest in ultrafine-grained (UFG) and NC materials, their production and application as well as the improvements in their mechanical and physical properties can be observed. Bulk UFG and NC materials can be defined by their microstructure, especially by their grain size. While the average grain size of bulk UFG materials is below 1 μm, NC materials have grain sizes of less than 100 nm. Additionally, bulk UFG materials are defined by having a homogeneous microstructure and a high amount of high-angle grain boundaries[6–10].

To process UFG and NC materials two general approaches can be used, which differ from each other in the way how the microstructure is formed. By using "bottom-up" techniques, the microstructure of a material is built up from small building blocks, which are in the size of nanosized particles, or even atoms. Examples of "bottom-up" techniques are inert gas condensation or physical and chemical deposition methods. On the other side "top-down" techniques start with bulk materials with a coarse-grained microstructure. Due to the used processing techniques, the grains are refined down to sub-micrometer ranges, resulting in UFG and NC materials[7,8].

One of these approaches to process UFG and NC materials is severe plastic deformation (SPD). By using SPD methods, grain refinement and formation of the desired microstructure is achieved by application of a hydrostatic pressure on the bulk material and simultaneously imposing high shear strains. While the high strains are imposed on the material, the outer shape and the dimensions of the specimen do not change[7–9]. The application of SPD leads to an enhancement of certain mechanical and functional properties of the treated material. Some improvements of mechanical properties are an increase in strength with simultaneously good ductility, improved high-cycle fatigue behavior and enhanced formability by superplastic deformation[6–9]. Additionally, improvements of physical properties like excellent soft magnetic properties, enhancements in the kinetics of absorption and desorption of hydrogen and improved material strength with simultaneous improvements in electrical conductivity compared to conventional strengthened materials could be achieved[6,7,9,10]. Up to now, several methods of SPD processes like accumulative roll-bonding, equal-channel angular pressing, high pressure torsion (HPT) and multi-directional forging are available[7–10]. Due to

the fact that HPT was used for material processing of this thesis, this method will be discussed in more detail in the next section.

2.2.1 High pressure torsion

When a material is processed using HPT, the sample in the shape of a disc is placed within the cavities of two anvils and compressed by applying a high pressure in the order of several GPa. One of the two anvils rotates, which leads to torsional straining of the sample and in further consequence to grain refinement by dislocation accumulation and formation of new grain boundaries. To achieve an UFG or even NC microstructure several turns of the anvil have to be conducted. The schematic setup of an HPT is illustrated in figure 2.5.

The torsional strain γ, that is induced by the rotation of the anvil, is inhomogeneous across the sample cross-section, but follows a linear relation, which can be calculated using equation (2.6).

$$\gamma = \left(\frac{r}{t}\right) \cdot \phi \tag{2.6}$$

$$\epsilon = \frac{\gamma}{x} \tag{2.7}$$

According to equation (2.6) the strain γ in the midpoint of the sample is zero and rises linearly with increasing distance r from the center. Moreover, the achieved torsional strain γ depends on the thickness t of the sample and the torsional angle ϕ. According to equation (2.7) the equivalent strain ϵ can be calculated. For the coefficient x either values from a plastic flow criterion or from the Taylor theory for polycrystals are inserted. Typically x is set to be $\sqrt{3}$ for the von Mises criterion. Including equation 2.6 in equation 2.7 leads to equation 2.8, where n indicates the number of rotations.

$$\epsilon = \frac{2 \cdot \pi \cdot n \cdot r}{\sqrt{3} \cdot t} \tag{2.8}$$

Despite results of the calculations showing inhomogeneous straining of the microstructure across the sample diameter, experimental results reveal acceptable achieved homogeneous UFG/NC microstructures after a certain number of turns. An easy approach to prove microstructural homogeneity is by conducting hardness measurements along the radial cross-section of HPT deformed samples[8–12].

As mentioned above, SPD processes lead to a grain refinement and the formation of UFG and NC microstructures. Additionally, phase amorphization and the formation of metastable phases and supersaturated solid solutions can be achieved by the application of HPT[12].

Besides using coarse-grained bulk samples as starting materials, powder mixtures can be processed by HPT. The powder mixtures, which can be either precompacted to specimens before HPT processing or directly placed in the anvil cavities, are consolidated into dense, bulk materials with a NC microstructure. Depending on the initial metal system, a bigger variety of compositions is possible to be processed by using powders rather than using bulk starting materials. This is, because the combination of various metal systems is limited due to their sometimes low mutual solubility, which leads to miscibility gaps in these systems. The processing of systems, that show an immiscibility, by using conventional metallurgical casting is tricky or even impossible. HPT gives a way to synthesize bulk materials starting from powder mixtures, which, depending on the concentration of the initial metal powders, may result
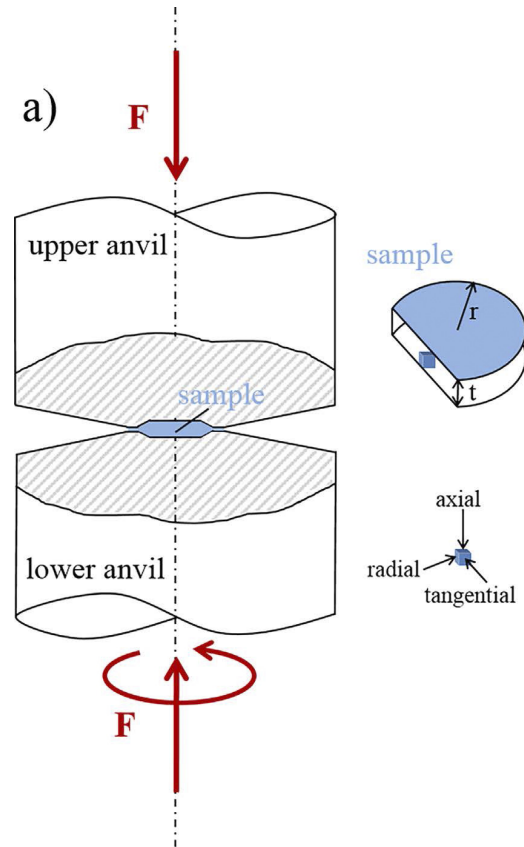

Figure 2.5: Schematic setup of an HPT[12]. The image was reproduced under the terms of the CC-BY 4.0 license ©2021, John Wiley & Sons.

in the formation of either an UFG supersaturated solid phase or supersaturated composites with a NC microstructure[11–13].

2.3 Scanning electron microscopy

A common method for characterization and image acquisition of microstructures is light microscopy. Due to the usage of visible light, whose wavelength ranges approximately from 400 nm to 700 nm, the resolution of structures is limited to this wavelength range, which makes light microscopy a suitable tool for preliminary investigations but impractical for the detailed characterization of NC materials. A way to overcome this

limitation in resolution is by the application of electron microscopy, where the signals generated by the interaction of a focused electron beam with the specimen are used for material characterization and imaging. With increasing applied voltage, which is used for the acceleration of electrons, their wavelength decreases and wavelengths down to several pm can be achieved. Besides a higher resolution also a high magnification range and a better focus depth can be achieved compared to light microscopy[14–16].

Two types of electron microscopes can be distinguished. Besides transmission electron microscopy, where a high-energetic electron beam is used to transmit a very thin specimen, a scanning electron microscope (SEM) is scanning and imaging the specimen surface line by line. A SEM consists of a column, in which electrons are emitted from a cathode and accelerated towards the specimen, and a vacuum chamber, in which a moveable specimen stage as well as signal detectors are placed. Electromagnetic lenses and apertures in the column are used for focusing, adjusting and scanning the electron beam over the specimen surface. To ensure that no interaction of electrons and gas molecules occurs, the pressure is reduced typically to 10^{-4} Pa inside the specimen chamber[15,16].

The interaction of the primary incident electron beam with the specimen causes several signals like backscattered electrons (BSEs), secondary electrons (SEs) or characteristic X-rays, which can be detected for image acquisition as well as for examination of the chemical composition of the specimen or specific microstructural areas. These signals originate from elastic and inelastic scattering processes, caused by the interaction of the primary electrons with the specimen. The scattering processes lead to a change of the incident electron trajectory and, in the case of inelastic scattering, a decrease of the primary electron energy due to energy transfer to the specimen. A schematic illustration of a scattering process is illustrated in figure 2.6 (a). The area, in which the scattering processes occur, is called the interaction volume, which can be seen in figure 2.6 (b). The size of the interaction volume depends on the acceleration voltage of the primary electron beam and the elements in the specimen and their concentration[16].

A BSE is a primary incident electron, which is scattered back out of the specimen due to scattering processes between the incident electron beam and matter. The amount of backscattered primary electrons depends on the atomic number, which represents the number of protons. An increasing proton number is leading to more BSEs and an increase of the measured signal. Due to the dependence of the electron yield on the atomic number, this so-called chemical contrast can be used to examine and image phase distributions within the microstructure. Not only the chemical contrast but also different crystal orientations can be detected, as the crystal orientation also influences the number of BSE´s. The detection of coherently scattered BSEs can be used to image
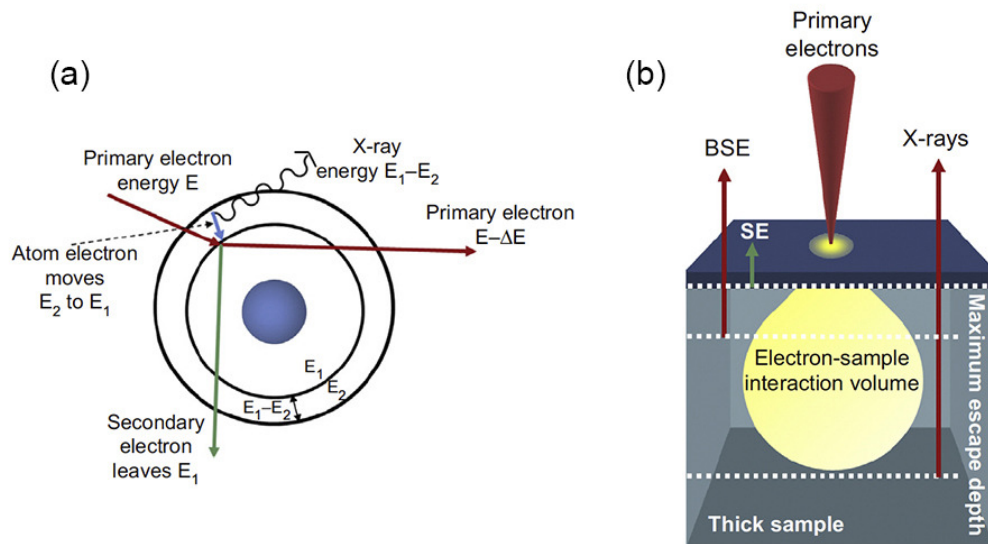
Figure 2.6: Schematic illustration of the interaction of incident electrons with matter. (a) Generation of BSEs, SEs and characteristic X-rays due to scattering processes. (b) Illustration of the interaction volume. Reprinted from[16] with permission from Elsevier.

the local structure and orientation of the crystals by electron backscatter diffraction (EBSD).

Another effect is used for imaging of the specimen topography. An electron, which is knocked out of its electron shell due to inelastic scattering processes, is called secondary electron. Commonly SEs exhibit energies of less than 50 eV and, due to these low energies, emerge from depths of less than 20 nm below the sample surface. This small escape depth, compared to other signals, is illustrated in figure 2.6 (b). The angle between the incident electron beam and the specimen surfaces affects the number of emitted SEs and as a result the intensity of the detected signal. Due to this dependence of the SE-intensity on the surface topography, the detection of SEs is used for high resolution image acquisition of the topography and shape of the specimen[15,16].

Besides SEs, inelastic scattering processes also cause the generation of characteristic and bremsstrahlung X-rays. While bremsstrahlung X-rays are generated due to a deceleration of incident primary electrons by the specimen atoms, characteristic X-rays are caused by a transition of electrons from higher to lower energy levels, which is illustrated in figure 2.6 (a). For such a transition, a spot for an electron in a lower shell with an energy E_1 has to be vacant. That vacancy can be generated by the incident primary electron knocking an electron out of its shell. A second electron, which transfers from its position in an outer shell (energy E_2) to the vacant spot in the inner shell causes the emission of an X-ray with a characteristic energy ($E_2 - E_1$). The energy only depends

on the difference of the shell energy levels and is characteristic for the corresponding element. The chemical composition of the specimen can be investigated by detecting the characteristic X-rays using energy dispersive X-ray analysis (EDX) or wavelength dispersive X-ray analysis (WDX). Parameters like the incident electron energy and the absorption of X-rays after generation have to be considered for a quantitative analysis of the specimen composition[15,16].

2.4 Hardness measurement

According to Martens, the hardness of a material is defined as the resistance against plastic deformation, which is caused by indentation with a harder material. To determine the hardness of a material several testing methods with static or dynamic force application have been developed. One of the methods with static force application is the Vickers hardness measurement, where a pyramid-shaped, square based diamond is used as an indenter. The tip of the pyramid has an angle of 136°. Depending on the applied force, a classification of the hardness measurements in categories like macro- and microhardness can be performed. The Vickers hardness HV of the tested material is determined by the applied force F divided by the surface A of the formed indent. During the indentation, the applied force is kept constant for a mandatory timespan. To determine the surface of the indent, the lengths of both indent diagonals after the indentation are measured and their mean value d is determined. According to equation (2.9) the indent surface can be calculated.

$$A = \frac{d^2}{\left[2 \cdot \sin\left(\frac{136}{2} \right) \right]} \tag{2.9}$$

With the calculated surface A, the measured hardness HV can be calculated using equation (2.10)[14,15].

$$HV = F \cdot 0.102 \cdot \frac{1}{A} \tag{2.10}$$

3 Experimental

3.1 Investigated materials and material systems

The investigated material systems can be differentiated into three groups. All compositions of group two and three in this thesis are given in atomic percent. To prevent contamination and oxidation, all used metal powders and flakes were stored and handled in a glovebox filled with Ar atmosphere.

In the first group pure elements were investigated. Bulk starting materials of the ferromagnetic elements Co, Ni and Fe were used for the specimen of group one. Besides bulk Fe-samples, Fe-powder (99.9 %, $-100 +200$ mesh, MaTeck) was used as a starting material for one HPT-deformed specimen. The HPT device was used for the compaction of the Fe-powder into a solid specimen prior to the deformation process. These elements have been selected to perform magnetostriction measurements using the newly designed experimental setup and a comparison of the results with literature values was made to ensure a proper measurement configuration.

Group two covers the Fe-Cu system, which exhibits a large miscibility gap at temperatures up to 600 °C. To extend the mutual solubilities, powders of Fe and Cu were used as starting materials and the specimen were processed by subsequent HPT-deformation[13]. Fe-powders (99.9 %, $-100 +200$ mesh, MaTeck) and Cu-powders (99.9 %, $-170 +400$ mesh, Alfa Aeser) were mixed in different ratios consisting of nominally 5 %, 15 % and 30 % Cu and 95 %, 85 % and 70 % Fe, respectively. The compaction of the Fe-Cu powder mixtures into solid specimen was conducted using the HPT device prior to the deformation process.

The third investigated system is the binary system of Fe and Cr. Mixtures of Fe-flakes and Cr-flakes with a nominal content of 30 %, 50 % and 70 % Fe (99.99 %, < 10 mm, HMW Hauner GmbH & Co. KG) and 70 %, 50 % and 30 % Cr (99.995 %, 1 mm – 25 mm, HMW Hauner GmbH & Co. KG), respectively, were arc melted (AM200 device Edmung Buehler GmbH) prior to the deformation treatment. 5 cycles of melting in Ar-atmosphere were performed. Discs with a diameter of 8 mm and a thickness of 1 mm were cut out of the arc melted Fe-Cr ingots and subsequently processed by HPT.

Polycrystalline W was used as material for the reference specimen in all magnetostric-

tion measurements. W was chosen because it is expected to exhibit a negligible small magnetostriction of less than $5 \cdot 10^{-3} \, \frac{\mu m}{m}$ at a magnetic field of 2284.3 mT[17,18].

3.2 HPT deformation

With the exception of the Co- and Ni-specimen as well as the W reference specimens, all specimens were deformed using HPT. The deformation parameters for HPT processing, depending on the respective material system and composition, are listed in table 3.1. All deformed specimens had a diameter of 8 mm. During the deformation processes pressures between 4 GPa and 7.5 GPa were applied. Between 10 and 100 revolutions were performed with a rotational frequency set between $0.6 \, \frac{1}{\min}$ and $1.2 \, \frac{1}{\min}$, depending on the respective specimen. In the case of the Fe-Cu system one-step deformation processes as well as two-step deformation process were accomplished. For the majority of the specimens a second deformation step at room temperature (RT) was performed after the first deformation step at elevated temperatures of 300 °C or 500 °C. During all deformation processes at RT, the anvils were cooled using compressed air to ensure, that the specimen temperature did not increase.

Besides the consolidation of metal powders into bulk specimen and the formation of an UFG microstructure, the application of HPT had an additional purpose. The aim was the formation of supersaturated solid solutions in the Fe-Cu and the Fe-Cr system by HPT processing. Depending on the initial concentrations of the elements, either single-phase supersaturated solid solutions or supersaturated composites consisting of two phases were formed.

In the case of one Fe sample, where a bulk starting material was used, and Fe-Cr samples of all investigated compositions, annealing treatments were conducted after HPT deformation. The as-deformed Fe sample was annealed at 650 °C for 1 h to form a well-defined globular microstructure with an average grain size of about 5 µm. Half discs of the as-deformed Fe-Cr samples were annealed for 1 h at 500 °C.

Table 3.1: Deformation parameter of all HPT deformed specimens. A two-step deformation process was used for the specimens marked with (*). The deformation parameters of the first and second step are listed in a separate line.

Nominal composition at. %	Initial material	Pressure GPa	Turns	Rotational speed $\frac{1}{min}$	Deformation temperature °C	Annealing parameter °C / h
Fe, No. 1	Bulk material	5	10	1.2	RT	
Fe, No. 2	Bulk material	5	10	1.2	RT	650 / 1
Fe, No. 3	Powder	7	20	1.2	RT	
$Fe_{95}Cu_5$, No. 1 *	Powder	4	50	1.2	500	
		5	50	1.2	RT	
$Fe_{95}Cu_5$, No. 2 *	Powder	4	50	1.2	500	
		5	50	1.2	RT	
$Fe_{85}Cu_{15}$, No. 1	Powder	5	100	1.2	300	
$Fe_{85}Cu_{15}$, No. 2 *	Powder	4	50	1.2	500	
		5	1	1.2	RT	
$Fe_{70}Cu_{30}$ *	Powder	4	50	1.2	500	
		5	50	1.2	RT	
$Fe_{70}Cr_{30}$, No. 1	Arc-melted ingot	7.5	22	0.6	RT	
$Fe_{70}Cr_{30}$, No. 2	Arc-melted ingot	7.5	22	0.6	RT	500 / 1
$Fe_{50}Cr_{50}$, No. 1	Arc-melted ingot	7.5	25	0.6	RT	
$Fe_{50}Cr_{50}$, No. 2	Arc-melted ingot	7.5	25	0.6	RT	500 / 1
$Fe_{30}Cr_{70}$, No. 1	Arc-melted ingot	7.5	22	0.6	RT	
$Fe_{30}Cr_{70}$, No. 2	Arc-melted ingot	7.5	22	0.6	RT	500 / 1

3.3 Microstructural characterization

For the specimens of group one and two, magnetostriction measurements and the characterization of the microstructure were performed on the same specimen. Different specimens with identical chemical composition and HPT processing route were used for the microstructural characterization of group three.

For the investigation of the microstructure, the HPT deformed specimens were cut in half using a diamond wire saw and embedded in resin for better handling. Additionally, specimens of coarse grained Co and Ni were embedded for microstructural characterization. After a metallographic preparation, scanning electron micrographs of the microstructure of Ni as well as of all HPT deformed samples were recorded. The image acquisition of all HPT deformed specimen was performed in tangential direction along the specimen radius in steps of $\Delta r = 1\,\text{mm}$. Image acquisition was conducted using a SEM (LEO 1525, Carl Zeiss Microscopy GmbH) in BSE mode. Additionally, images of the microstructure of Co were acquired using light microscopy. Measurements of the chemical composition were performed using EDX (XFlash 6|60 device, Bruker). Due to sample contamination, there is always a prominent carbon peak. Thus, carbon was not taken into account for chemical analysis. The grain size of the Fe specimen after the annealing treatment (650 °C, 1 h) was determined by EBSD using a Bruker e⁻ Flash^{FS} detector.

Measurements of the microhardness were conducted on the HPT deformed specimens to verify, that homogeneously deformed microstructures after HPT processing were obtained. The hardness measurements were conducted in tangential direction along the specimen radius in steps of $\Delta r = 0.25\,\text{mm}$ (Micromet 5102, Buehler). Mean values as well as their standard deviations of all validly measured hardness values in a range of $r = 2\,\text{mm}$ to $3.5\,\text{mm}$ of the specimen were determined.

To investigate the existing phases after HPT-deformation of the Fe-Cu system, XRD measurements were conducted for specimens of group two in axial orientation. The measurements were performed at least for one specimen of every chemical composition. In the case of the specimen composition $Fe_{70}Cu_{30}$, not the magnetostrictively measured specimen but a second specimen of identical HPT processing parameters was used for the XRD measurement. Before the measurement, the specimens´ surface were sanded with fine graded sand papers with mesh sizes of 1000 to 1200. The XRD measurements were conducted on a Bruker D2-Phaser using a Bragg-Brentano geometry and a Co-source with a wavelength of 178.897 pm. The measurements were conducted in a 2θ range of 45° to 105° with a step size of 0.2° and a measurement time of 3 s per step. During each measurement the specimen was rotated with a rotation velocity

of $15\,\frac{1}{\mathrm{min}}$. In the case of the Fe-Cr system synchrotron high-energy X-ray diffraction (HEXRD) experiments were performed at Deutsches Elektronen Synchrotron (DESY; Petra III Beamline P21.2) in Hamburg, Germany. Instead of the specimens used for magnetostriction measurements, specimens with identical chemical composition and HPT processing route were used for synchrotron experiments. The measurements were conducted in transmission mode with a spot size of $200\,\mu\mathrm{m}$ x $200\,\mu\mathrm{m}$ and a photon energy of $60\,\mathrm{keV}$. The diffraction patterns were captured by a VAREX XRD 4343 flat panel detector[19].

3.4 Magnetostriction measurements

The aim of this thesis was to build up a new measurement set-up and confirm its applicability with the measurement of pure ferromagnetic elements as well as the investigation of the magnetostrictive behavior of the two binary material systems Fe-Cu and Fe-Cr. Since these measurements were the main part of this thesis, the implementation and the measurement setup shall be discussed in more detail.

The magnetostrictive strain λ of the specimen, caused by the applied magnet field B, was measured using a strain gauge ($1 - LY11 - 0.6/120$, HBM), which was cemented onto the specimen surface with a $Z70$ instant glue from HBM. To enhance adhesion, the specimen surface was sanded with fine graded sand papers with mesh sizes of 1000 to 1200 and cleaned with isopropanol before the attachment of the strain gauge. Half discs of HPT deformed specimens were used for magnetostriction measurements. In the case of the specimen $Fe_{85}Cu_{15}$, No. 2, a full disc was used. To ensure, that the strain was measured in areas with a homogeneous microstructure, the strain gauge was positioned onto the specimen surface so that the graticule of the strain gauge was located at a radial distance of $1\,\mathrm{mm}$ to $2\,\mathrm{mm}$ from the specimen center. The positioning of the strain gauge in this way maximizes the adhesive area on the small specimen surface, while measuring at the largest possible radius. In the case of the undeformed specimen of Co and Ni the strain gauge was positioned in the specimen center since no deformation of the sample had occurred and the coarse microstructure was homogeneous throughout the whole specimen. The strain gauge leads were fixed at the specimen edges using a $X - 60$ glue from HBM to prevent motion and contact of the wires, which could lead to short circuits during the measurements. Figure 3.1 illustrates the specimen used for magnetostriction measurements of HPT deformed and annealed $Fe_{50}Cr_{50}$ with an attached strain gauge.

The measurements of the magnetostrictive behavior were performed using a Bruker B - E 30 electromagnet with conical pole pieces and a pole diameter of $176\,\mathrm{mm}$. Both
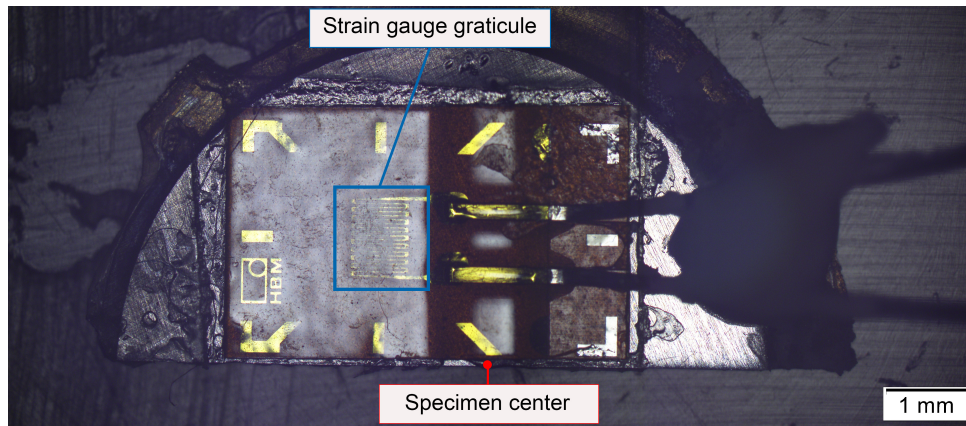
Figure 3.1: Illustration of the HPT deformed and annealed $Fe_{50}Cr_{50}$ specimen with an attached stain gauge.

poles were separated by an air gap of 50 mm. The electromagnet was actuated with a maximal current of 200 A, which results in a nominal magnet field of 2284.3 mT[18]. The actual measured maximal magnetic field was close to 2260 mT. The electromagnet was controlled by pre-programmed Scilab scripts (Version 6.0.3), in which a list of current values was defined. The Scilab scripts are listed in chapter 8.1. The magnetic fields, corresponding to the specified current values, were measured using a Model 475 DSP Hall-probe from Lakeshore, which was positioned within the air gap. The Scilab scripts, which controlled the actuation of the electromagnet, additionally were used for data acquisition of the measured magnetic fields.

Below the Hall-probe, a rotatable mount with a sample chamber was positioned in the air gap, in which the specimen as well as the reference specimen were encapsulated. A schematic illustration can be seen in figure 3.2. For each measurement, strain gauges of the same batch were cemented onto both samples. As it can be seen in figure 3.2, the initial specimen was positioned above the reference specimen and both samples were aligned with parallel strain gauges. Both strain gauges were connected to a half bridge circuit of a Wheatstone bridge and a Quantum^x MX410 amplifier from HBM was used to process the measured signals. For strain
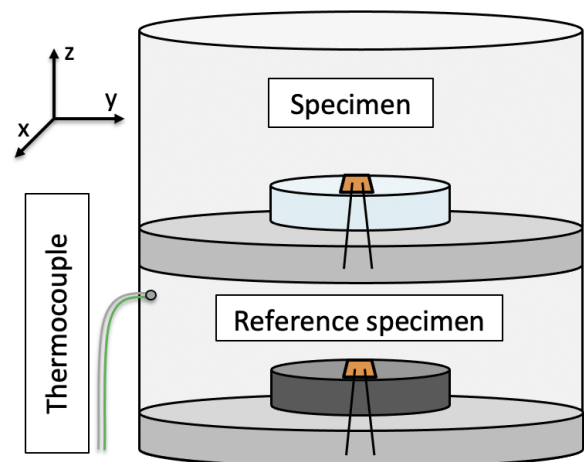
Figure 3.2: Schematic illustration of the specimen chamber and the alignment of the encapsulated specimen as well as the attached thermocouple.

gauge data acquisition the software CATMAN Easy V5.3 was used. The temperature inside the sample chamber was monitored using a Yocto-Thermocouple USB temperature sensor and a type-K thermocouple (Ni-Cr / Ni). For data acquisition of the temperature the software Spyder was used.

Two main concepts for the magnetostriction measurements were conducted. For the first concept the encapsulated specimens were oriented in certain positions with regard to the magnetic field lines. Both specimens were aligned in a way, that the strain gauge graticules were oriented either parallel, perpendicular or at an angle of 45° to the magnetic field lines, as it can be seen in figure 3.3 (a) – (c).

For each specimen orientation the electromagnet was actuated with the predefined list of current values and the measured data of the magnetic field B, the specimen strain λ as well as the temperature T were recorded over time t. For the first and last value in the predefined list a current was chosen, which corresponded to a magnetic field as close as possible to $0\,\text{mT}$. 150 measurements of B were conducted at each defined current value.

For the second concept the electromagnet was actuated with a constant current of $120\,\text{A}$, which corresponds to a magnetic field of approximately $2\,\text{T}$. As it is schematically illustrated in figure 3.3 (d) the orientation of the specimen was changed in steps of 10° between 0° and 180°. At each orientation of the specimen, the measured data of B, λ, T and t were acquired. Additionally, magnetostriction measurements at the angles of 45° and 135° were conducted. The number of measurements of the magnetic field, which were conducted at each specimen orientation, was extended to 200. In both concepts the strain was measured with a rate of $2\,\text{Hz}$ and the temperature was measured with a rate of approximately $1\,\text{Hz}$.
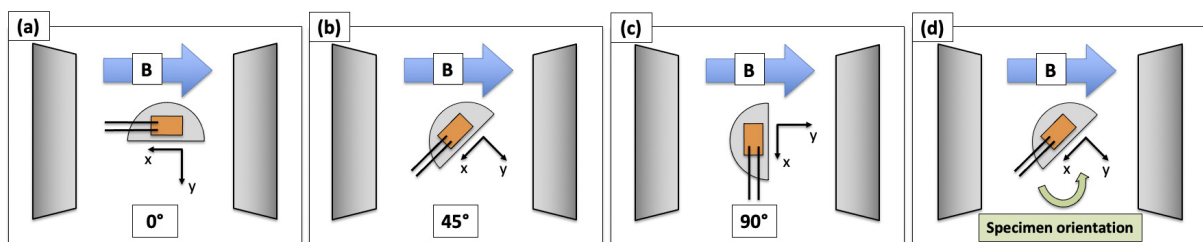
Figure 3.3: Schematic illustration of the specimen alignment during the magnetostriction measurement. (a) Parallel alignment of the specimen with the magnetic field. (b) Orientation of the specimen at an angle of 45°. (c) Perpendicular alignment of the specimen. (d) Varied specimen orientation at a constant magnetic field during the magnetostriction measurement.

Both concepts were applied to all three specimen groups. In the case of the measured pure elements and Fe-Cu specimens the current list, which was used in the first concept

to actuate the magnet field, contained only positive values. The measured specimen was magnetized by an increasing magnetic field up to approximately 2.26 T followed by a decrease of the magnetic field down to 0 mT. This means, that a ferromagnetic material, which was present in every specimen, experienced the initial magnetisation curve and the first part of a hysteresis loop. For the group containing the Fe-Cr alloys, the list of actuating currents was extended and the specimens experienced a full hysteresis loop. Due to the very long duration of these measurements, the magnetostriction measurements using the extended current list to actuate the electromagnet were only conducted for the orientations of 0° and 90°.

3.5 Data evaluation

The analysis of the measurements was conducted using the software MATLAB, version R2020a, in which some scripts for data evaluation were programmed. The scripts are listed in chapter 8.2.

The principle of the data evaluation shall be explained briefly. As mentioned in chapter 3.4, the data of the measured magnetic field, the strain of the specimen and the temperature were acquired over time for both measurement concepts. A schematic illustration of the measured data of B, λ and T over t is shown in figure 3.4. Since the acquisition of B, λ and T was conducted using three different programs, three data files with varying starting points and measurement rates were received after each measurement.

The recorded timeline corresponding to B is divided into individual time spans. During each time span, which lasted approximately 45 s, the electromagnet was actuated with a constant current. The mean values of all 150 measured values of the magnetic field were calculated for each time span and are represented by the red circles in figure 3.4 (a). To determine the corresponding values of λ and T, their timelines were compared with the first time point of each time span. The time values of both timelines (λ and T), which were showing the least deviation from the first time point of the time span of B, were chosen as starting points for the data evaluation of λ and T. The measured values of the strain and the temperature during the first 5 s after each starting point were disregarded and the values of λ and T of the following 30 s were averaged. The mean values of the strain and the temperature are represented by the blue and green circles in figure 3.4 (b) and (c). The reason, why the measured strain values of the first 5 s were disregarded, was to ensure, that the measured signal of the specimen strain reached a constant level after every actuation of the electromagnet with a new current. The same method was applied for the data evaluation of the temperature to determine the corresponding values. In addition to the averages of λ and T their

standard deviations for each time span were determined. As a result the mean values of B, λ and T corresponding to every current in the predefined list were obtained.

The data evaluation was slightly modified in the case of the second measurement concept. In addition to the acquired data of B, λ and T the angle of the specimen orientation was recorded. During each time span, the specimen chamber was positioned at a certain angle referring to the magnetic field. Since the number of measurements of B was extended to 200, the time span prolonged to almost 60 s. The mean value of all 200 measured values of the magnetic field was calculated for each time span. In the case of λ and T, the measured values of the first 5 s of each time span were disregarded, but the values of the following 45 s were averaged. As a result the mean values of B, λ and T corresponding to every specimen orientation were obtained.

To determine the saturation magnetostriction of each specimen, equation (2.4) was used. To calculate λ_s, the determined magnetostriction values at a specimen orientation of 0° and 90° were utilized as the magnetostriction at magnetic saturation parallel to the magnetic field $\lambda_{s\parallel}$ as well as perpendicular to the magnetic field $\lambda_{s\perp}$. The mean value as well as the corresponding standard deviation of all calculated saturation magnetostriction values above magnetic fields B of 1 T were determined for every specimen.

Figure 3.4: Schematic illustration of the measured data of: (a) the magnetic field B, (b) the specimen strain λ and (c) the temperature T over time t. The colored circles represent the calculated mean values of each time span.

The results of the second measurement concept were compared with measured magnetostriction values of the first measurement concept that were determined at the same current on the respective specimen orientations. In addition, the saturation magnetostriction depending on the specimen orientation $\lambda_s(\theta)$ was calculated using equation (2.5). The calculated values of $\lambda_s(\theta)$ were compared with the determined values of the second measurement concept. The saturation magnetostriction λ_s in equation (2.5) was

calculated by using mean values of the determined magnetostriction values of the first concept at 120 A of the specimen orientations of 0° and 90°.

3.5.1 Temperature compensation

Since the straining of the specimen that is caused by temperature differences can be of the same order of magnitude as the straining that is caused by a magnetic field, a compensation of temperature changes, which might have occurred during the conducted magnetostriction measurements, was seen as a beneficial part of the data evaluation. As mentioned in chapter 2.1.1, temperature changes during measurements can be compensated by the addition of a dummy strain gauge to a half bridge circuit. Yet, both strain gauges have to be attached to specimens with the same thermal expansion coefficient to ensure a proper temperature compensation. In this case a W-specimen was used to ensure a proper measurement of the magnetostrictive behavior and a compensation of the magnetoresistive behavior of the strain gauges. Due to the differences in thermal expansion, an additional compensation of thermal effects was implemented. The principle of the temperature compensation was the calculation of a strain difference $\Delta\lambda$ using the determined temperature differences ΔT and the thermal expansion coefficients α_s of the specimen as well as α_r of the reference specimen. Both specimens experienced a straining, depending on their respective thermal expansion coefficients, when a change of the temperature occurred. The strain gauges of the actual specimen and the reference specimen were connected to a half bridge circuit, as mentioned in chapter 3.4. Since the measured signal of the reference specimen was subtracted from the measured signal of the actual specimen, the resulting measured strain due to temperature differences depended on the difference $\Delta\alpha$ of both thermal expansion coefficients α_s and α_r, which was calculated according to equation (3.1).

$$\Delta\alpha = \alpha_s - \alpha_r \tag{3.1}$$

In the case of the investigated material systems of group two and three, the thermal expansion coefficient α_s for the temperature compensation was calculated according to equation (3.2) for each specimen, chemical composition respectively. Index 1 refers to Fe and index 2 refers to either Cu or Cr. Besides the thermal expansion coefficients α_1 and α_2 of both elements, their nominal concentrations x_1 and x_2 were used for the calculation.

$$\alpha_s = \alpha_1 \cdot x_1 + \alpha_2 \cdot x_2 \tag{3.2}$$

To compensate temperature changes, three methods were implemented in the MAT-LAB scripts. The principle of all three methods is schematically shown in figure 3.5. For all three methods, the determined mean values of T were used, which are shown in figure 3.5 as green circles.

In the first method, the temperature compensation is based on the determination of the temperature difference ΔT between a certain temperature mean value T_j and the previous averaged temperature T_i, which is schematically shown in figure 3.5 (a). This calculation of the temperature difference between two consecutive averaged temperatures was conducted for all determined mean values of the temperature T. As the first mean value of T was seen as the reference point for the temperature compensation, the temperature difference for this point was set to 0. For the second method, a quadratic function was fitted to all determined temperature mean values, representing the temperature trend during the measurement. A schematic illustration of this function can be seen in figure 3.5 (b). The calculated function values, which are illustrated by the black diamonds, were used for the determination of the temperature differences. Similar to the first method, the first calculated value of the function, corresponding to the first tem-

Figure 3.5: Schematic illustration of all methods for the temperature compensation. (a) Temperature compensation according to method one. (b) The second method of the temperature compensation, which used a fitted function. (c) Schematic illustration of the third method.

perature mean value, was seen as the reference point for the temperature compensation and its value was set to 0. For the determination of the values of ΔT, each calculated function values was compared with the reference function value and their difference was determined. The temperature compensation of the third method is based on the determination of ΔT, similar to the second method. Yet, for the calculation of a temperature difference, a certain averaged temperature T_j was compared with the first temperature mean value T_a, which is schematically illustrated in figure 3.5 (c). Equal

to the two other methods, this calculation was conducted for all determined temperature mean values.

3.5.2 Data presentation

The results of the magnetostriction measurements after data evaluation as well as the microstructural characterization are shown in the following chapter. For every specimen, the determined magnetostrictive behavior is presented in three graphs. In the first graph the results of the first measurement concept, which is schematically illustrated in figure 3.3 (a) – (c), are displayed. Figure two shows the results of the second measurement concept, which is schematically illustrated in figure 3.3 (d). As mentioned before, the red data points in each second figure illustrate the measured magnetostriction values, which were determined at a current of 120 A on the respective specimen orientations using the first measurement concept. The dashed black line illustrates the results of the calculated saturation magnetostriction depending on the specimen orientation $\lambda_s(\theta)$ using equation (2.5). In the third graph, the saturation magnetostriction λ_s is displayed, which was determined using equation (2.4). The mean value as well as the corresponding standard deviation of all calculated saturation magnetostriction values above magnetic fields of 1 T are listed.

Since the strain gauge graticules were positioned in a radial distance of 1 mm to 2 mm from the specimen center, scanning electron micrographs recorded at a radius of 2 mm are shown for the HPT deformed specimens. Additionally, images of the microstructure of Co and Ni are shown. With the exception fo Co and Ni, the mean values and their standard deviation of the measured hardness values are listed. In addition, results of the XRD measurements in the case of the Fe-Cu system as well as of the HEXRD measurements in the case of the Fe-Cr system are listed in the respective chapters.

4 Results and Discussion

As mentioned in the previous chapter, results of the measured magnetostricitve behavior as well as the microstructural characterization are presented. Three graphs are shown for every specimen, in which the results of the magnetostriction measurements are illustrated. Although methods for the temperature compensation, which are described in chapter 3.5.1, were implemented in the data evaluation, the as-measured results without any temperature compensation are illustrated in this chapter.

The results of each material group will be discussed at the end of the respective chapter. Values of the saturation magnetostriction are stated in two different forms in the literature, either in the form of λ_s or in the form of $\frac{3}{2}\lambda_s$ (see equation (2.4)). For the discussion of the measurement results all values of the saturation magnetostriction will be stated in the form of λ_s.

The results of the magnetostriction measurements of the Fe-Cr system using the first measurement concept form a part of a publication by Weissitsch et al.[19].

4.1 Results of pure elements

4.1.1 Co

The results of the magnetostriction measurements as well as an image of the microstructure of Co are shown below. The determined mean value of all saturation magnetostriction values above magnetic fields of $1\,\mathrm{T}$ was $-61\,\frac{\mu m}{m} \pm 0.5\,\frac{\mu m}{m}$. The chemical composition of the specimen, which was measured using EDX, only consisted of Co.
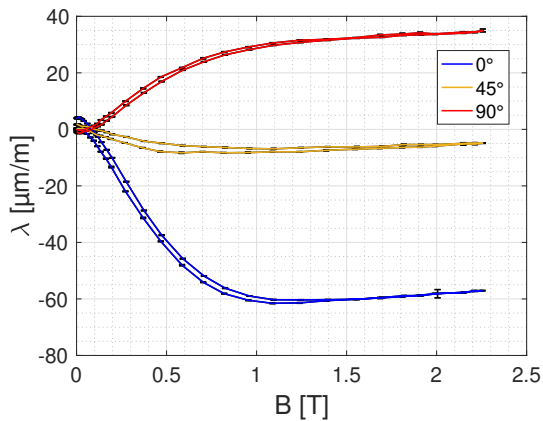
Figure 4.1: Measured magnetostrictive strain λ of Co for the specimen orientations of 0°, 45° and 90°.
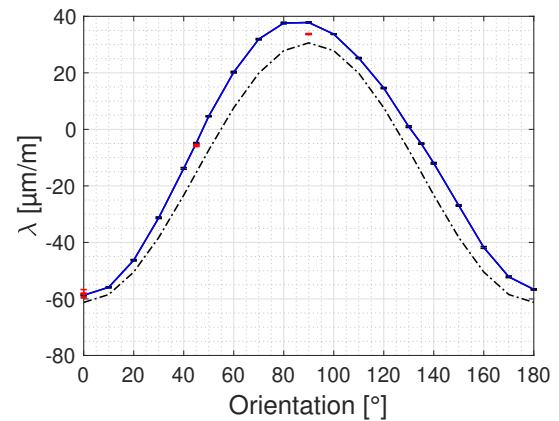
Figure 4.2: Measured magnetostrictive strain λ of Co of the second measurement concept.
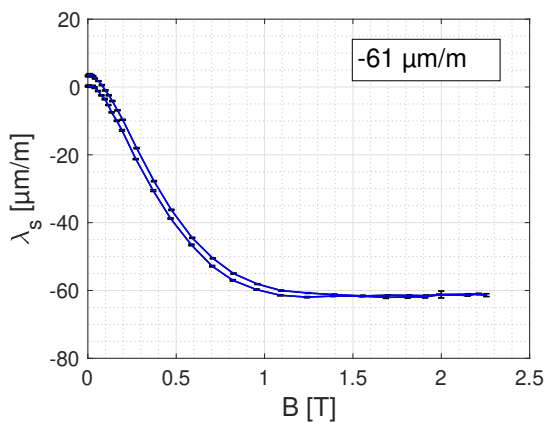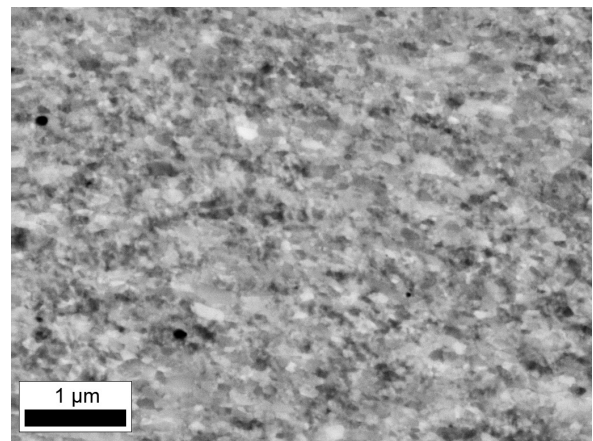

Figure 4.3: The calculated saturation magnetostriction λ_s of Co.

Figure 4.4: Image of the microstructure of Co.

4.1.2 Ni

The results of the magnetostriction measurements as well as a scanning electron micrograph of the Ni specimen are shown below. The determined mean value of all saturation magnetostriction values above magnetic fields of $1\,\mathrm{T}$ was $-39\,\frac{\mu m}{m} \pm 0.3\,\frac{\mu m}{m}$. The chemical composition of the specimen, which was measured using EDX, only consisted of Ni.
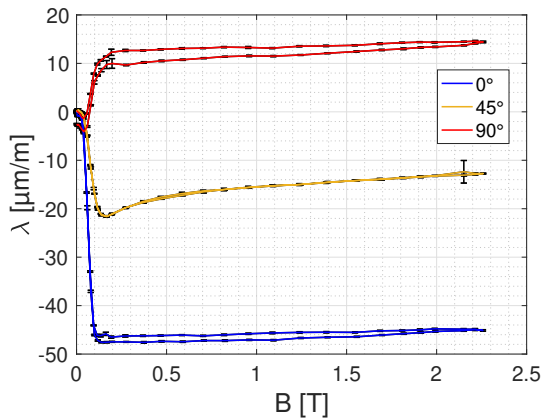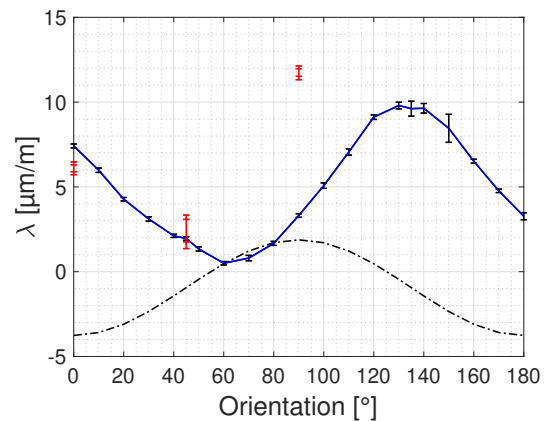

Figure 4.5: Measured magnetostrictive strain λ of Ni for the specimen orientations of 0°, 45° and 90°.
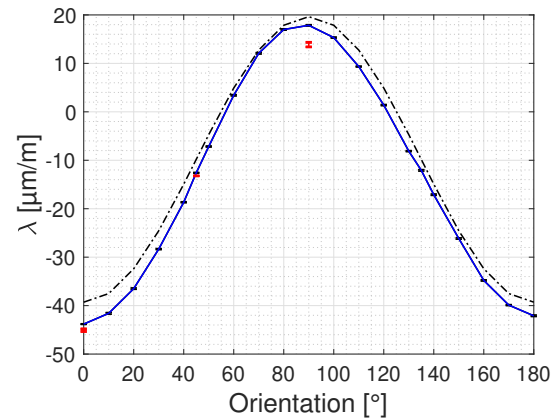
Figure 4.6: Measured magnetostrictive strain λ of Ni of the second measurement concept.
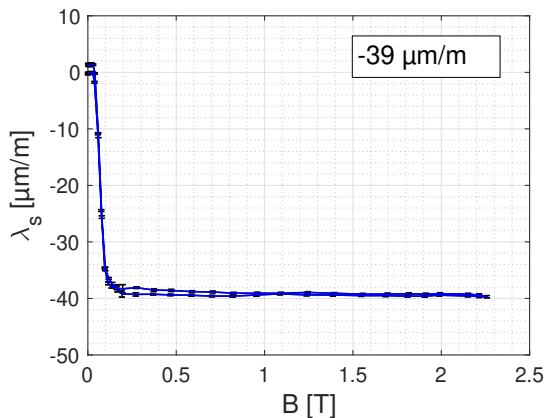
Figure 4.7: The calculated saturation magnetostriction λ_s of Ni.
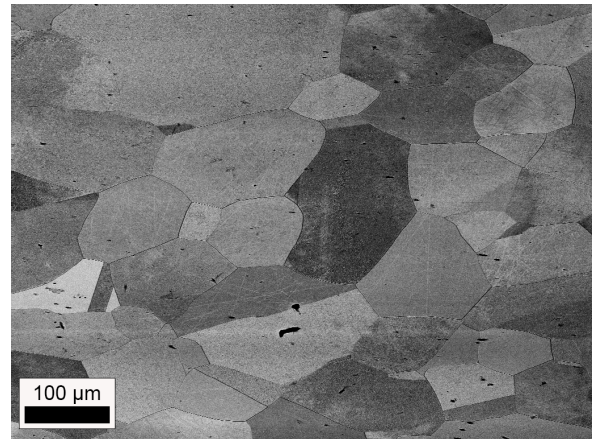
Figure 4.8: Image of the microstructure of Ni.

4.1.3 Fe, No. 1

The results of the magnetostriction measurements as well as a scanning electron micrograph of the **HPT deformed bulk Fe** specimen are shown below. The determined mean value of all saturation magnetostriction values above magnetic fields of 1 T was $-10\,\frac{\mu m}{m} \pm 0.2\,\frac{\mu m}{m}$. The average of the measured specimen hardness after deformation was $463\ HV0.5 \pm 4\ HV0.5$. The chemical composition of the specimen, which was measured using EDX, only consisted of Fe.
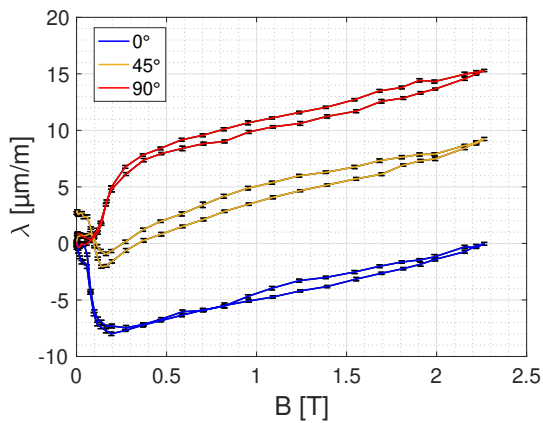
Figure 4.9: Measured magnetostrictive strain λ of HPT deformed bulk Fe for the specimen orientations of 0°, 45° and 90°.
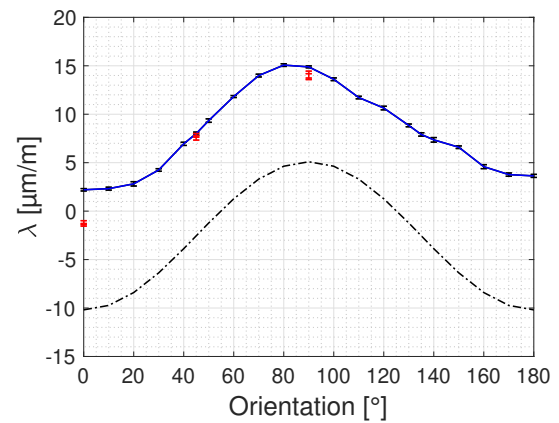
Figure 4.10: Measured magnetostrictive strain λ of HPT deformed bulk Fe of the second measurement concept.
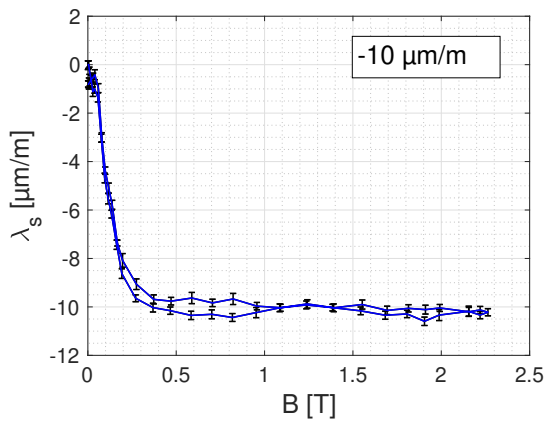
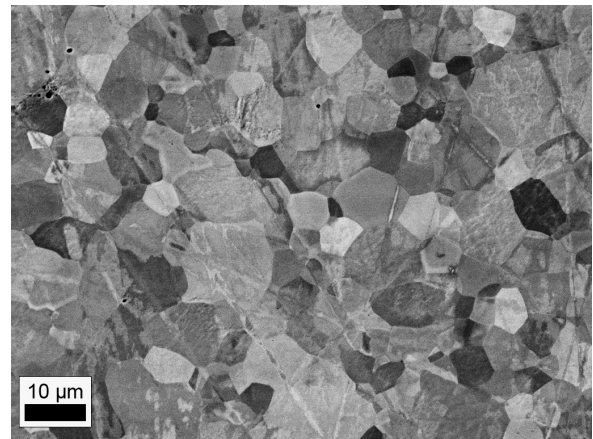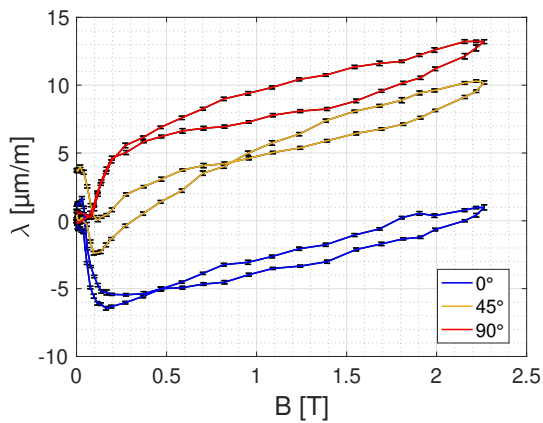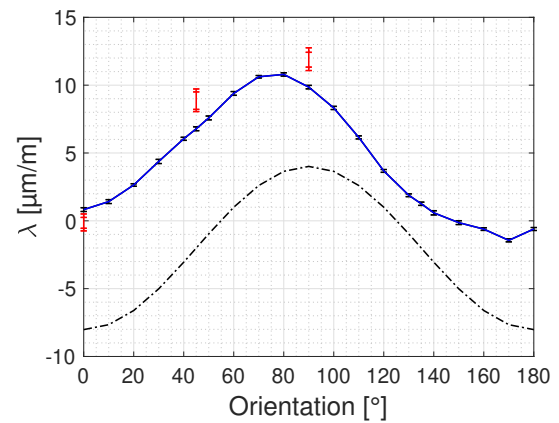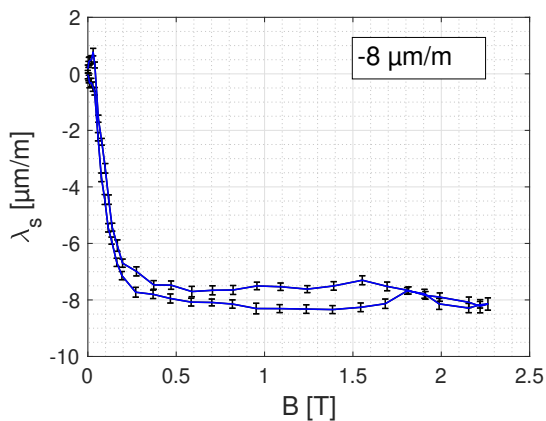Figure 4.11: The calculated saturation magnetostriction λ_s of HPT deformed bulk Fe.

Figure 4.12: Image of the microstructure of HPT deformed bulk Fe.

4.1.4 Fe, No. 2

The results of the magnetostriction measurements as well as a scanning electron micrograph of the **HPT deformed and annealed bulk Fe** specimen are shown below. The determined mean value of all saturation magnetostriction values above magnetic fields of 1 T was $-4 \frac{\mu m}{m} \pm 0.5 \frac{\mu m}{m}$. The average of the measured specimen hardness after deformation was 107 $HV0.1 \pm 5$ $HV0.1$. The chemical composition of the specimen, which was measured using EDX, only consisted of Fe.
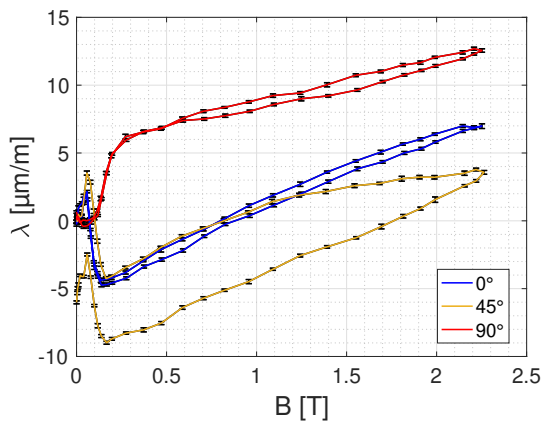
Figure 4.13: Measured magnetostrictive strain λ of HPT deformed and annealed Fe for the specimen orientations of 0°, 45° and 90°.

Figure 4.14: Measured magnetostrictive strain λ of HPT deformed and annealed Fe of the second measurement concept.
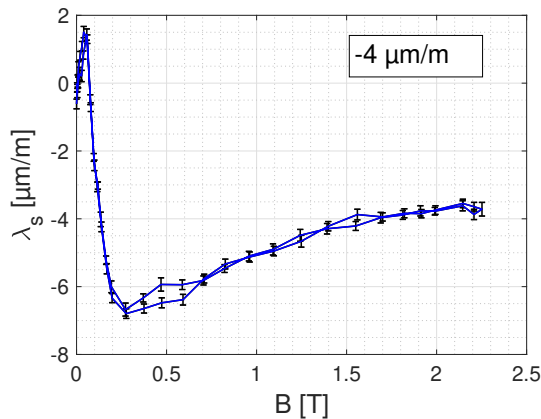
Figure 4.15: The calculated saturation magnetostriction λ_s of HPT deformed and annealed Fe.

Figure 4.16: Image of the microstructure of HPT deformed and annealed Fe.

4.1.5 Fe, No. 3

The results of the magnetostriction measurements as well as a scanning electron micrograph of the **HPT deformed Fe powder** specimen are shown below. The determined mean value of all saturation magnetostriction values above magnetic fields of 1 T was $-8\,\frac{\mu m}{m} \pm 0.4\,\frac{\mu m}{m}$. The average of the measured specimen hardness after deformation was $467\,HV0.5 \pm 10\,HV0.5$. The chemical composition of the specimen, which was measured using EDX, only consisted of Fe.

Figure 4.17: Measured magnetostrictive strain λ of HPT deformed Fe powder for the specimen orientations of 0°, 45° and 90°.

Figure 4.18: Measured magnetostrictive strain λ of HPT deformed Fe powder of the second measurement concept.

Figure 4.19: The calculated saturation magnetostriction λ_s of HPT deformed Fe powder.
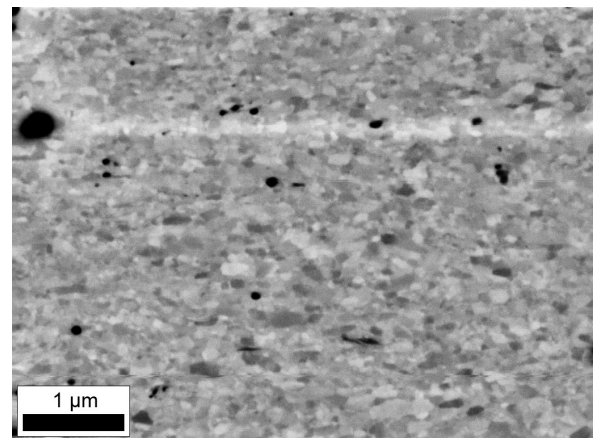
Figure 4.20: Image of the microstructure of HPT deformed Fe powder.

4.1.6 Discussion of the results of pure elements

The Co specimen exhibits a coarse grained microstructure, as shown in figure 4.4. The determined value of λ_s shows a very good accordance with a value found in literature. The determined mean value of $-61\,\frac{\mu m}{m}$ is almost identical with the literature value of $-62\,\frac{\mu m}{m}$[1]. The values of the strain, that were measured at a current of $120\,A$ using the first measurement concept (illustrated as red data points in figure 4.2), fit very well to the determined results using the second measurement concept. Furthermore, the calculated values of $\lambda_s(\theta)$, which are illustrated by the dashed black line, are in agreement with the measured values of the second concept.

In figure 4.21, the measured magnetostriction values of the specimen orientations of 0° and 90° are illustrated together with literature values of Co, which were measured at low magnetic fields[20]. As it is illustrated, the trend of the measured magnetostrictive behavior is parallel to the values stated in literature. Yet, the measured values do not align completely with the literature values. The measured magnetostriction values deviate from $0\,\frac{\mu m}{m}$ at magnetic fields of about $40\,mT$ to $60\,mT$ while the literature values start to differ from $0\,\frac{\mu m}{m}$ already at about $10\,mT$. A reason for this difference of the magnetostrictive behavior might be due
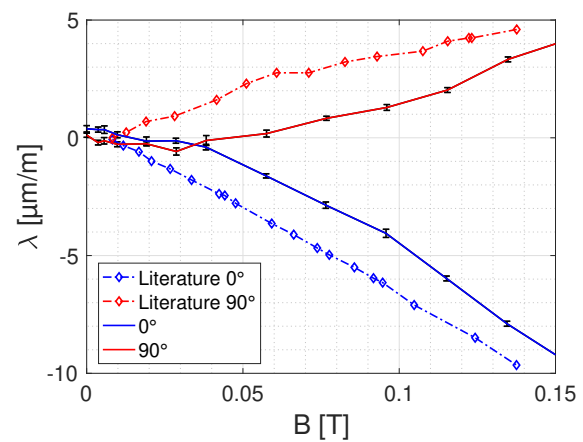

Figure 4.21: Comparison of measured magnetostrictive values of Co at low magnetic fields of the specimen orientations of 0° and 90° with literature values[20].

to a difference in specimen shape between the specimen used in this thesis and the ones used in literature. When figure 4.21 would be re-drawn not using the applied magnetic field but with the magnetic field inside the specimen as the new x-axis, it is expected that the measured results and the results stated in literature coincide in an even better way[20].

As illustrated in figure 4.8, the Ni specimen also exhibits a coarse grained microstructure. The magnetostrictive saturation for the specimen orientations of 0° and 90° is reached at very low magnetic fields between $100\,mT$ and $200\,mT$, as illustrated in figure 4.5. For Ni, a wide spectrum of the saturation magnetostriction can be found in literature, ranging from $-25\,\frac{\mu m}{m}$ to $-47\,\frac{\mu m}{m}$[3]. Differences in these values might arise from preferred grain orientations of the investigated specimens. Furthermore, resid-

ual stresses strongly influence the magnetic properties of Ni. The determined mean value of λ_s of $-39\,\frac{\mu m}{m}$ falls very well within the range of reported values. Although a wide range of the saturation magnetostriction is reported, usually accepted experimental values for λ_s of $-34\,\frac{\mu m}{m}$ and $-33.3\,\frac{\mu m}{m}$ are stated in literature, which show good agreement with the determined saturation magnetostriction of $-39\,\frac{\mu m}{m}$ [1,3]. Figure 4.6 illustrates the magnetostrictive behavior of Ni depending on the specimen orientation. The values determined using the first measurement concept at a current of 120 A as well as the calculated values of $\lambda_s(\theta)$ show a very good compliance with the measured magnetostriction values of the second concept.

Figure 4.22 illustrates a comparison of the measured magnetostriction values of the specimen orientations of 0° and 90° with literature values of Ni measured at low magnetic fields[21]. Although the results of the measurements show, that magnetostrictive saturation is reached for the specimen orientations of 0° and 90° at magnetic fields between 100 mT and 200 mT, a difference compared to the literature values is visible. The results reported in literature reach magnetic saturation below a magnetic field of 50 mT. Similar to the behavior of Co, the measured magnetostriction curves differ from $0\,\frac{\mu m}{m}$ between approximately 30 mT
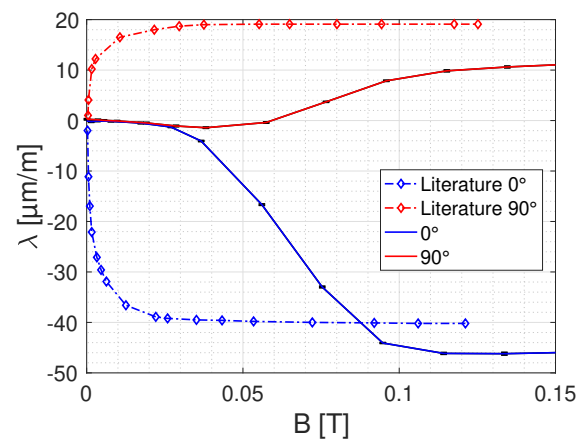

Figure 4.22: Comparison of measured magnetostrictive values of Ni at low magnetic fields of the specimen orientations of 0° and 90° with literature values[21].

and 60 mT, while the literature values deviate from $0\,\frac{\mu m}{m}$ already at smallest applied fields. Again, this difference is devoted to a different specimen shape. Additionally, the measured values of the strain at magnetic saturation do no match the literature values. Yet, the difference between both specimen orientations is approximately the same, when magnetic saturation is reached, yielding about the same saturation magnetostriction[21].

Magnetostriction measurements and an investigation of the microstructure were conducted on three different specimens in the case of Fe. Generally, the determined results of both HPT deformed specimens are similar while the results of the HPT deformed and annealed Fe specimen differ strongly.

The HPT deformed specimens Fe, No. 1 and Fe, No. 3 exhibit a NC microstructure,

as visible in the figures 4.12 and 4.20. The determined mean values of the measured hardness of both specimen show a very good agreement with almost identical mean values. The HPT deformed and annealed specimen Fe, No. 2 exhibits a coarse grained microstructure with an area weighted average grain size of 20 µm determined with EBSD, which is illustrated in figure 4.16. Due to recovery and recrystallization processes during the annealing treatment, a strong decrease of the measured hardness is visible. The determined mean value is 107 *HV*0.1.

The same magnetostrictive behavior is observable in all figures illustrating the results of the first measurement concept of Fe (4.9, 4.13 and 4.17). After magnetic saturation of the specimen is reached, a linear increase of the measured magnetostriction is visible, which occurs uniformly for all measured specimen orientations. It is suggested, that this linear increase is due to the volume magnetostriction of Fe. As it is illustrated in figure 2.3, the volume magnetostriction sits atop of the Joule´s magnetostriction saturation value. In the figures 4.11 and 4.19, indeed a constant saturation value is reached. The reason for the deviating behavior shown in figure 4.15 is not clear yet.

As visible in the figures that illustrate the results of the second measurement concept, an offset between the measured values of the second measurement concept and the calculated values for $\lambda_s(\theta)$ is present. This offset is seen as a consequence of the strong volume magnetostriction as this measurement concept involved measurements at an applied field of 2 T.

Although all three specimens show basically the same behavior of volume magnetostriction, it is recognizable, that the determined results of the HPT deformed and annealed Fe specimen (Fe, No. 2) show a different behavior compared to both HPT deformed Fe specimen (Fe, No. 1 and Fe, No. 3). As illustrated in figure 4.13, the magnetostriction measured at a specimen orientation of 45° is even below the magnetostriction measured at a specimen orientation parallel to the magnetic field. This behavior has not been observed yet for any other specimen. In addition, the slope of the measured magnetostriction at a specimen orientation of 0° is steeper than the measured magnetostriction at a specimen orientation of 90°, which results in an increasing saturation magnetostriction after the magnetic saturation of the specimen was reached, as it is illustrated in figure 4.15. The minimal value of λ_s reaches almost $-7\,\frac{\mu m}{m}$, which fits very good to the values $-7\,\frac{\mu m}{m}$ and $-9.3\,\frac{\mu m}{m}$ of λ_s found in literature and is in the same range as the saturation values of the two other two Fe-specimens[1,3]. Yet, due to the increasing saturation magnetostriction, the determined mean value of all saturation magnetostriction values above magnetic fields of 1 T is about $-4\,\frac{\mu m}{m}$, which is approximately half of the literature values.

The measured values of the second measurement concept differ from the calculated

values of $\lambda_s(\theta)$, as it is illustrated in figure 4.14. The measured values are not only shifted vertically, which can again be explained by the volume magnetostriction. Furthermore, the shape of the curve does not follow the *cos²*-relationship (equation (2.5)). This strong difference might be due to the presence of a preferred grain orientation. Preliminary EBSD-measurements (not presented within this thesis) give an indication of an increased strength of texture of the HPT deformed and annealed Fe-specimen in comparison to the as-deformed one. Furthermore, Renk et al. reported on different texture components but also an enhanced texture for fully recystallized Ta in comparison to the HPT deformed material[22]. The magnetostriction values of the first measurement concept measured at a current of 120 A agree very well with the results of the second measurement concept in the case of the specimen orientations of 0° and 45°. In the case of the values at a specimen orientation of 90° a difference between the results of the first and second measurement concept is visible.

In the case of both HPT deformed specimens, the determined saturation magnetostriction values are pretty similar. While for the HPT deformed bulk Fe specimen a mean value of $-10\,\frac{\mu m}{m}$ was measured, as illustrated in figure 4.11, the HPT deformed Fe powder specimen reaches a saturation magnetostriction mean value of $-8\,\frac{\mu m}{m}$, which is illustrated in figure 4.19. Both mean values fit very well to the values $-7\,\frac{\mu m}{m}$ and $-9.3\,\frac{\mu m}{m}$ reported in literature[1,3]. Both specimens exhibit a constant magnetostriction value after magnetic saturation is reached, as visible in the figures 4.11 for Fe, No. 1 and 4.19 for Fe, No. 3.

For both specimens, the results of the second measurement concept are illustrated in the figures 4.10 and 4.18. Both specimens show a good compliance with the values of the first measurement concept, that were measured at a current of 120 A. Although the measured magnetostriction values of both specimens show a similar behavior as the calculated values of $\lambda_s(\theta)$, a slight horizontal shift of the maximum curve value to a specimen orientation of 80° is recognizable, especially for the specimen Fe, No. 3. A reason for this shift may be a small misorientation of the specimen in the specimen chamber. Since the specimens are located inside the specimen chamber using a double-sided adhesive tape and additionally fixed with adhesive tape on top, a slight misorientation of the specimen during the assembly and small movements of the specimen during measurements cannot be excluded with certainty.

The comparison of the magnetostriction values of HPT deformed and annealed Fe at specimen orientations of 0° and 90° with literature values at low magnetic fields are illustrated in figure 4.23[21]. Generally, the measured magnetostriction values show a similar behavior as the literature values. Again, the magnetostriction values reported in the literature start to differ from $0\,\frac{\mu m}{m}$ at lower magnetic fields than the measured

magnetostriction values. Yet, a difference occurs in the case of the magnetostriction measured at a specimen orientation of 0°. The values decrease only to approximately the half of the values reported in literature[21].

Both non-annealed specimens exhibit a similar magnetostrictive behavior at low magnetic fields, which is illustrated in figure 4.24 for the specimen Fe, No. 1 and in figure 4.25 for the specimen Fe, No. 3 for the specimen orientations of 0° and 90°. Compared with literature values of Fe, a similar behavior is recognizable as for the specimen Fe, No. 2[21]. However, the magnetostriction values measured at a specimen orientation of 0° show a slightly different behavior. While the HPT deformed and annealed Fe shows an increase of the measured magnetostriction at magnetic fields of about 50 mT before the magnetostriction decreases, the measured values of both HPT deformed Fe specimens only show a decrease[21].
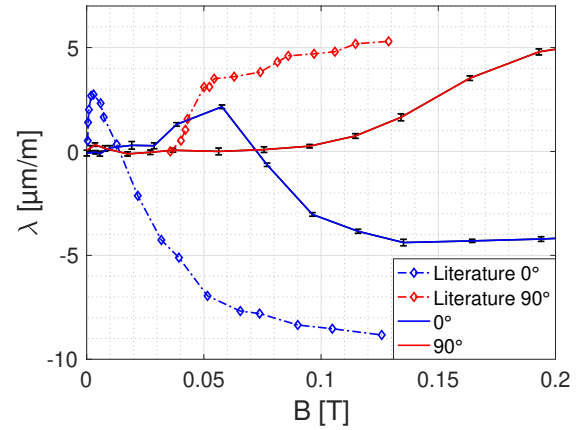
Figure 4.23: Comparison of measured magnetostrictive values of HPT deformed and annealed Fe at low magnetic fields of the specimen orientations of 0° and 90° with literature values[21].
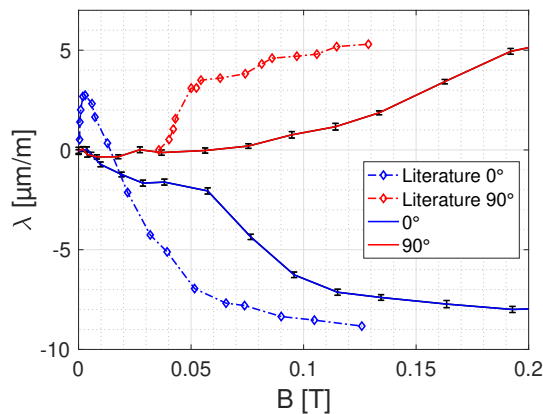
Figure 4.24: Comparison of measured magnetostrictive values of a HPT deformed bulk Fe specimen at low magnetic fields of the specimen orientations of 0° and 90° with literature values[21].
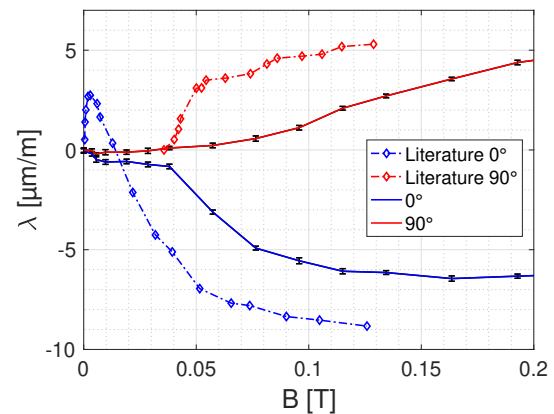

Figure 4.25: Comparison of measured magnetostrictive values of HPT deformed Fe powder at low magnetic fields of the specimen orientations of 0° and 90° with literature values[21].

4.2 Results for the Fe-Cu system

4.2.1 $Fe_{95}Cu_5$, No. 1

The results of the magnetostriction measurements as well as a scanning electron micrograph of the $Fe_{95}Cu_5$, No. 1 specimen are shown below. The determined mean value of all saturation magnetostriction values above magnetic fields of 1 T was $-3 \frac{\mu m}{m} \pm 0.3 \frac{\mu m}{m}$. The average of the measured specimen hardness after deformation was 549 $HV0.5 \pm$ 6 $HV0.5$. The averaged chemical composition of the specimen, which was measured using EDX, consisted of 94.4 % ±1.6 % Fe and 5.6 % ± 1.6 % Cu. The peak at 150° in figure 4.27 may have occurred due to a contact between the magnet pole and the strain gauge leads.
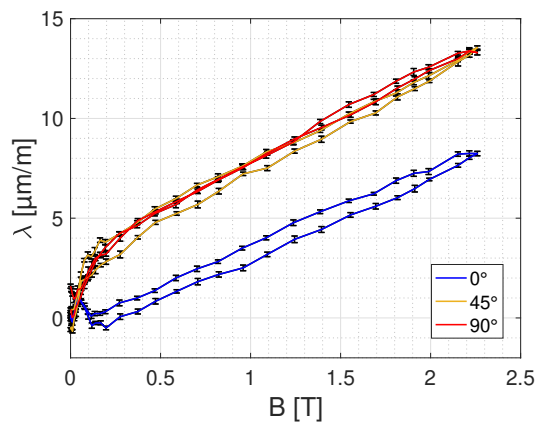
Figure 4.26: Measured magnetostrictive strain λ of $Fe_{95}Cu_5$, No. 1 for the specimen orientations of 0°, 45° and 90°.
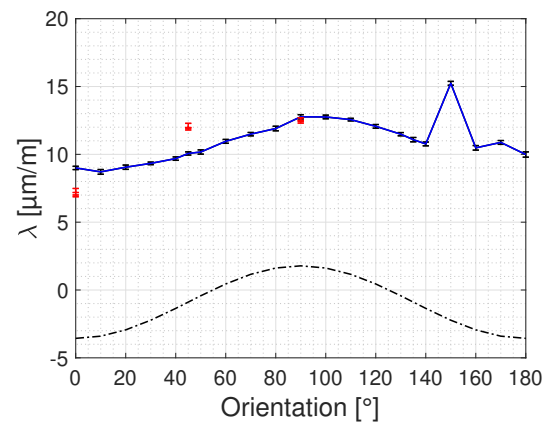
Figure 4.27: Measured magnetostrictive strain λ of $Fe_{95}Cu_5$, No. 1 of the second measurement concept.
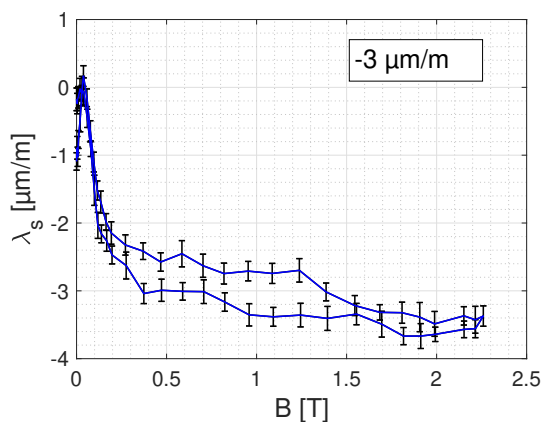

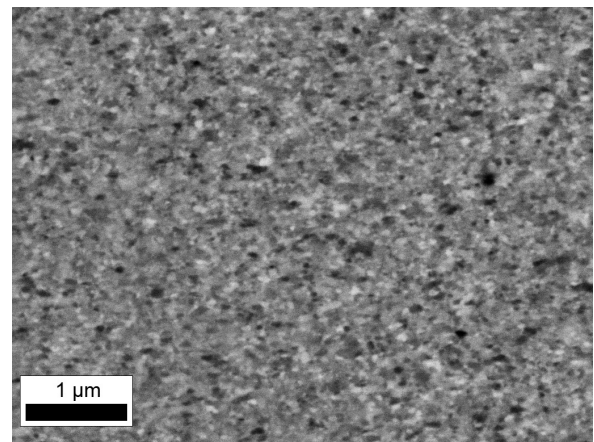Figure 4.28: The calculated saturation magnetostriction $λ_s$ of $Fe_{95}Cu_5$, No. 1.

Figure 4.29: Image of the microstructure of $Fe_{95}Cu_5$, No. 1.

4.2.2 Fe₉₅Cu₅, No. 2

The results of the magnetostriction measurements as well as a scanning electron micrograph of the Fe₉₅Cu₅, No. 2 specimen are shown below. The determined mean value of all saturation magnetostriction values above magnetic fields of 1 T was $-2\,\frac{\mu m}{m} \pm 0.4\,\frac{\mu m}{m}$. The average of the measured specimen hardness after deformation was 556 $HV0.5 \pm$ 23 $HV0.5$. The averaged chemical composition of the specimen, which was measured using EDX, consisted of 91.8 % ± 2.6 % Fe and 8.2 % ± 2.6 % Cu.
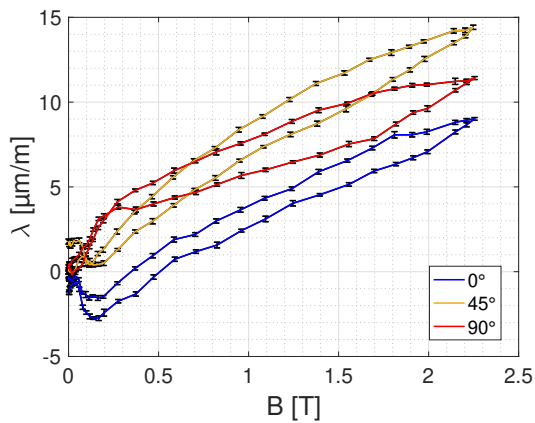

Figure 4.30: Measured magnetostrictive strain λ of Fe₉₅Cu₅, No. 2 for the specimen orientations of 0°, 45° and 90°.
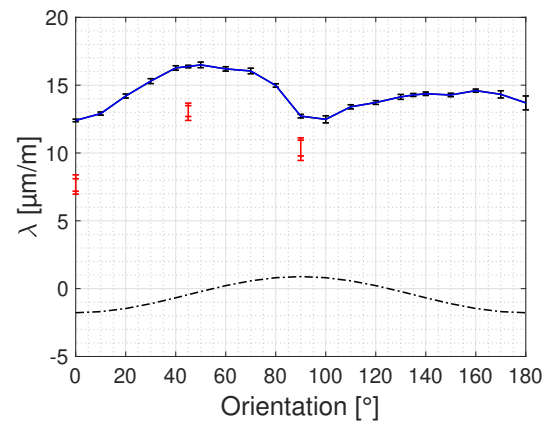

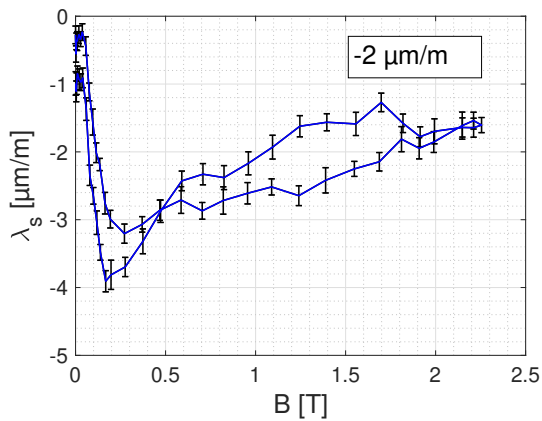Figure 4.31: Measured magnetostrictive strain λ of Fe₉₅Cu₅, No. 2 of the second measurement concept.

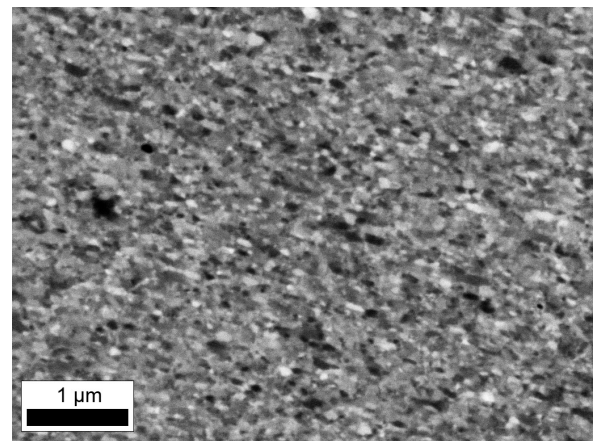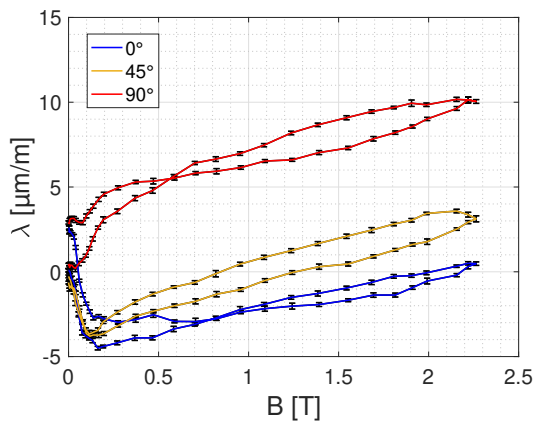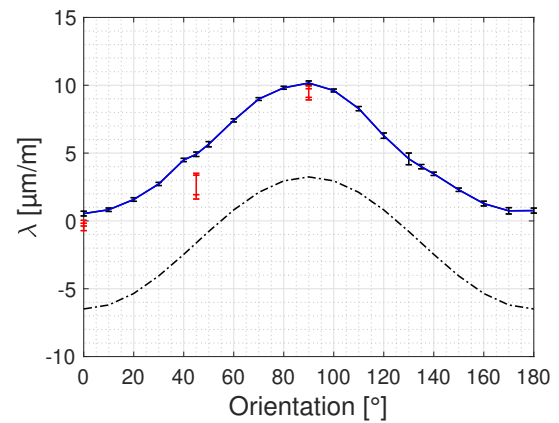Figure 4.32: The calculated saturation magnetostriction λ_s of Fe₉₅Cu₅, No. 2.

Figure 4.33: Image of the microstructure of Fe₉₅Cu₅, No. 2.

4.2.3 Fe$_{85}$Cu$_{15}$, No. 1

The results of the magnetostriction measurements as well as a scanning electron micrograph of the Fe$_{85}$Cu$_{15}$, No. 1 specimen are shown below. The determined mean value of all saturation magnetostriction values above magnetic fields of 1 T was $-6\,\frac{\mu m}{m}$ $\pm\,0.3\,\frac{\mu m}{m}$. The image of the specimen microstructure was acquired at a specimen radius of 1 mm. The average of the measured specimen hardness after deformation was 629 $HV0.5 \pm 6\ HV0.5$. The averaged chemical composition of the specimen, which was measured using EDX, consisted of 83.9 % ± 2.7 % Fe and 16.1 % ± 2.7 % Cu.

Figure 4.34: Measured magnetostrictive strain λ of Fe$_{85}$Cu$_{15}$, No. 1 for the specimen orientations of 0°, 45° and 90°.

Figure 4.35: Measured magnetostrictive strain λ of Fe$_{85}$Cu$_{15}$, No. 1 of the second measurement concept.

Figure 4.36: The calculated saturation magnetostriction λ$_s$ of Fe$_{85}$Cu$_{15}$, No. 1.
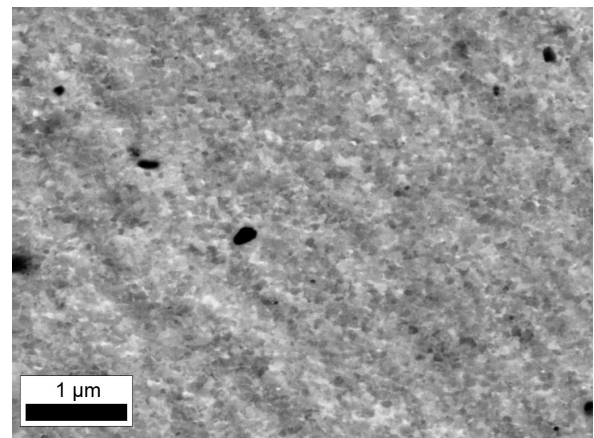
Figure 4.37: Image of the microstructure of Fe$_{85}$Cu$_{15}$ No. 1 at r = 1 mm.

4.2.4 Fe$_{85}$Cu$_{15}$, No. 2

The results of the magnetostriction measurements as well as a scanning electron micrograph of the Fe$_{85}$Cu$_{15}$, No. 2 specimen are shown below. The determined mean value of all saturation magnetostriction values above magnetic fields of 1 T was $-6\,\frac{\mu m}{m}$ $\pm\,0.3\,\frac{\mu m}{m}$. The average of the measured specimen hardness after deformation was 502 *HV*0.3 $\pm$ 20 *HV*0.3. The averaged chemical composition of the specimen, which was measured using EDX, consisted of 85.6 % $\pm$ 5.3 % Fe and 14.4 % $\pm$ 5.3 % Cu.

Figure 4.38: Measured magnetostrictive strain λ of Fe$_{85}$Cu$_{15}$, No. 2 for the specimen orientations of 0°, 45° and 90°.

Figure 4.39: Measured magnetostrictive strain λ of Fe$_{85}$Cu$_{15}$, No. 2 of the second measurement concept.
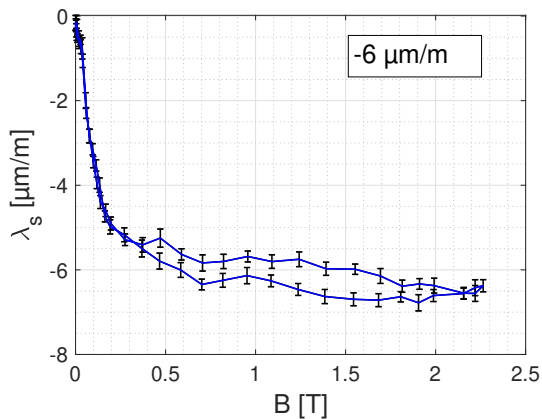

Figure 4.40: The calculated saturation magnetostriction λ$_s$ of Fe$_{85}$Cu$_{15}$, No. 2.
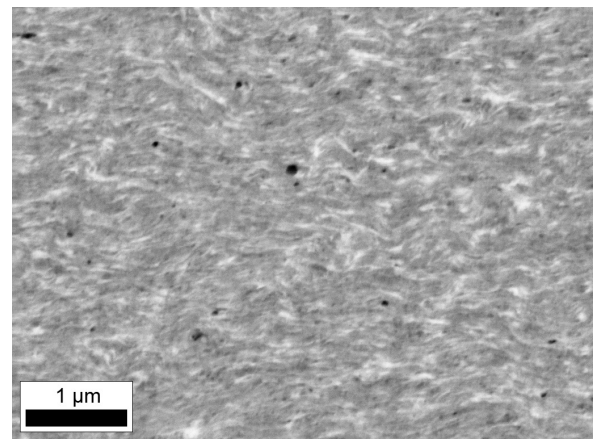
Figure 4.41: Image of the microstructure of Fe$_{85}$Cu$_{15}$, No. 2.

4.2.5 Fe$_{70}$Cu$_{30}$

The results of the magnetostriction measurements as well as a scanning electron micrograph of the Fe$_{70}$Cu$_{30}$ specimen are shown below. The determined mean value of all saturation magnetostriction values above magnetic fields of 1 T was $-5\,\frac{\mu m}{m} \pm 0.3\,\frac{\mu m}{m}$. The average of the measured specimen hardness after deformation was 433 $HV0.5 \pm$ 12 $HV0.5$. The averaged chemical composition of the specimen, which was measured using EDX, consisted of 67.2 % ± 2.7 % Fe and 32.8 % ± 2.7 % Cu.
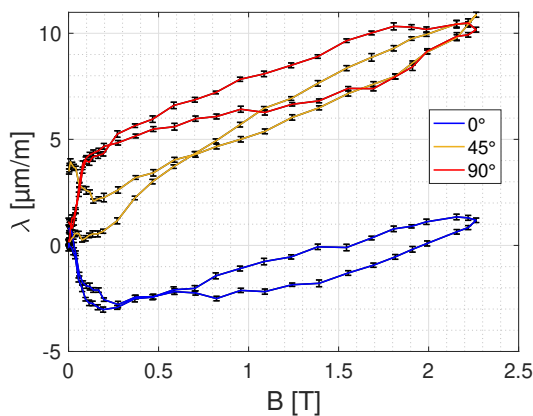

Figure 4.42: Measured magnetostrictive strain λ of Fe$_{70}$Cu$_{30}$ for the specimen orientations of 0°, 45° and 90°.
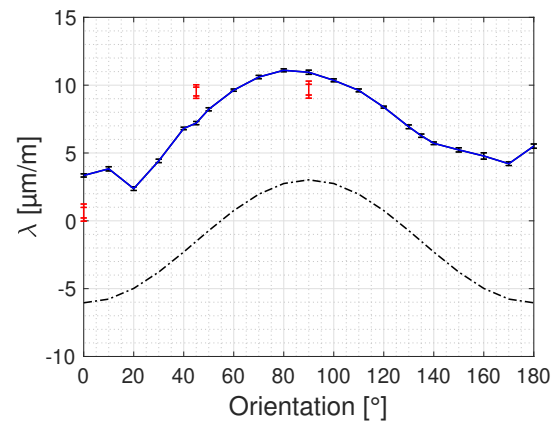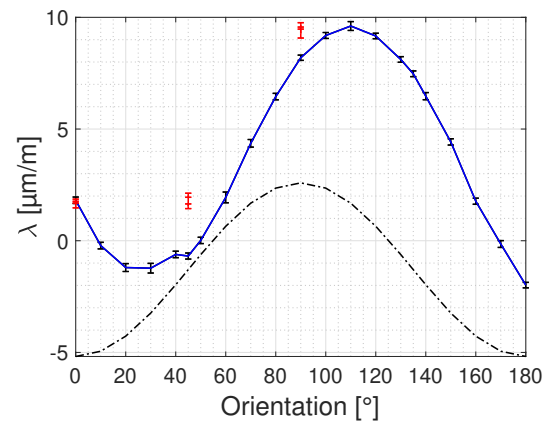

Figure 4.43: Measured magnetostrictive strain λ of Fe$_{70}$Cu$_{30}$ of the second measurement concept.
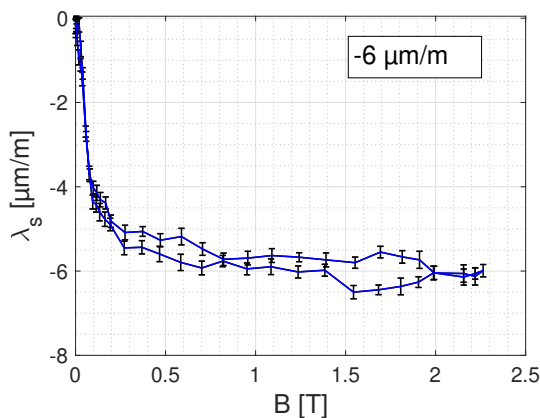

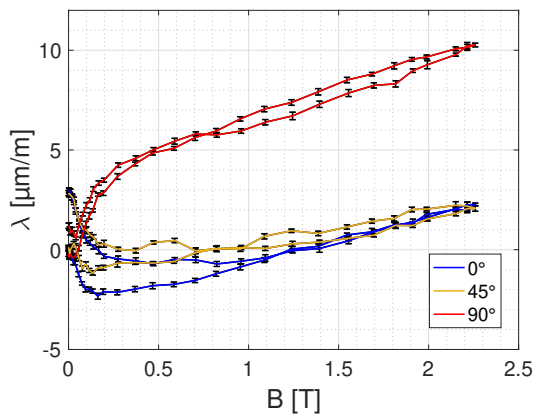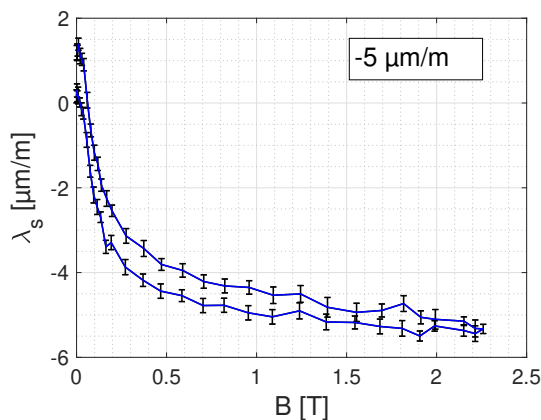Figure 4.44: The calculated saturation magnetostriction λ$_s$ of Fe$_{70}$Cu$_{30}$.
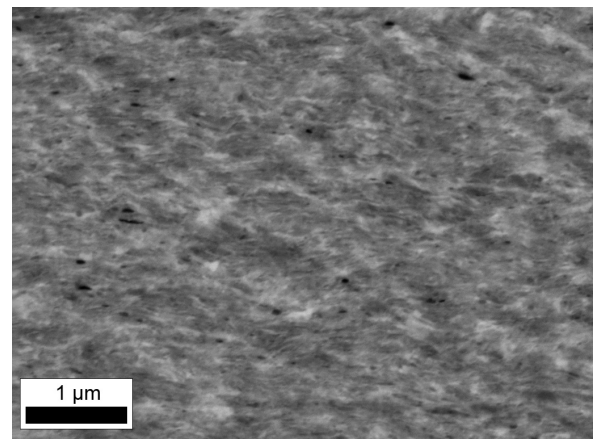
Figure 4.45: Image of the microstructure of Fe$_{70}$Cu$_{30}$.

4.2.6 XRD measurements of the Fe-Cu system

The results of the conducted XRD measurements of the Fe-Cu system are presented below. As mentioned in chapter 3.3, a specimen with identical chemical composition and HPT processing route was used for the XRD measurement in the case of the specimen $Fe_{70}Cu_{30}$. The vertical lines indicate the theoretical peak positions of copper (red) and iron (blue).
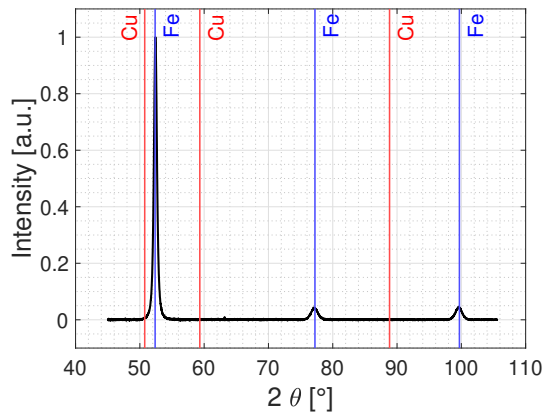
Figure 4.46: The diffraction pattern of the specimen $Fe_{95}Cu_5$ No. 2.
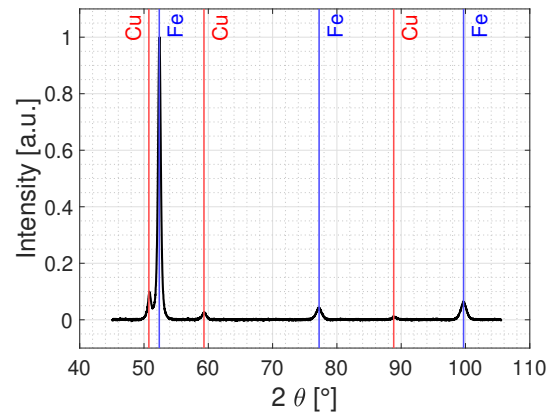
Figure 4.47: The diffraction pattern of the specimen $Fe_{85}Cu_{15}$ No. 1.
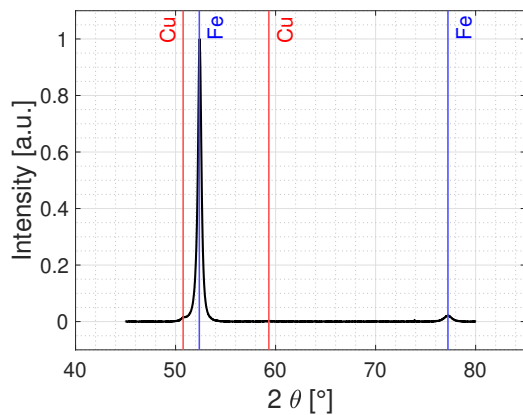
Figure 4.48: The diffraction pattern of the specimen $Fe_{85}Cu_{15}$ No. 2.
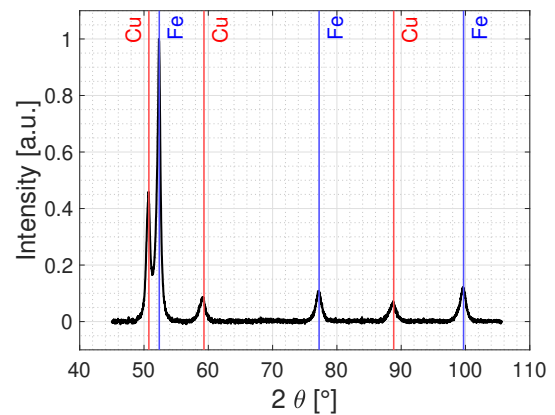
Figure 4.49: The diffraction pattern of a specimen with identical composition and HPT processing route as the specimen $Fe_{70}Cu_{30}$.

4.2.7 Discussion of the results of the Fe-Cu system

As visible in the images, which illustrate the result of the first measurment method, all specimens exhibit a volume-magnetostrictive behavior. The magnetostriction of each specimen generally rises with the same slope after magnetic saturation of the specimen is reached. This magnetostrictive behavior is similar to the magnetostrictive behavior of pure Fe. In addition, it is recognizable for most specimens, that the magnetostriction, which was determined at a specimen orientation of 45° is close to one of the measured magnetostriction values, which were measured at a specimen orientation of 0° or 90°, which is especially the case for the the specimens $Fe_{95}Cu_5$, No. 1 and $Fe_{70}Cu_{30}$. The specimen $Fe_{95}Cu_5$, No. 2 shows a different behavior. The magnetostriction, measured at a specimen orientation of 45°, even exceeds the measured magnetostriction of the specimen orientation of 90°, as illustrated in figure 4.30. A similar behavior has been observed for the annealed specimen Fe, No. 2, where this behavior was devoted to the evolution of a pronounced texture.

The results of the first measurement concept that were determined at a current of 120 A, fit pretty well to the results of the second measurement concept (see the red markers in the figures illustrating the results of the second measurement concept). Yet, slight variations between the determined data points of the first and the results of the second measurment concept are visible for every specimen. The biggest difference is visible in the case of the specimen $Fe_{95}Cu_5$, No. 2. As illustrated in figure 4.31, all data points of the magnetostriction values of the first measurement concept are below the measured magnetostriction values of the second measurement concept. This difference might have occured due to a drift or an offset in the measured values. The offset between the measured magnetostriction values and the calculated values of $\lambda_s(\theta)$ is seen as a consequence of the volume magnetostriction of Fe. It is recognizable, that the measured values, which were determined using the second measurement concept, of three out of five specimens exhibit similarities with the calculated values of $\lambda_s(\theta)$. With exception of the offset, the trend in measured magnetostriction of the specimen $Fe_{85}Cu_{15}$, No. 1 fits very good to the calculated values of $\lambda_s(\theta)$, as illustrated in figure 4.35. The trend of the specimens $Fe_{95}Cu_5$, No. 1 and $Fe_{85}Cu_{15}$, No. 2 show good compliance with the trend of the calculated values of $\lambda_s(\theta)$. Slight deviations are visible at specimen orientations near 0° and 180°. As illustrated in figure 4.39, the maximum value of the measured curve is slightly shifted to a specimen orientation of 80° for the specimen $Fe_{85}Cu_{15}$, No. 2, which might be due to a small misalignment of the strain gauge with the magnetic field.

The measured magnetostriction values of the second measurement concept of the specimens $Fe_{95}Cu_5$, No. 2 and $Fe_{70}Cu_{30}$ show a different behavior as the calculated mag-

netostriction values of $\lambda_s(\theta)$. Equal to the specimen Fe, No. 2, this mismatch may be an indication for the presence of a preferred grain orientation. A texture analysis of all involved specimens would be needed to decide on this hypothesis. The results of the magnetostriction measurements of the specimen $Fe_{95}Cu_5$, No. 2 exhibit similarities to the specimen Fe, No. 2.

The determined mean values of the saturation magnetostriction above a magnetic field of 1 T in dependence on the Cu content of each specimen are illustrated in figure 4.50. In addition, the determined mean values of λ_s of both HPT deformed Fe specimens are illustrated as black lines. The mean value of the saturation magnetostriction of Fe, No. 2 is not included, since the specimen was in an annealed state and both HPT deformed specimens show better compliance with literature values. It is recognizable, that the addition of Cu increases the saturation magnetostriction of Fe. A

Figure 4.50: Comparison of the determined mean values of λ_s depending on the measured Cu-content of each specimen.

small amount of 5.6 at % to 8.2 at % Cu leads to a stronger increase of λ_s than a higher amount of 14.4 at % to 16.1 at %. In the case of the specimen composition $Fe_{95}Cu_5$, an XRD measurement was conducted only for the specimen $Fe_{95}Cu_5$, No. 2 which is illustrated in figure 4.46. It is recognizable, that only peaks of Fe were measured and no peaks of Cu appear, which leads to the conclusion, that Cu was dissolved in the Fe matrix by HPT processing and a supersaturated solid solution was formed. Both specimens with the composition $Fe_{85}Cu_{15}$ exhibit very similar values of λ_s. Yet, differences in the results of the XRD measurements are visible. While small Cu peaks are visible in the results of $Fe_{85}Cu_{15}$, No. 1, as illustrated in figure 4.47, the Cu peaks almost vanish in the case of $Fe_{85}Cu_{15}$, No. 2. As illustrated in figure 4.48 only a very slight peak can be estimated at 2θ of about 50°. The difference of the XRD measurements may be a consequence of the different deformation parameters. While the specimen $Fe_{85}Cu_{15}$, No. 1 was deformed using a one-step deformation process at an elevated temperature of 300 °C, the specimen $Fe_{85}Cu_{15}$, No. 2 was deformed using a two-step deformation process. In a first step, the specimen was deformed at a temperature of 500 °C for 50 turns. In a second step, the specimen was deformed at RT for one rotation only to refine the microstructure but trying to keep the supersaturated microstructure. According to
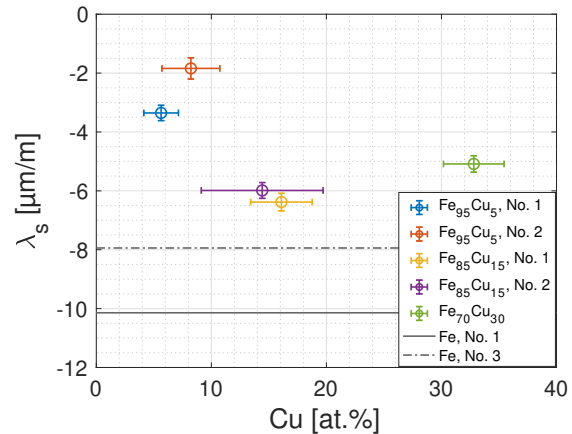
the results of the XRD measurements, it seems that a two-step deformation process at higher temperatures enhances the solution of Cu in Fe. In the case of $Fe_{70}Cu_{30}$, the XRD measurement was conducted on a specimen with identical nominal composition and HPT processing route. As illustrated in figure 4.49, the results of the XRD measurement show peaks of Fe and Cu. Combining the XRD-results with the results of the magnetostriction measurements, it seems that the amount of Cu in supersaturated solution in Fe does not have a strong influence on the saturation magnetostriction at compositions close to 15 at % Cu. However, for smaller amounts of Cu close to 5 at % to 8 at %, the effect is stronger. This is the composition range, where further research on low-magnetostrictive NC Fe-Cu materials should set in.

From scanning electron micrographs it can be said that all specimens exhibit a homogeneous, NC microstructure. The mean values of the measured hardness values in dependence on the Cu content of each specimen is illustrated in figure 4.51. In addition, the hardness mean values of both HPT deformed Fe specimens are marked as horizontal lines. The mean values of the hardness of the specimens with a nominal Cu content of 5 at % are almost identical. A low amount of Cu leads to a significant increase in the specimen hardness. This hardness increase is even higher in the case of $Fe_{85}Cu_{15}$, No.

Figure 4.51: Comparison of the determined hardness mean values depending on the measured Cu-content of each specimen.

1. However, the difference between the hardness mean values of both specimens with a nominal Cu content of 15 at % is very high. A reason for this big difference in hardness are the two different processing routes. It seems, that the microstructure is not yet fully refined after one additional rotation at RT, when starting from a microstructure, that was previously deformed at 500 °C. The measured hardness value drops below the measured hardness values of HPT deformed Fe, as the Cu content is increased to nominally 30 at %.

4.3 Results for the Fe-Cr system

4.3.1 Fe$_{70}$Cr$_{30}$, No. 1

The results of the magnetostriction measurements as well as a scanning electron micrograph of the **HPT deformed Fe$_{70}$Cr$_{30}$** specimen are shown below. The determined mean value of all saturation magnetostriction values above magnetic fields of 1 T was $17 \frac{\mu m}{m} \pm 0.3 \frac{\mu m}{m}$. The average of the measured specimen hardness after deformation was $555\ HV0.5 \pm 4\ HV0.5$. The averaged concentration of Fe, which was measured using EDX, was $69.1\ \% \pm 1.1\ \%$[19].

Figure 4.52: Measured magnetostrictive strain λ of Fe$_{70}$Cr$_{30}$, No. 1 for the specimen orientations of 0° and 90°.

Figure 4.53: Measured magnetostrictive strain λ of Fe$_{70}$Cr$_{30}$, No. 1 of the second measurement concept.
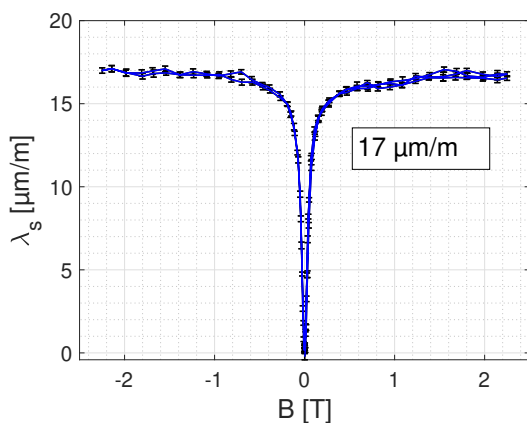
Figure 4.54: The calculated saturation magnetostriction λ_s of Fe$_{70}$Cr$_{30}$, No. 1.
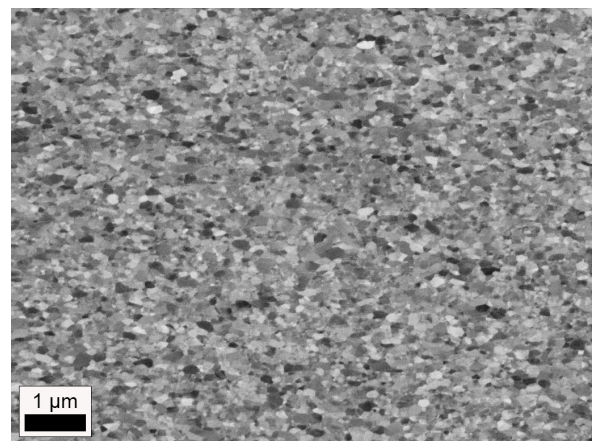
Figure 4.55: Image of the microstructure of HPT deformed Fe$_{70}$Cr$_{30}$.

4.3.2 Fe$_{70}$Cr$_{30}$, No. 2

The results of the magnetostriction measurements as well as a scanning electron micrograph of the **HPT deformed and annealed Fe$_{70}$Cr$_{30}$** specimen are shown below. The determined mean value of all saturation magnetostriction values above magnetic fields of 1 T was 22 $\frac{\mu m}{m}$ ± 0.5 $\frac{\mu m}{m}$. The average of the measured specimen hardness after deformation was 386 $HV0.5$ ± 4 $HV0.5$. The averaged concentration of Fe, which was measured using EDX, was 69.1 % ± 1.1 %[19].

Figure 4.56: Measured magnetostrictive strain λ of Fe$_{70}$Cr$_{30}$, No. 2 for the specimen orientations of 0° and 90°.

Figure 4.57: Measured magnetostrictive strain λ of Fe$_{70}$Cr$_{30}$, No. 2 of the second measurement concept.
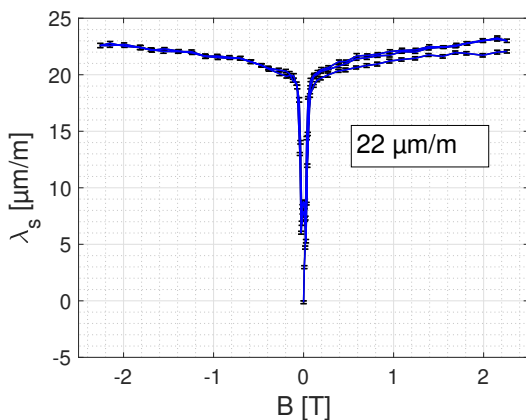
Figure 4.58: The calculated saturation magnetostriction λ$_s$ of Fe$_{70}$Cr$_{30}$, No. 2.
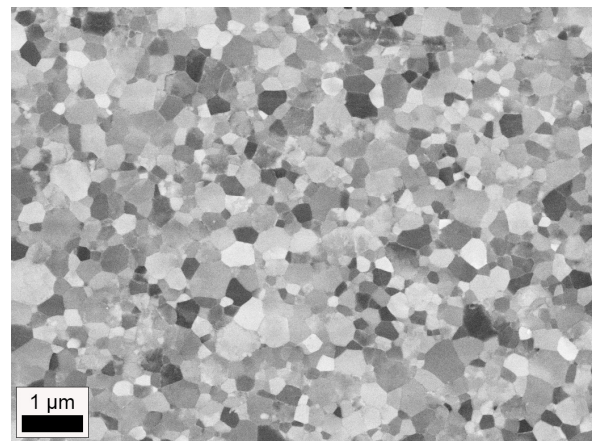
Figure 4.59: Microstructure of HPT deformed and annealed Fe$_{70}$Cr$_{30}$.

4.3.3 Fe$_{50}$Cr$_{50}$, No. 1

The results of the magnetostriction measurements as well as a scanning electron micrograph of the **HPT deformed Fe$_{50}$Cr$_{50}$** specimen are shown below. The determined mean value of all saturation magnetostriction values above magnetic fields of 1 T was $8 \frac{\mu m}{m} \pm 0.4 \frac{\mu m}{m}$. The average of the measured specimen hardness after deformation was $664\, HV0.5 \pm 13\, HV0.5$. The averaged concentration of Fe, which was measured using EDX, was $48.7\,\% \pm 0.8\,\%$[19].
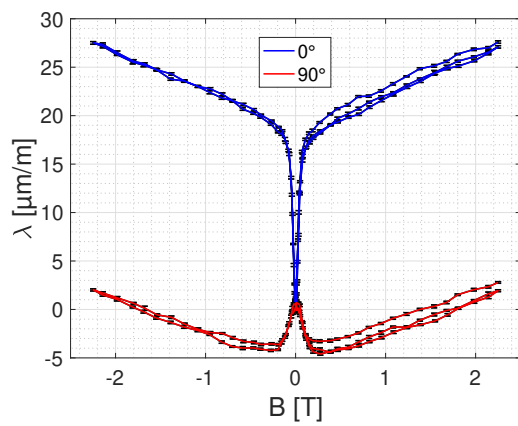

Figure 4.60: Measured magnetostrictive strain λ of Fe$_{50}$Cr$_{50}$, No. 1 for the specimen orientations of 0° and 90°.
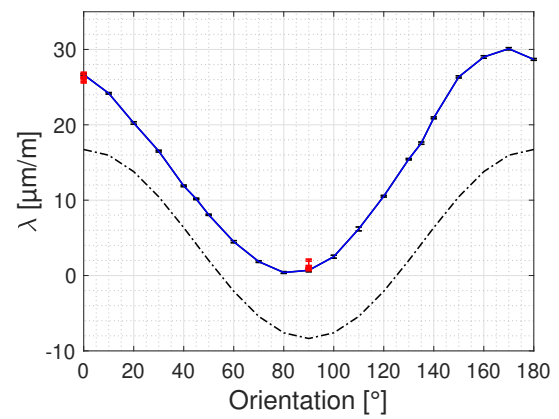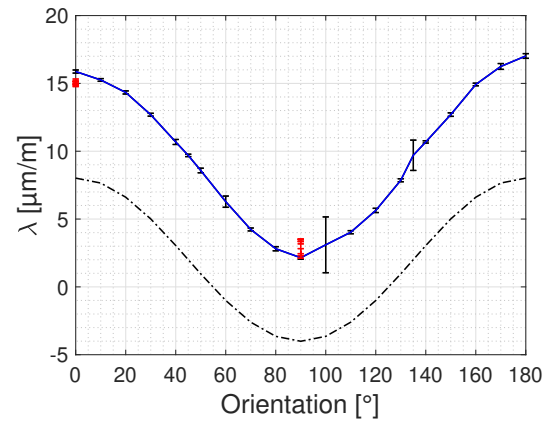

Figure 4.61: Measured magnetostrictive strain λ of Fe$_{50}$Cr$_{50}$, No. 1 of the second measurement concept.
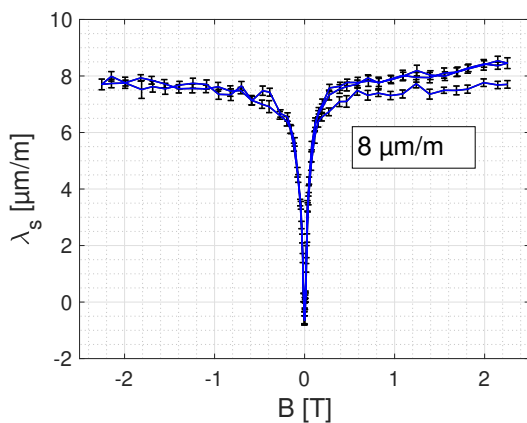
Figure 4.62: The calculated saturation magnetostriction λ$_s$ of Fe$_{50}$Cr$_{50}$, No. 1.
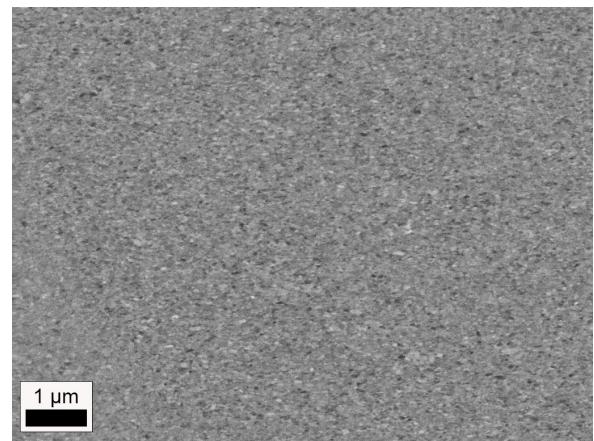
Figure 4.63: Image of the microstructure of HPT deformed Fe$_{50}$Cr$_{50}$.

4.3.4 Fe$_{50}$Cr$_{50}$, No. 2

The results of the magnetostriction measurements as well as a scanning electron micrograph of the **HPT deformed and annealed Fe$_{50}$Cr$_{50}$** specimen are shown below. The determined mean value of all saturation magnetostriction values above magnetic fields of 1 T was 12 $\frac{\mu m}{m}$ ± 0.2 $\frac{\mu m}{m}$. The average of the measured specimen hardness after deformation was 555 $HV0.5$ ± 2 $HV0.5$. The averaged concentration of Fe, which was measured using EDX, was 48.7 % ± 0.8 %[19].
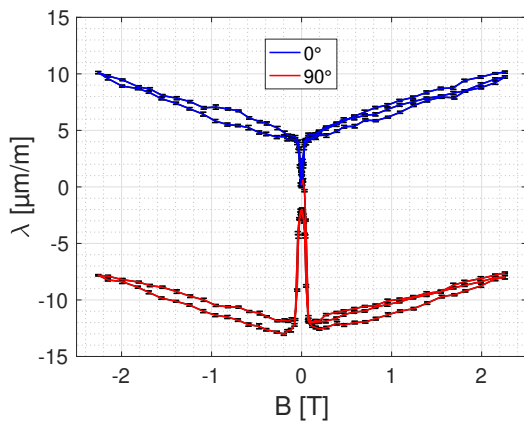
Figure 4.64: Measured magnetostrictive strain λ of Fe$_{50}$Cr$_{50}$, No. 2 for the specimen orientations of 0° and 90°.
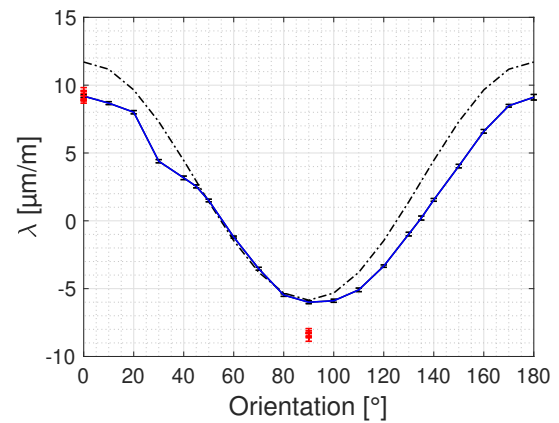
Figure 4.65: Measured magnetostrictive strain λ of Fe$_{50}$Cr$_{50}$, No. 2 of the second measurement concept.
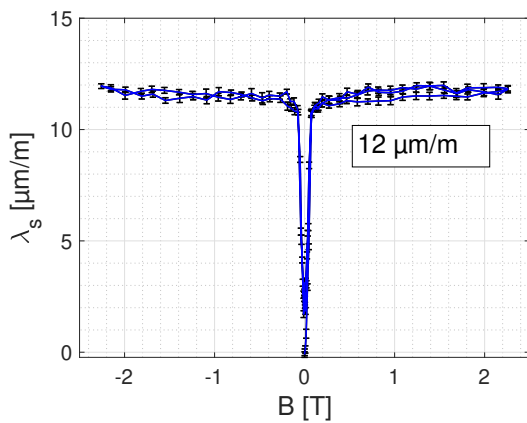
Figure 4.66: The calculated saturation magnetostriction λ$_s$ of Fe$_{50}$Cr$_{50}$, No. 2.
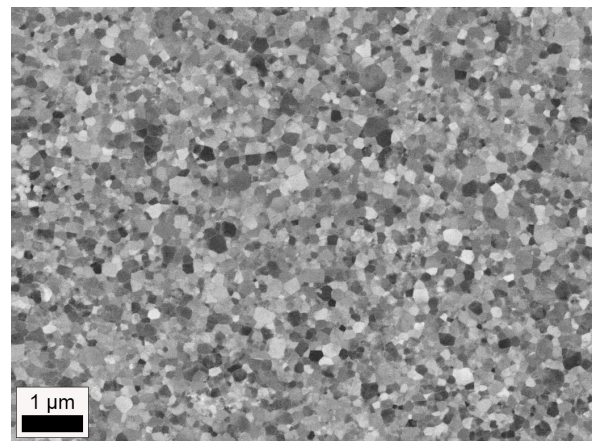
Figure 4.67: Microstructure of HPT deformed and annealed Fe$_{50}$Cr$_{50}$.

4.3.5 Fe$_{30}$Cr$_{70}$, No. 1

The results of the magnetostriction measurements as well as a scanning electron micrograph of the **HPT deformed Fe$_{30}$Cr$_{70}$** specimen are shown below. The determined mean value of all saturation magnetostriction values above magnetic fields of 1 T was $0 \frac{\mu m}{m} \pm 0.3 \frac{\mu m}{m}$. The average of the measured specimen hardness after deformation was $769\,HV0.5 \pm 11\,HV0.5$. The averaged concentration of Fe, which was measured using EDX, was $27.8\,\% \pm 3.3\,\%$ [19].
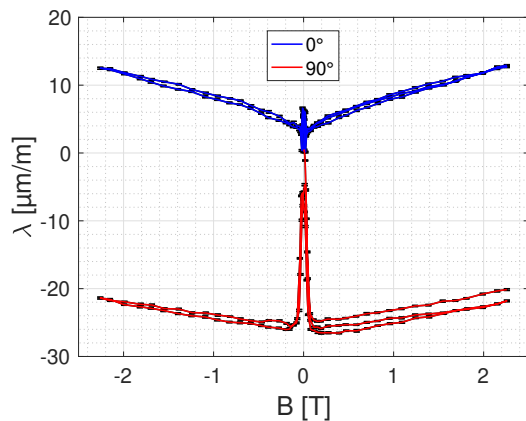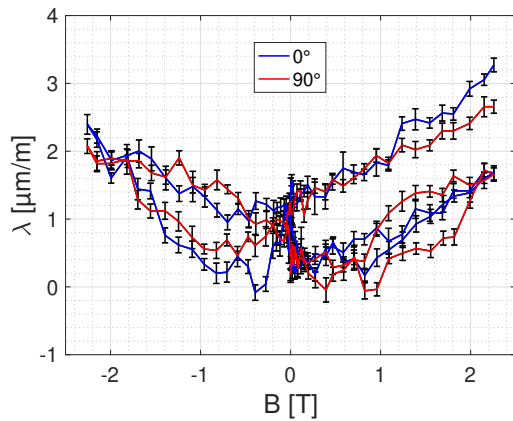

Figure 4.68: Measured magnetostrictive strain λ of Fe$_{30}$Cr$_{70}$, No. 1 for the specimen orientations of 0° and 90°.
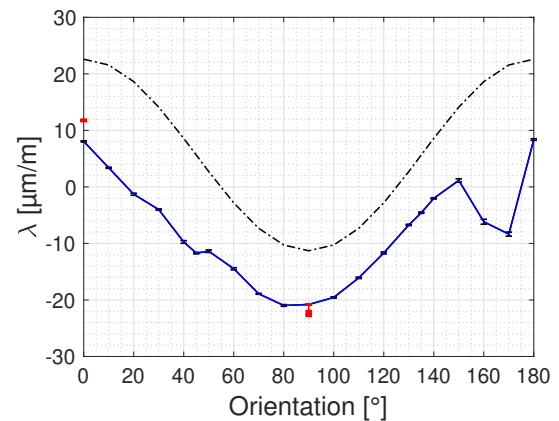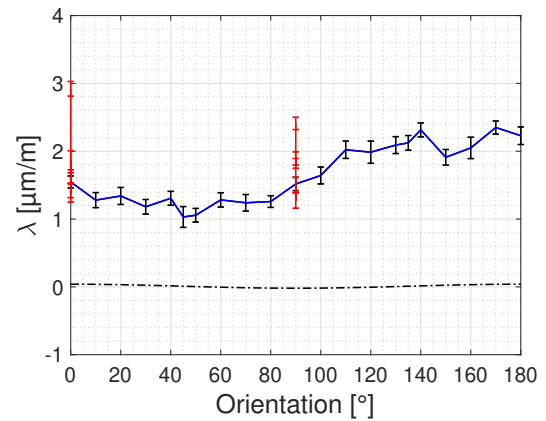

Figure 4.69: Measured magnetostrictive strain λ of Fe$_{30}$Cr$_{70}$, No. 1 of the second measurement concept.

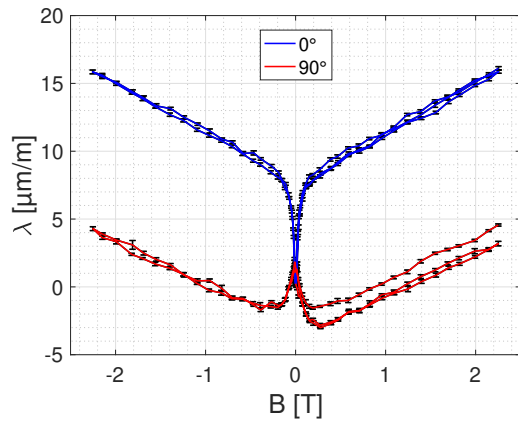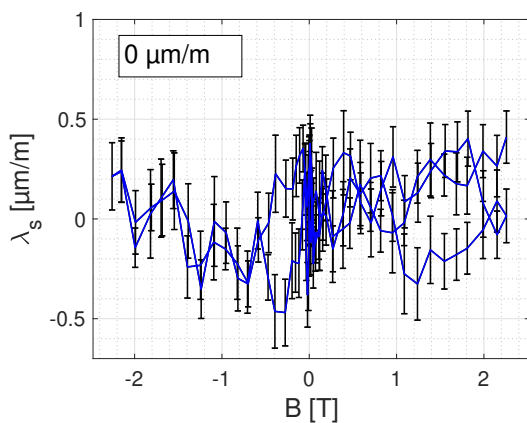Figure 4.70: The calculated saturation magnetostriction λ$_s$ of Fe$_{30}$Cr$_{70}$, No. 1.
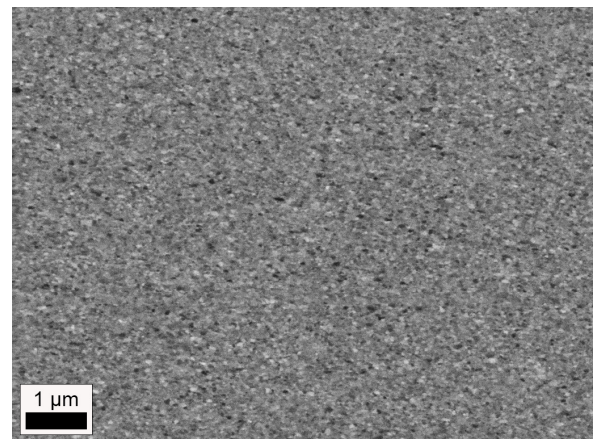
Figure 4.71: Image of the microstructure of HPT deformed Fe$_{30}$Cr$_{70}$.

4.3.6 Fe$_{30}$Cr$_{70}$, No. 2

The results of the magnetostriction measurements as well as a scanning electron micrograph of the **HPT deformed and annealed Fe$_{30}$Cr$_{70}$** specimen are shown below. The determined mean value of all saturation magnetostriction values above magnetic fields of 1 T was $1 \frac{\mu m}{m} \pm 0.5 \frac{\mu m}{m}$. The average of the measured specimen hardness after deformation was 798 $HV0.5 \pm 13$ $HV0.5$. The averaged concentration of Fe, which was measured using EDX, was 27.8 % $\pm$ 3.3 %[19].
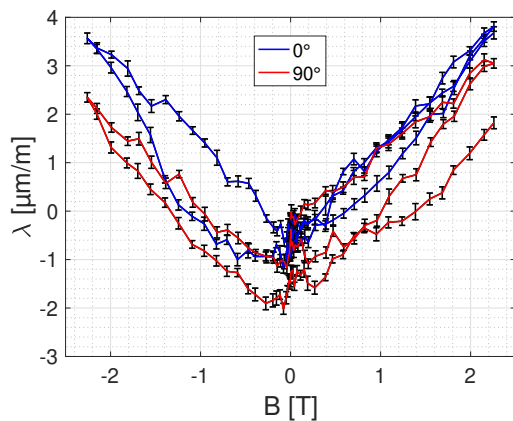
Figure 4.72: Measured magnetostrictive strain λ of Fe$_{30}$Cr$_{70}$, No. 2 for the specimen orientations of 0° and 90°.
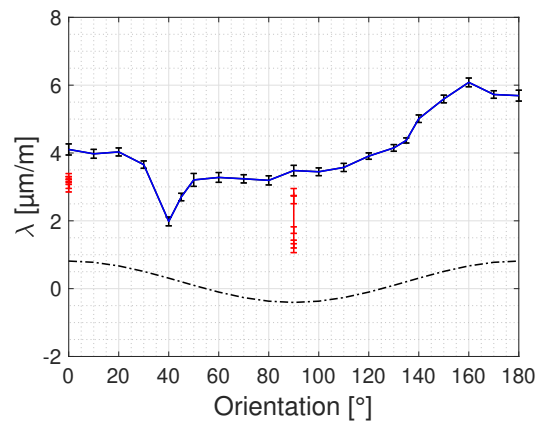
Figure 4.73: Measured magnetostrictive strain λ of Fe$_{30}$Cr$_{70}$, No. 2 of the second measurement concept.
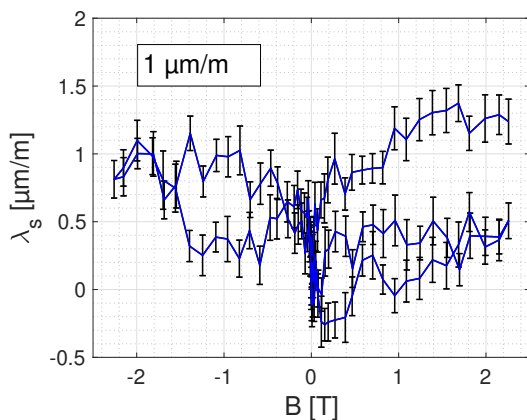
Figure 4.74: The calculated saturation magnetostriction λ_s of Fe$_{30}$Cr$_{70}$, No. 2.
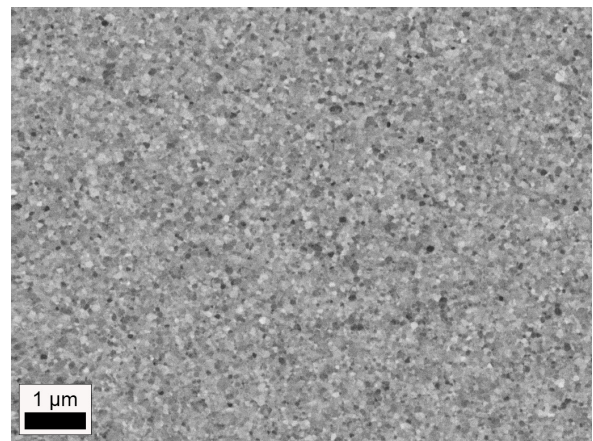
Figure 4.75: Microstructure of HPT deformed and annealed Fe$_{30}$Cr$_{70}$.

4.3.7 Synchrotron measurements of the Fe-Cr system

The results of performed synchrotron measurements of the Fe-Cr system are listed below. As mentioned in chapter 3.3, the experiments were conducted on specimens with identical chemical composition and HPT processing route instead of the specimens, which were used for the magnetostriction measurements. The measured spectrum (a) as well as the most distinctive peak (b) are illustrated for every specimen composition. The vertical lines indicate the theoretical peak positions of Cr (red) and Fe (blue).
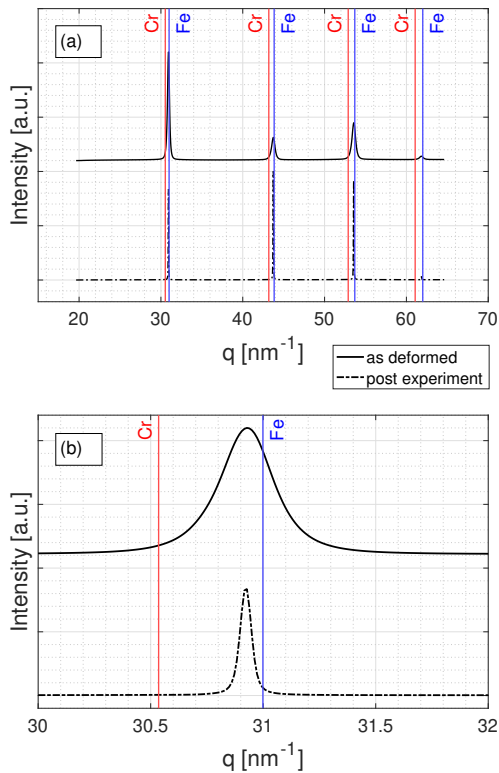
Figure 4.76: Image of (a) the overall measured diffraction pattern and (b) the most distinct peak of $Fe_{70}Cr_{30}$ after HPT deformation as well as after an in-situ annealing HEXRD experiment.
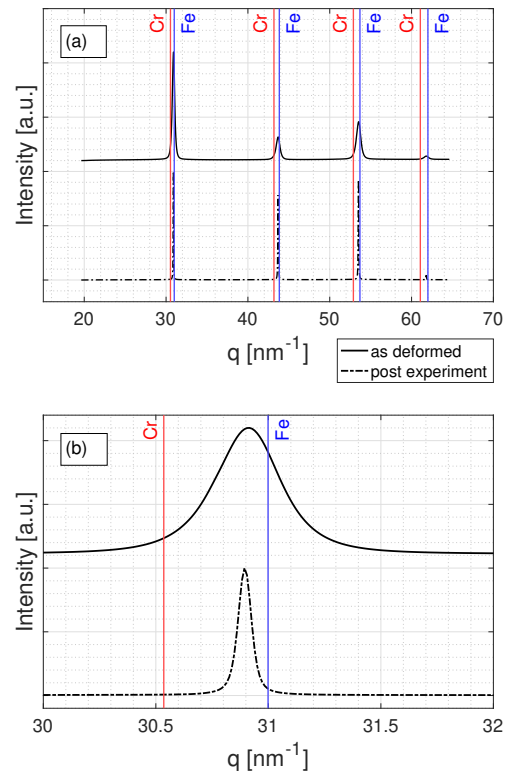
Figure 4.77: Image of (a) the overall measured diffraction pattern and (b) the most distinct peak of $Fe_{50}Cr_{50}$ after HPT deformation as well as after an in-situ annealing HEXRD experiment.
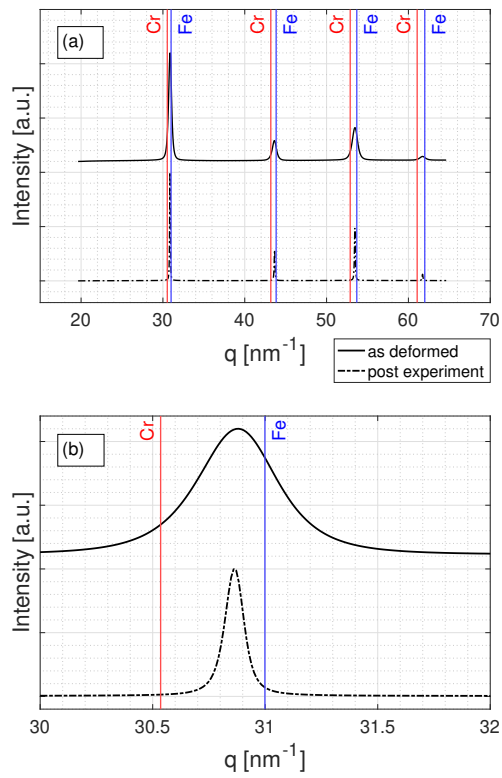
Figure 4.78: Image of (a) the overall measured diffraction pattern and (b) the most distinct peak of $Fe_{30}Cr_{70}$ after HPT deformation as well as after an in-situ annealing HEXRD experiment.

4.3.8 Discussion of the results of the Fe-Cr system

In contrast to the magnetostriction measurements of pure elements and the Fe-Cu system, the magnetostriction measurements of the Fe-Cr system were conducted at positive and negative magnetic fields, as mentioned in chapter 3.4. The figures illustrating the results of the first measurement concept show a symmetric behavior of the measured magnetostriction values over the applied magnetic field. In addition, the measured magnetostriction of all specimens exhibits a volume-magnetostrictive behavior, similar to the behavior of the Fe and Fe-Cu specimens.

In the case of the specimen $Fe_{50}Cr_{50}$, No. 1 a slight difference in the determined magnetostriction values at a specimen orientation of 90° is recognizable, which is visible in figure 4.60. The magnetostriction values measured during initial magnetization and the first branch of the hysteresis are smaller compared to values measured in the later part of the hysteresis. As the polarization of the magnetic field is changed, a slight increase of the magnetostriction values seems to appear, which results in an offset between these two parts of the measurement curve. A similar behavior is visible for the measured magnetostriction values at a specimen orientation of 90° of the specimen $Fe_{30}Cr_{70}$, No. 1, as illustrated in figure 4.68. This offset appears to be smaller than in the case of the specimen $Fe_{50}Cr_{50}$, No. 1, which might be due to the fact, that the measured magnetostriction values of the specimen $Fe_{30}Cr_{70}$, No. 1 are generally very small. In both cases, an increase in temperature was measured during the experiment, which would explain this offset. However, the question whether this behavior can be attributed to temperature changes or to the procedure of polarization changes still needs to be answered.

Another interesting behavior can be observed for the compositions $Fe_{70}Cr_{30}$ and $Fe_{50}Cr_{50}$. At small fields, the as-deformed states of both compositions show a strong increase of the magnetostriction determined at a specimen orientation of 0°, while the measured magnetostriction of the specimen orientation of 90° slightly decreases. This behavior is reversed after an annealing treatment. In both cases, the magnetostriction that was measured at a specimen orientation of 0° shows only a slight increase while the determined magnetostriction at a specimen orientation of 90° shows a stronger decrease. This behavior is hard to confirm in the case of the composition $Fe_{30}Cr_{70}$ since the measured magnetostriction values of the specimen orientations of 0° and 90° show almost no difference. Yet, a very slight decrease of the magnetostriction values measured at a specimen orientation of 90° might be assumed.

The measured magnetostriction values at a current of 120 A of the first measurement concept as well as the calculated values of $\lambda_s(\theta)$ show good compliance with the measured magnetostriction values of the second measurement concept. An offset between

the measured magnetostriction values and the calculated values of $\lambda_s(\theta)$ is visible for almost all specimens. As it was found in the results of Fe and the Fe-Cu system, this offset is seen as a consequence of the volume magnetostriction also present in the Fe-Cr system. The calculated values of $\lambda_s(\theta)$ are below the measured magnetostriction values in the case of all HPT deformed Fe-Cr specimens as well as the HPT deformed and annealed specimen $Fe_{30}Cr_{70}$, No. 2. This condition has also been observed for the Fe specimens and the specimens of the Fe-Cu system. In the case of the specimens $Fe_{70}Cr_{30}$, No. 2 and $Fe_{50}Cr_{50}$, No. 2, the determined magnetostriction values of the second measurement concept are shifted towards lower values. As mentioned before, a shift towards lower magnetostriction values was observed for these two specimens also in the case of the first measurement concept. Yet, the reason for this downward shift cannot be stated. A decrease of the measured magnetostriction values at specimen orientations of 160° and 170° is visible in figure 4.57 of the specimen $Fe_{70}Cr_{30}$, No. 2. This decrease might have occurred due to a contact between the pole pieces and the strain gauge leads. A slight increase of the determined magnetostriction is recognizable for the specimens $Fe_{30}Cr_{70}$, No. 1 and $Fe_{30}Cr_{70}$, No. 2, as illustrated in the figures 4.69 and 4.73. This increase is expected to occur due to a thermal expansion, since a small increase of the temperature was measured in both cases.

Figure 4.79 illustrates the calculated mean values of the saturation magnetostriction depending on the concentration of Cr. An increase of λ_s for all compositions is visible compared to the mean values of λ_s of both HPT deformed Fe specimens. The specimen $Fe_{70}Cr_{30}$, No. 1 exhibits a high saturation magnetostriction of $17\,\frac{\mu m}{m}$. A decrease of λ_s with increasing concentration of Cr is recognizable for the HPT deformed specimens. This decrease follows a linear trend, as indicated by the dotted line in figure 4.79. The saturation magnetostriction increased for all specimen compositions after an an-

Figure 4.79: Comparison of the determined mean values of λ_s depending on the measured Cr-content of each specimen.

nealing treatment. While the saturation magnetostriction roughly increased by 30 % in the case of the specimen $Fe_{70}Cr_{30}$, No. 2, an increase of λ_s of 50 % is measurable in the case of the specimen $Fe_{50}Cr_{50}$, No. 2. The determined saturation magnetostriction of the composition $Fe_{30}Cr_{70}$ shows a very small increase from $0\,\frac{\mu m}{m}$ to $1\,\frac{\mu m}{m}$ after the

annealing treatment. The measured saturation magnetostriction of the HPT deformed and annealed specimens again indicates a linear decrease with increasing concentration of Cr, which is indicated by the dotted line in figure 4.79. Values for λ_s between $23\,\frac{\mu m}{m}$ and $47\,\frac{\mu m}{m}$ are stated by Bormio-Nunes et al. for the composition $Fe_{70}Cr_{30}$[23]. The measurements were conducted on cube shaped specimens with a coarse grained microstructure composed of elongated grains. In contrast to the specimens investigated in this thesis, these specimens did not experience severe plastic deformation but were directly produced by arc-melting. XRD measurements showed a single phase structure of the specimens and also confirmed a textured microstructure. Although the values of λ_s stated in literature are slightly higher than the measured saturation magnetostrictions of as-deformed $Fe_{70}Cr_{30}$, the saturation magnetostriction of annealed $Fe_{70}Cr_{30}$ already is within the range given in[23]. The results stated by Bormio-Nunes et al.[23] and in this thesis show that a significant increase of the saturation magnetostriction is recognizable compared to values for pure Fe.

All compositions exhibit a NC microstructure in the as-deformed state. Still, the microstructure of the specimen $Fe_{70}Cr_{30}$, No. 1 appears slightly coarser than the microstructures of the specimens $Fe_{50}Cr_{50}$, No. 1 and $Fe_{30}Cr_{70}$, No. 1, as illustrated in figure 4.55. The specimen $Fe_{70}Cr_{30}$, No. 2 still exhibits an UFG microstructure after annealing, although a strong grain growth is visible in figure 4.59. The amount of grain growth due to annealing decreases with increasing concentration of Cr. As illustrated in figure 4.75, almost no grain growth occurred due to annealing in the case of the specimen $Fe_{30}Cr_{70}$, No. 2.

The mean values of the measured hardness in dependence of the concentration of Cr are illustrated in figure 4.80. The mean values of the measured hardness of both HPT deformed Fe specimens are illustrated as a reference. A linear increase of the hardness with increasing concentration of Cr is visible in the case of the HPT deformed specimens as well as in the case of the HPT deformed and annealed specimens, which is indicated by the dotted trend lines. Due to recovery processes, the hardness of the specimens $Fe_{70}Cr_{30}$, No. 2 and $Fe_{50}Cr_{50}$, No. 2 decreased after annealing.
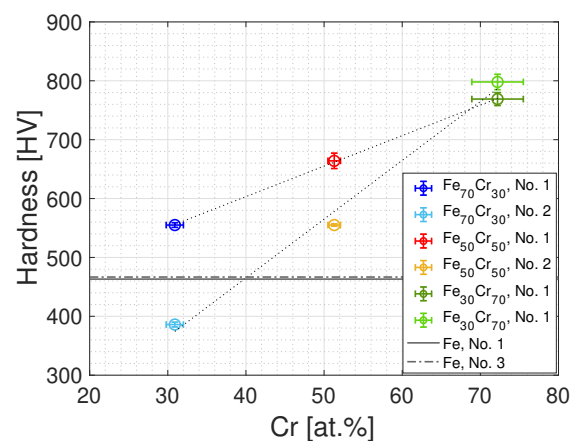
Figure 4.80: Comparison of the determined mean values of the hardness depending on the measured Cr-content of each specimen.

The results of the synchrotron measurements are listed in chapter 4.3.7. In the case of the as-deformed state, which is illustrated by the black line, broad peaks were measured between the theoretical peak positions of Cr (red) and Fe (blue). Since the theoretical positions of Cr and Fe are very close to each other, it cannot said with certainty if a supersaturated solid solution of Fe-Cr or two phases of Fe and Cr are present in the as-deformed state. Yet, a supersaturated solid solution is expected to be present in the as-deformed state, since the results of the magnetostriction measurements of the Fe-Cr system showed a completely different behavior than in the case of pure Fe.

4.4 Discussion of the temperature compensation

A compensation of temperature effects was described in the chapters 2.1.1 and 3.5.1. To compensate thermal induced straining of the specimen, three different methods were implemented into the automated data evaluation. Yet, only the results of the as-measured data were presented in chapter 4. To ensure a proper correction of thermal effects, still further evaluation of the magnetostriction data after temperature correction and comparison with the as-measured data has do be conducted. Although the as-measured values of the magnetostriction measurements of pure elements showed a good compliance with literature values and the observed temperature changes during all measurements were below $1\,°C$, a compensation of temperature changes was seen as a beneficial task.

All three methods of the temperature compensation shall be discussed on the measured magnetostriction values of the specimen $Fe_{85}Cu_{15}$, No. 2. The measurement was conducted at a specimen orientation of $0°$ using the first measurement method. The calculated temperature mean values as well as the corresponding standard deviations of every time span, in which the magnetic field was kept constant, are illustrated in figure 4.81 (a) by the blue line. In addition, the determined temperature differences corresponding to the first and third compensation method as well as the polynomial fit of the second compensation method are illustrated. The determined temperature differences of the first concept, which are illustrated by the red dotted line, do not clearly indicate an increase or decrease of the measured temperature. The quadratic fit corresponding to the second compensation method is illustrated by the green, dashed line. The fit captures the general evolution of the temperature very well. The black, dotted line illustrates the determined temperature differences of the third compensation method. Since the determination of ΔT is based on the comparison of the temperature mean values of all data points with the mean value of the first data point, the trend of the determined temperature differences exhibits the same behavior as the temperature curve.

The blue line in figure 4.81 (b) illustrates the as-measured magnetostriction values at a specimen orientation of $0°$. In addition, the magnetostriction values after temperature compensation using the first compensation method are illustrated by the red line. The magnetostriction values after compensation do not differ very much from the as-measured values. However, the compensated magnetostriction values tend to scatter around the as-measured curve. In figure 4.81 (c), a deviation of the corrected magnetostriction values from the as-measured values is visible after temperature compensation using the second method. A very similar shape of the as-measured magnetostric-
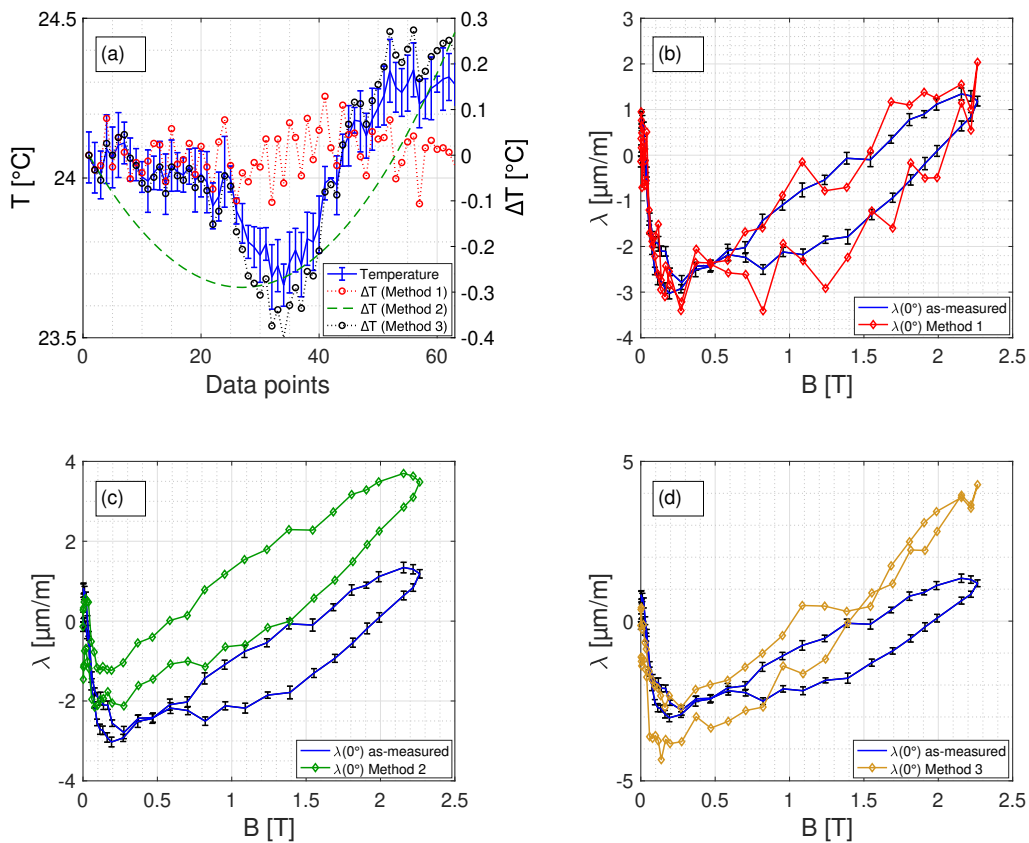
Figure 4.81: Comparison of three temperature compensation methods on the measured magnetostriction values of the specimen $Fe_{85}Cu_{15}$, No. 2 at a specimen orientation of 0°. (a) Measured temperature and the determined temperature changes ΔT corresponding to the three compensation methods. Comparison of the results of the first (b), second (c) and third (d) temperature compensation method with as-measured magnetostriction values.

tion curve and the curve after compensation of the temperature is recognizable. Figure 4.81 (d) shows a deviation of the magnetostriction values after temperature compensation using the third method from the as-measured values at high magnetic fields.

The exemplary results of the three temperature compensation methods that are illustrated in figure 4.81, visualize the behavior of the compensation methods pretty well. For most specimens, similar results of the magnetostriction values were obtained after a temperature compensation was conducted using either the second or the third method. Although it cannot be stated, if the second or the third compensation method provides better results, the temperature compensation using the first compensation method can be neglected, since the determined values only scatter around the as-measured magnetostriction values.

5 Summary

The aim of this thesis was the determination of the magnetostrictive behavior of three different material groups. For the determination of the magnetostrictive behavior, a newly built set-up was used and the measurements were conducted using two different measurement concepts. In the first concept, the electromagnet was actuated with a predefined current list resulting in a varying magnetic field, while the orientation of the specimen was kept constant during the measurement. Measurements were conducted for specimen orientations of 0°, 45° and 90°. In the second measurement concept, the electromagnet was actuated with a constant current value of 120 A resulting in a magnetic field close to 2 T and the specimen orientation was varied between 0° and 180°.

In the case of the first material group, magnetostriction measurements were conducted on coarse grained Co and Ni as well as on HPT deformed Fe specimens. A very good agreement of measured values and literature values confirmed the applicability and accuracy of the developed experimental set-up. In the second material group, specimens of the Fe-Cu system with nominal Cu contents between 5 at % and 30 at % were investigated. Powders of Fe and Cu were used as starting materials, which were compacted into solid specimens and subsequently deformed by HPT processing. The third investigated material group was the Fe-Cr system. Mixtures of Fe- and Cr-flakes with nominal Cr contents between 30 at % and 70 at % were arc melted prior to an HPT treatment. HPT deformations were conducted in the case of the second and third material group to form supersaturated solid solutions with a nanocrystalline microstructure. Annealing treatments of the Fe-Cr specimens after HPT deformation were conducted for 1 h at 500 °C to reveal a possibly still existing supersaturated Fe-Cr phase by using magnetostriction measurements.

Besides the determination of the magnetostrictive behavior, a characterization of the microstructure was conducted for all specimens. Scanning electron micrographs of the microstructure of the Ni specimen and all HPT deformed specimens were recorded. The hardness of all HPT deformed specimens was measured along the specimen radius. The chemical composition of all specimens was determined using EDX. XRD measurements in the case of the Fe-Cu system and HEXRD measurements in the case of the Fe-Cr system were performed to investigate the formation of supersaturated

solid solutions after HPT processing.

The results of the as-measured magnetostriction values of pure elements showed a good compliance with literature values, confirming the applicability of the newly built set-up. In the case of the Fe-Cu system, the determined saturation magnetostriction λ_s led to smaller absolute values for all measured specimen compositions. λ_s closest to 0 was measured for the specimen composition $Fe_{95}Cu_5$. Depending on the respective specimen composition, XRD measurements revealed either a supersaturated solid solution or a composite of two phases. In contrast to the saturation magnetostriction values determined for the specimens of the first and second material group, the determined saturation magnetostrictions of the Fe-Cr system exhibited positive values. A linear trend with decreasing values for λ_s was visible while the Cr content increased from 30 at % to 70 at %. After an annealing treatment of the specimens, an increase in saturation magnetostriction was determined for all specimen compositions. Still, a linear decreasing trend of λ_s was recognizable with increasing Cr content. According to the results of HEXRD measurements, a supersaturated solid solution of Fe-Cr was suggested to be present before as well as after the annealing treatment. The results of the magnetostriction measurements were seen as a confirmation of this suggestion, since the determined magnetostrictive behavior of the Fe-Cr system differed strongly from the determined magnetostrictive behavior of pure Fe. In general, a good compliance between the measured magnetostriction values of the first and second measurement concept were found for all three material groups.

Three different methods for the compensation of temperature effects were implemented into the automated data evaluation. The non-compensated, as-measured magnetostriction values are presented in this thesis, but the temperature compensation is seen as a beneficial tool for further magnetostriction measurements. Still, further evaluations of the measured magnetostriction data has to be conducted to state, which method yields the best results for the temperature compensation.

6 Bibliography

[1] M. J. Dapino, "On magnetostrictive materials and their use in adaptive structures," *Structural Engineering and Mechanics*, vol. 17, no. 3-4, p. 27, 2003.

[2] N. Ekreem, A. Olabi, T. Prescott, A. Rafferty, and M. Hashmi, "An overview of magnetostriction, its use and methods to measure these properties," *Journal of Materials Processing Technology*, vol. 191, pp. 96–101, Aug. 2007.

[3] B. D. Cullity and C. D. Graham, *Introduction to magnetic materials*. Hoboken, N.J: IEEE/Wiley, 2nd ed ed., 2009.

[4] E. W. Lee, "Magnetostriction and Magnetomechanical Effects," *Reports on Progress in Physics*, vol. 18, pp. 184–229, Jan. 1955. Publisher: IOP Publishing.

[5] S. Keil, *Dehnungsmessstreifen*. Wiesbaden: Springer Fachmedien Wiesbaden, 2017.

[6] R. Valiev, Y. Estrin, Z. Horita, T. Langdon, M. Zehetbauer, and Y. Zhu, "Fundamentals of Superior Properties in Bulk NanoSPD Materials," *Materials Research Letters*, vol. 4, pp. 1–21, Jan. 2016.

[7] Y. T. Zhu, T. C. Lowe, and T. G. Langdon, "Performance and applications of nanostructured materials produced by severe plastic deformation," *Scripta Materialia*, vol. 51, pp. 825–830, Oct. 2004.

[8] R. Valiev, "Nanostructuring of metals by severe plastic deformation for advanced properties," *Nature Materials*, vol. 3, pp. 511–516, Aug. 2004.

[9] R. Z. Valiev, Y. Estrin, Z. Horita, T. G. Langdon, M. J. Zechetbauer, and Y. T. Zhu, "Producing bulk ultrafine-grained materials by severe plastic deformation," *JOM*, vol. 58, pp. 33–39, Apr. 2006.

[10] R. B. Figueiredo and T. G. Langdon, "Fabricating Ultrafine-Grained Materials through the Application of Severe Plastic Deformation: a Review of Developments in Brazil," *Journal of Materials Research and Technology*, vol. 1, pp. 55–62, Apr. 2012.

[11] A. Bachmaier and R. Pippan, "High-Pressure Torsion Deformation Induced Phase Transformations and Formations: New Material Combinations and Advanced Properties," *MATERIALS TRANSACTIONS*, vol. 60, pp. 1256–1269, July 2019.

[12] K. S. Kormout, R. Pippan, and A. Bachmaier, "Deformation-Induced Supersaturation in Immiscible Material Systems during High-Pressure Torsion: Deformation-Induced Supersaturation," *Advanced Engineering Materials*, vol. 19, p. 1600675, Apr. 2017.

[13] A. Bachmaier, M. Kerber, D. Setman, and R. Pippan, "The formation of supersaturated solid solutions in Fe–Cu alloys deformed by high-pressure torsion," *Acta Materialia*, vol. 60, pp. 860–871, Feb. 2012.

[14] E. Greven and W. Magin, *Werkstoffkunde und Werkstoffprüfung für technische Berufe*. Hamburg: Handwerk und Technik, 14. stark überarb. aufl. / von wolfgang magin ed., 2004.

[15] H. Blumenauer, *Werkstoffprüfung: mit 93 Tabellen*. No. Book, Whole, Leipzig [u.a.]: Dt. Verl. für Grundstoffindustrie, 6., stark überarb. u. erw. aufl. ed., 1994.

[16] B. J. Inkson, "2 - Scanning electron microscopy (SEM) and transmission electron microscopy (TEM) for materials characterization," *Scanning electron microscopy*, pp. 17–43, 2016.

[17] P. Kapitza, "The study of the magnetic properties of matter in strong magnetic fields. Part V.— Experiments on magnetostriction in dia- and para-magnetic substances," *Proceedings of the Royal Society of London. Series A, Containing Papers of a Mathematical and Physical Character*, vol. 135, pp. 568–600, Apr. 1932.

[18] B. A. Messtechnik, "Betriebsanleitung Bruker B-E 30, Teil magnetische Prüfungen," 1993.

[19] L. Weissitsch, S. Wurster, A. Paulischin, M. Stückler, R. Pippan, and A. Bachmaier, "Nanocrystalline FeCr alloys synthesised by severe plastic deformation – A potential material for exchange bias and enhanced magnetostriction," *Journal of Magnetism and Magnetic Materials*, vol. 534, p. 168017, Sept. 2021.

[20] Y. Masiyama, "On the magnetostriction of iron-cobalt alloys," *Reprinted from the Science Reports of the Tohoku Imperial University*, vol. 1, pp. 394–410, Oct. 1932.

[21] Y. Masiyama, "On the magnetostriction of iron-nickel alloys," *Reprinted from the Science Reports of the Tohoku Imperial University*, vol. 1, pp. 574–593, Oct. 1931.

[22] O. Renk, P. Ghosh, and R. Pippan, "Generation of extreme grain aspect ratios in severely deformed tantalum at elevated temperatures," *Scripta Materialia*, vol. 137, pp. 60–63, Aug. 2017.

[23] C. Bormio-Nunes, J. P. Serra, F. S. Barbosa, M. B. S. Dias, R. S. Turtelli, M. Atif, and R. Grossinger, "Magnetostriction of Fe–Cr and Fe–Cr–B Alloys," *IEEE Transactions on Magnetics*, vol. 52, pp. 1–4, May 2016.

7 Remarks

In this thesis, I, Alexander Benedikt Paulischin, performed all experiments and data analyses with the following exceptions:

- Martin Stückler performed the XRD measurements of specimens of the Fe-Cu system.

- Lukas Weissitsch performed the specimen fabrication, HPT deformation processes as well as the characterization of the microstructure (SEM investigations, hardness measurements and synchrotron measurements) of specimens of the Fe-Cr system.

- Stefan Wurster wrote the Scilab-scripts, which were used for the actuation of the electromagnet.

8 Appendix

8.1 Scilab scripts

Listing 8.1: Script for the first magnetostriction measurement concept.

```scilab
clear

warning('off')

// VERÄNDERN Anzahl von Messungen von B pro gehaltenem
    Elektromagnet-Strom, Einfluss auf Magnetfeld-Haltezeit
measurements=150

//Speicherverzeichnis
Verz="C:\Users\Wurster\Desktop\Scilab\Daten\";
//Speichern, Dateiname
Dateiname=input("Proben/Dateiname: ","string")

Zeit2=getdate();
ExportDate2=string([Zeit2(1),Zeit2(2),Zeit2(6),Zeit2(7),
    Zeit2(8),Zeit2(9),Zeit2(10)]);
Datei2=strcat([Verz,Dateiname,"_2_",ExportDate2,".txt"]);
fprintfMat(Datei2,[Zeit2(1),Zeit2(2),Zeit2(6),Zeit2(7),
    Zeit2(8),Zeit2(9),Zeit2(10)],"%lg",'Jahr Monat   Tag
    Stunde  Minute  Sekunde Millisekunde');

//Start Zeit
tic

//Start Kommunikation Elektromagnet
[status, deviceAddrs] = findAllInstruments()
[status, defaultRM] = viOpenDefaultRM()
```

```
,24  [status , idDevice] = viOpen(defaultRM ,deviceAddrs(3),
         viGetDefinition("VI_NULL"), viGetDefinition("VI_NULL"))

,26  //Start Kommunikation Gaussmeter
,27  Gauss=openserial(1,"9600,o,7,1","crlf")

,29  //angefahrene Stromwerte
,30  Stromschleife
         =[-0.214;0;0.25;0.5;1;1.5;2;3;4;5;6;7;8.5;10;14;19;24;
         30;36;42;49;56;64;72;81;90;100;110;120;150;175;200;175;
         150;120;110;100;90;81;72;64;56;49;42;36;30;24;19;14;10;
         8.5;7;6;5;4;3;2;1.5;1;0.5;0.25;0;-0.214]

,32  m=1

,34  for i=1:length(Stromschleife)

,36      //Strom aus [Stromschleife] einstellen
,37      Strom=Stromschleife(i)
,38      Strom=string(Strom)
,39      StromStr=strcat(["CUR=",Strom])
,40      [status ,count]=viWrite(idDevice ,StromStr)

,42      //Warten auf konstantes Magnetfeld
,43      B_wait1=100
,44      B_wait2=200

,46      ProgBar=progressionbar('Warten auf konstantes
             Magnetfeld ')
,47      progressionbar(ProgBar)

,49      sleep (5000)

,51      while abs(B_wait1-B_wait2)>0.00001

,53          writeserial(Gauss ,"RDGFIELD?"+ascii (10))
,54          sleep(1000)
```

```scilab
55         ausleseB=readserial(Gauss)
56         B_wait1=strtod(ausleseB)

58         writeserial(Gauss,"RDGFIELD?"+ascii(10))
59         sleep(1000)
60         ausleseB=readserial(Gauss)
61         B_wait2=strtod(ausleseB)

63     end

65     close(ProgBar)

67     for j=1:measurements

69         //Auslesen Zeit
70         t(m)=toc()

72         //Schreiben Wert aus [Stromschleife] für
             Speicherung
73         StromSchleifeSchleife(m)=Stromschleife(i)

75         writeserial(Gauss,"RDGFIELD?"+ascii(10))
76         sleep(250)

78         ausleseB=readserial(Gauss)
79         B(m)=strtod(ausleseB)

81         disp(j)

83         m=m+1

85     end

87 end

89 //Speichern ohne Temperatur
90 //Datei 1: Stromschleife, Magnetfeld
```

```
,91  Zeit=getdate();
,92  ExportDate=string([Zeit(1),Zeit(2),Zeit(6),Zeit(7),Zeit(8),
         Zeit(9),Zeit(10)]);
,93  Datei1=strcat([Verz,Dateiname,"_1_",ExportDate,".txt"]);
,94  fprintfMat(Datei1,[t,StromSchleifeSchleife,B],"%lg","Zeit [
         s]       I_Magnet [A]  mag.Feld [T]");

,96  //Schließen der Kommunikation
,97  //Elektromagnet
,98  viClose(idDevice)
,99  viClose(defaultRM)
```

Listing 8.2: Script for the first magnetostriction measurement concept for the Fe-Cr system.

```
,1   clear

,3   warning('off')

,5   // VERÄNDERN Anzahl von Messungen von B pro gehaltenem
         Elektromagnet-Strom, Einfluss auf Magnetfeld-Haltezeit
,6   measurements=150


,9   //Speicherverzeichnis
,10  Verz="C:\Users\Wurster\Desktop\Scilab\Daten\";
,11  //Speichern, Dateiname
,12  Dateiname=input("Proben/Dateiname: ","string")

,14  Zeit2=getdate();
,15  ExportDate2=string([Zeit2(1),Zeit2(2),Zeit2(6),Zeit2(7),
         Zeit2(8),Zeit2(9),Zeit2(10)]);
,16  Datei2=strcat([Verz,Dateiname,"_2_",ExportDate2,".txt"]);
,17  fprintfMat(Datei2,[Zeit2(1),Zeit2(2),Zeit2(6),Zeit2(7),
         Zeit2(8),Zeit2(9),Zeit2(10)],"%lg",'Jahr Monat   Tag
         Stunde  Minute  Sekunde Millisekunde');

,19  //Start Zeit
,20  tic

,22  //Start Kommunikation Elektromagnet
,23  [status, deviceAddrs] = findAllInstruments()
,24  [status, defaultRM] = viOpenDefaultRM()
,25  [status, idDevice] = viOpen(defaultRM,deviceAddrs(3),
         viGetDefinition("VI_NULL"), viGetDefinition("VI_NULL"))


,28  //Start Kommunikation Gaussmeter
,29  Gauss=openserial(1,"9600,o,7,1","crlf")
```

```scilab
,32   //Erste Stromschleife: Neukurve und retour auf Null-Feld
,33   //NUR DEN ERSTEN WERT ANPASSEN

,35   Stromschleife
          =[-0.080;0;0.5;1;1.75;2.5;4;6;8;10;14;20;24;30;36;42;49;
           56;64;72;81;90;100;120;150;200;150;120;100;90;81;72;64;
           56;49;42;36;30;24;20;14;10;8;6;4;2.5;1.75;1;0.5;0]

,37   //Stromschleife=[0]

,39   m=1

,41   for i=1:length(Stromschleife)

,43       //Strom aus [Stromschleife] einstellen
,44       Strom=Stromschleife(i)
,45       Strom=string(Strom)
,46       StromStr=strcat(["CUR=",Strom])
,47       [status,count]=viWrite(idDevice,StromStr)

,49       //Warten auf konstantes Magnetfeld
,50       B_wait1=100
,51       B_wait2=200

,53       ProgBar=progressionbar('Warten auf konstantes
              Magnetfeld')
,54       progressionbar(ProgBar)

,56       while abs(B_wait1-B_wait2)>0.00001

,58           writeserial(Gauss,"RDGFIELD?"+ascii(10))
,59           sleep(1000)
,60           ausleseB=readserial(Gauss)
,61           B_wait1=strtod(ausleseB)

,63           writeserial(Gauss,"RDGFIELD?"+ascii(10))
```

```scilab
,64          sleep (1000)
,65          ausleseB = readserial ( Gauss )
,66          B_wait2 = strtod ( ausleseB )


,68      end


,70      close ( ProgBar )


,72      for j =1: measurements


,74          // Auslesen Zeit
,75          t(m)= toc ()


,77          // Schreiben Wert aus [ Stromschleife ] für
                  Speicherung
,78          StromSchleifeSchleife (m)= Stromschleife (i)


,80          writeserial ( Gauss ," RDGFIELD ?"+ ascii (10) )
,81          sleep (250)


,83          ausleseB = readserial ( Gauss )
,84          B(m)= strtod ( ausleseB )


,86          disp (j)


,88          m=m+1


,90      end


,92  end


,94  // UMPOLUNG
,95  sleep (1000)
,96  // DC Off
,97  [ status , count ]= viWrite ( idDevice , 'DCP =0 ')
,98  sleep (2000)
,99  // Wechseln Polarität Positiv -->> Negativ
```

```scilab
,100  [status,count]=viWrite(idDevice,'POL=1')
,101  sleep(45000)
,102  //DC On
,103  [status,count]=viWrite(idDevice,'DCP=1')
,104  sleep(1000)

,106  //wegen Umpolung
,107  //Stromschleife=[200;0]

,109  Stromschleife
          =[0;0.5;1;1.75;2.5;4;6;8;10;14;20;24;30;36;42;49;56;64;
          72;81;90;100;120;150;200;150;120;100;90;81;72;64;56;49;
          42;36;30;24;20;14;10;8;6;4;2.5;1.75;1;0.5;0]

,111  Stromschleife=Stromschleife*(-1)

,113  for i=1:length(Stromschleife)

,115      //Strom aus [Stromschleife] einstellen
,116      Strom=Stromschleife(i)
,117      Strom=string(Strom)
,118      StromStr=strcat(["CUR=",Strom])
,119      [status,count]=viWrite(idDevice,StromStr)

,121      //Warten auf konstantes Magnetfeld
,122      B_wait1=100
,123      B_wait2=200

,125      ProgBar=progressionbar('Warten auf konstantes
              Magnetfeld')
,126      progressionbar(ProgBar)

,128      while abs(B_wait1-B_wait2)>0.00001

,130          writeserial(Gauss,"RDGFIELD?"+ascii(10))
,131          sleep(1000)
,132          ausleseB=readserial(Gauss)
```

```scilab
,133            B_wait1=strtod(ausleseB)

,135            writeserial(Gauss,"RDGFIELD?"+ascii(10))
,136            sleep(1000)
,137            ausleseB=readserial(Gauss)
,138            B_wait2=strtod(ausleseB)

,140        end

,142        close(ProgBar)

,144        for j=1:measurements

,146            //Auslesen Zeit
,147            t(m)=toc()

,149            //Schreiben Wert aus [Stromschleife] für
                    Speicherung
,150            StromSchleifeSchleife(m)=Stromschleife(i)

,152            writeserial(Gauss,"RDGFIELD?"+ascii(10))
,153            sleep(250)

,155            ausleseB=readserial(Gauss)
,156            B(m)=strtod(ausleseB)

,158            disp(j)

,160            m=m+1

,162        end

,164    end


,167 // Umpolung
,168 sleep(1000)
```

```
,169    //DC Off
,170    [status,count]=viWrite(idDevice,'DCP=0')
,171    sleep(2000)
,172    //Wechseln Polarität Negativ -->> Positiv
,173    [status,count]=viWrite(idDevice,'POL=0')
,174    sleep(45000)
,175    //DC On
,176    [status,count]=viWrite(idDevice,'DCP=1')
,177    sleep(1000)


,179    //neue Stromschleife, nur Hochfahren auf max.Feld
,180    Stromschleife
            =[0;0.5;1;1.75;2.5;4;6;8;10;14;20;24;30;36;42;49;56;64;
            72;81;90;100;120;150;200;0]


,182    for i=1:length(Stromschleife)


,184        //Strom aus [Stromschleife] einstellen
,185        Strom=Stromschleife(i)
,186        Strom=string(Strom)
,187        StromStr=strcat(["CUR=",Strom])
,188        [status,count]=viWrite(idDevice,StromStr)


,190        //Warten auf konstantes Magnetfeld
,191        B_wait1=100
,192        B_wait2=200


,194        ProgBar=progressionbar('Warten auf konstantes
                Magnetfeld')
,195        progressionbar(ProgBar)


,197        while abs(B_wait1-B_wait2)>0.00001


,199            writeserial(Gauss,"RDGFIELD?"+ascii(10))
,200            sleep(1000)
,201            ausleseB=readserial(Gauss)
,202            B_wait1=strtod(ausleseB)
```

```scilab
,204        writeserial(Gauss,"RDGFIELD?"+ascii(10))
,205        sleep(1000)
,206        ausleseB=readserial(Gauss)
,207        B_wait2=strtod(ausleseB)


,209    end


,211    close(ProgBar)


,213    for j=1:measurements


,215        //Auslesen Zeit
,216        t(m)=toc()


,218        //Schreiben Wert aus [Stromschleife] für
                Speicherung
,219        StromSchleifeSchleife(m)=Stromschleife(i)


,221        writeserial(Gauss,"RDGFIELD?"+ascii(10))
,222        sleep(250)


,224        ausleseB=readserial(Gauss)
,225        B(m)=strtod(ausleseB)


,227        disp(j)


,229        m=m+1


,231    end


,233 end



,236 //Speichern ohne Temperatur
,237 //Datei 1: Stromschleife, Magnetfeld
,238 Zeit=getdate();
```

```scilab
239  ExportDate=string([Zeit(1),Zeit(2),Zeit(6),Zeit(7),Zeit(8),
         Zeit(9),Zeit(10)]);
240  Datei1=strcat([Verz,Dateiname,"_1_",ExportDate,".txt"]);
241  fprintfMat(Datei1,[t,StromSchleifeSchleife,B],"%lg","Zeit [
         s]        I_Magnet [A]   mag.Feld [T]");


244  //Schließen der Kommunikation
245  //Elektromagnet
246  viClose(idDevice)
247  viClose(defaultRM)
```

Listing 8.3: Script for the second magnetostriction measurement concept.

```scilab
,2  clear

,4  warning('off')

,6  // VERÄNDERN Anzahl von Messungen von B pro gehaltenem
        Elektromagnet-Strom, Einfluss auf Magnetfeld-Haltezeit
,7  measurements=200


,10 //Speicherverzeichnis
,11 Verz="C:\Users\Wurster\Desktop\Scilab\Daten\";
,12 //Speichern, Dateiname
,13 Dateiname=input("Proben/Dateiname: ","string")

,15 Zeit2=getdate();
,16 ExportDate2=string([Zeit2(1),Zeit2(2),Zeit2(6),Zeit2(7),
        Zeit2(8),Zeit2(9),Zeit2(10)]);
,17 Datei2=strcat([Verz,Dateiname,"_2_",ExportDate2,".txt"]);
,18 fprintfMat(Datei2,[Zeit2(1),Zeit2(2),Zeit2(6),Zeit2(7),
        Zeit2(8),Zeit2(9),Zeit2(10)],"%lg",'Jahr Monat   Tag
        Stunde  Minute  Sekunde Millisekunde');

,20 //Start Zeit
,21 tic

,23 //Start Kommunikation Elektromagnet
,24 [status, deviceAddrs] = findAllInstruments()
,25 [status, defaultRM] = viOpenDefaultRM()
,26 [status, idDevice] = viOpen(defaultRM,deviceAddrs(3),
        viGetDefinition("VI_NULL"), viGetDefinition("VI_NULL"))


,29 //Start Kommunikation Gaussmeter
,30 Gauss=openserial(1,"9600,o,7,1","crlf")
```

```scilab
32  //Ein einzelner Wert für Erhalt eines konstanten
        Magnetfeldes, z.B. 2T
33  Stromschleife=120

35  m=1

37  for i=1:length(Stromschleife)

39      //Strom aus [Stromschleife] einstellen
40      Strom=Stromschleife(i)
41      Strom=string(Strom)
42      StromStr=strcat(["CUR=",Strom])
43      [status,count]=viWrite(idDevice,StromStr)

45      //Warten auf konstantes Magnetfeld
46      B_wait1=100
47      B_wait2=200

49      ProgBar=progressionbar('Warten auf konstantes
            Magnetfeld')
50      progressionbar(ProgBar)

52      sleep(5000)

54      while abs(B_wait1-B_wait2)>0.00001

56          writeserial(Gauss,"RDGFIELD?"+ascii(10))
57          sleep(1000)
58          ausleseB=readserial(Gauss)
59          B_wait1=strtod(ausleseB)

61          writeserial(Gauss,"RDGFIELD?"+ascii(10))
62          sleep(1000)
63          ausleseB=readserial(Gauss)
64          B_wait2=strtod(ausleseB)

66      end
```

```scilab
,68        close(ProgBar)

,70        Winkel=input("eingestellter Winkel [deg]: ")

,72        while Winkel<1000

,74            for j=1:measurements

,76                //Auslesen Zeit
,77                t(m)=toc()

,79                //Schreiben Wert aus [Stromschleife] für
                       Speicherung
,80                StromSchleifeSchleife(m)=Stromschleife(i)

,82                writeserial(Gauss,"RDGFIELD?"+ascii(10))
,83                sleep(250)

,85                ausleseB=readserial(Gauss)
,86                B(m)=strtod(ausleseB)

,88                SpeicherWinkel(m)=Winkel

,90                disp(j)

,92                m=m+1

,94            end

,96            Winkel=input("eingestellter Winkel [deg]: ")

,98        end

,100   end

,102   //Speichern
```

```
,103   //Datei 1: Stromschleife, Magnetfeld
,104   Zeit=getdate();
,105   ExportDate=string([Zeit(1),Zeit(2),Zeit(6),Zeit(7),Zeit(8),
           Zeit(9),Zeit(10)]);
,106   Datei1=strcat([Verz,Dateiname,"_1_",ExportDate,".txt"]);
,107   fprintfMat(Datei1,[t,StromSchleifeSchleife,B,SpeicherWinkel
           ],"%lg","Zeit [s]        I_Magnet [A]   mag.Feld [T]
           eingestellter Winkel [deg]");


,110   //Ausschalten Strom
,111   Strom=0
,112   Strom=string(Strom)
,113   StromStr=strcat(["CUR=",Strom])
,114   [status,count]=viWrite(idDevice,StromStr)


,117   //Schließen der Kommunikation
,118   //Elektromagnet
,119   viClose(idDevice)
,120   viClose(defaultRM)
```

8.2 MATLAB scripts

Listing 8.4: Script for the data evaluation of magnetostriction measurements of the first measurement concept.

```
 1  function [Messpunkte, Matrix, fit] =
        Auswertung_Temperaturkompensation(Steuerzeit,Magnetstrom
        ,Magnetfeld,Messzeit,Dehnung,Schrittweite,Offset,Breite,
        Messratenfaktor,StartoffsetD,Temperatur,StartoffsetT,
        AlphaProbeC1,AlphaProbeC2,C1,C2,AlphaReferenz,Dateiname,
        Diagrammname)

 3  %% Calculation of the thermal expansion coefficient

 5  AlphaDMS = 10.8;
 6  AlphaProbe = (AlphaProbeC1 * C1) + (AlphaProbeC2 * C2);
 7  AlphaProbe_neu = AlphaProbe - AlphaDMS;
 8  AlphaReferenz_neu = AlphaReferenz - AlphaDMS;

10  Alpha = AlphaProbe_neu - AlphaReferenz_neu;

12  %% Definition of variables

14  OffsetT = Offset;
15  BreiteT = Breite;
16  OffsetD = OffsetT * Messratenfaktor;
17  BreiteD = BreiteT * Messratenfaktor;

19  Laenge1 = length(Steuerzeit);
20  Messpunkte = Laenge1 / Schrittweite;
21  Laenge2 = length(Messzeit);
22  Laenge3 = length(Temperatur);
23  Tempzeit = (1:1:Laenge3);
24  Tempzeit = Tempzeit';

26  Matrix = zeros(Messpunkte,15);

28  Messzeit1 = Messzeit - StartoffsetD;
```

```matlab
Tempzeit1 = Tempzeit - StartoffsetT;

%% Calculation of the mean values of strain and temperature
    at each specimen orientation

a = 1;
b = Schrittweite;

    for k = 1:Messpunkte

        I_Vektor = Magnetstrom(a:b, 1);
        B_Vektor = Magnetfeld(a:b, 1);

        mean_I = mean(I_Vektor);
        mean_B = mean(B_Vektor);

        Matrix(k,1) = k;
        Matrix(k,2) = mean_I;
        Matrix(k,3) = mean_B;

        MatrixD = zeros(Laenge2,1);
        MatrixT = zeros(Laenge3,1);

        for l = 1:Laenge2

            Zeit = Steuerzeit(a,1);
            Diff = abs(Zeit - Messzeit1(l,1));
            MatrixD(l,1) = Diff;

        end

        for m = 1:Laenge3

            Zeit = Steuerzeit(a,1);
            DiffT = abs(Zeit - Tempzeit1(m,1));
            MatrixT(m,1) = DiffT;
```

```matlab
,65             end

,67             Minimum = min(MatrixD);
,68             Position = find(MatrixD == Minimum);

,70             MinimumT = min(MatrixT);
,71             PositionT = find(MatrixT == MinimumT);

,73             Beginn = Position + OffsetD;
,74             Ende = Position + OffsetD + BreiteD;

,76             BeginnT = PositionT + OffsetT;
,77             EndeT = PositionT + OffsetT + BreiteT;

,79             D_Vektor = Dehnung(Beginn:Ende,1);
,80             mean_D = mean(D_Vektor);
,81             stand_D = std(D_Vektor);

,83             T_Vektor = Temperatur(BeginnT:EndeT,1);
,84             mean_T = mean(T_Vektor);
,85             stand_T = std(T_Vektor);

,87             Matrix(k,4) = mean_D;
,88             Matrix(k,5) = stand_D;
,89             Matrix(k,6) = mean_T;
,90             Matrix(k,7) = stand_T;

,92             a = a + Schrittweite;
,93             b = b + Schrittweite;

,95         end

,97 x1 = Matrix(:,1);
,98 x2 = x1 - 1;

,100 VektorB = Matrix(:,3);
,101 VektorD = Matrix(:,4);
```

```matlab
Vektor_stab_D = Matrix(:,5);
VektorT = Matrix(:,6);
Vektor_stab_T = Matrix(:,7);


%% Temperature compensation


Vektor_deltaT = zeros(Messpunkte,1);
Vektor_deltaT3 = zeros(Messpunkte,1);


% First method of the temperature compensation


for n = 1:(Messpunkte-1)


    o = n + 1;


    Vektor_deltaT(o,1) = VektorT(o,1) - VektorT(n,1);


end


Vektor_deltaD = Vektor_deltaT * Alpha;


VektorD_Korr = VektorD - Vektor_deltaD;


Matrix(:,8) = Vektor_deltaT;
Matrix(:,9) = VektorD_Korr;


% Second method of the temperature compensation


fit = polyfit(x2, VektorT, 2);
c1 = fit (1,1);
c2 = fit (1,2);
d = fit (1,3);


T_curve = (c1 * (x2.^2)) + (c2 * x2) + d;


Vektor_deltaT2 = T_curve - d;
```

```
,139  Vektor_deltaD2 = Vektor_deltaT2 * Alpha ;

,141  VektorD_Korr_2 = VektorD - Vektor_deltaD2 ;

,143  Matrix (: ,10) = Vektor_deltaT2 ;
,144  Matrix (: ,11) = VektorD_Korr_2 ;

,146  % Thirt method of the temperature compensation

,148  for j =1: Messpunkte

,150      Vektor_deltaT3 (j ,1) = VektorT (j ,1) - VektorT (1 ,1) ;

,152  end

,154  Vektor_deltaD3 = Vektor_deltaT3 * Alpha ;

,156  VektorD_Korr_3 = VektorD - Vektor_deltaD3 ;

,158  Matrix (: ,12) = Vektor_deltaT3 ;
,159  Matrix (: ,13) = VektorD_Korr_3 ;

,161  %% Error estimation

,163  Vektor_stab_D2 = Vektor_stab_T * Alpha ;
,164  Vektor_stab_D3 = Vektor_stab_D + Vektor_stab_D2 ;
,165  Matrix (: ,14) = Vektor_stab_D2 ;
,166  Matrix (: ,15) = Vektor_stab_D3 ;

,168  %% Plots

,170  figure (1) ;

,172  subplot (2 ,3 ,1) ;
,173  errorbar ( VektorB , VektorD , Vektor_stab_D , '-b') ;
,174  set ( gca , 'FontSize' ,15) ;
,175  xlabel ('B [T] ') ;
```

```
176  ylabel('\lambda [\mum/m]');
177  grid on
178  grid minor
179  box on
180  title(Diagrammname);

182  subplot(2,3,2);
183  [hLine3] = plot([VektorB, VektorB, VektorB, VektorB], [
        VektorD, VektorD_Korr, VektorD_Korr_2, VektorD_Korr_3]);
184  set(gca,'FontSize',15);
185  title(Diagrammname);
186  xlabel('B [T]');
187  ylabel('\lambda [\mum/m]');
188  grid on;
189  grid minor;
190  box on;
191  hLine3(1,1).Marker = 'diamond';
192  hLine3(1,1).Color = [0 0 1];
193  hLine3(2,1).LineStyle = '-.';
194  hLine3(2,1).Color = [1 0 0];
195  hLine3(3,1).LineStyle = '-.';
196  hLine3(3,1).Marker = 'o';
197  hLine3(3,1).Color = [0 0.6 0];
198  hLine3(4,1).LineStyle = '-.';
199  hLine3(4,1).Marker = 'o';
200  hLine3(4,1).Color = [0 0 0];
201  legend('\lambda', '\lambda mit \DeltaT-Korrektur (Methode
        1)', '\lambda mit \DeltaT-Korrektur (Methode 2)', '\
        lambda mit \DeltaT-Korrektur (Methode 3)')

203  subplot(2,3,3);
204  plot(VektorB, Vektor_stab_D2, '-diamondb', VektorB,
        Vektor_stab_D3, '-diamondr');
205  set(gca,'FontSize',15);
206  grid on
207  grid minor
208  box on
```

```matlab
xlabel('B [T]');
ylabel('\Delta\lambda [\mum/m]');
title('Schwankungsbreite \lambda');
legend('Schwankungsbreite T','Schwankungsbreite T + \lambda
    ');

subplot(2,3,4);
errorbar(x1, VektorT, Vektor_stab_T, '-b');
hold on
plot(x1, T_curve, '--', 'Color', [0 0.6 0], 'Linewidth',
    1.5);
set(gca,'FontSize',15);
grid on
grid minor
box on
xlabel('Messpunkte');
ylabel('T [Â°C]');
title('Temperaturverlauf');
legend('Temperaturverlauf','Temperaturverlauf des Polynoms'
    );

subplot (2,3,(5:6));
colororder({'k','k'})
yyaxis left
set(gca,'FontSize',15);
plot(x1, VektorT, 'LineStyle', '-', 'Marker', 'diamond', '
    Color', [0 0 1]);
hold on;
plot(x1, T_curve, 'LineStyle', '--', 'Marker', 'none', '
    Color', [0 0.6 0]);
xlabel('Messpunkte');
ylabel('Temperatur [Â°C]');
title('Temperaturverlauf');
grid on;
grid minor;
box on;
yyaxis right
```

```
,241  plot(x1, Vektor_deltaT, 'LineStyle', ':', 'Marker', 'o', '
          Color', [1 0 0]);
,242  plot(x1, Vektor_deltaT3, 'Linestyle', ':', 'Marker', 'o', '
          Color', [0 0 0]);
,243  ylabel('\DeltaT [Â°C]');
,244  legend('Temperaturverlauf', 'Temperaturverlauf des Polynoms
          ', '\DeltaT-Verlauf (Methode 1)', '\DeltaT-Verlauf (
          Methode 3)');
,245  hold off;


,248  figure(2);

,250  subplot(2,2,1)
,251  plot(VektorB, VektorD, '-diamondb')
,252  set(gca,'FontSize',15);
,253  grid on
,254  grid minor
,255  box on
,256  xlabel('B [T]');
,257  ylabel('\lambda [\mum/m]');
,258  title('Messwert');

,260  subplot(2,2,2)
,261  plot(VektorB, VektorD_Korr, '-diamondb')
,262  set(gca,'FontSize',15);
,263  grid on
,264  grid minor
,265  box on
,266  xlabel('B [T]');
,267  ylabel('\lambda [\mum/m]');
,268  title('Temperaturkorrektur Methode 1');

,270  subplot(2,2,3)
,271  plot(VektorB, VektorD_Korr_2, '-diamondb')
,272  set(gca,'FontSize',15);
,273  grid on
```

```matlab
274  grid minor
275  box on
276  xlabel('B [T]');
277  ylabel('\lambda [\mum/m]');
278  title('Temperaturkorrektur Methode 2');

280  subplot(2,2,4)
281  plot(VektorB, VektorD_Korr_3, '-diamondb')
282  set(gca,'FontSize',15);
283  grid on
284  grid minor
285  box on
286  xlabel('B [T]');
287  ylabel('\lambda [\mum/m]');
288  title('Temperaturkorrektur Methode 3');


291  %% Data output

293  Name = [Dateiname '.xlsx'];

295  Text1 = 'Messpunkt';
296  Text2 = 'I';
297  Text3 = 'B';
298  Text4 = 'lambda';
299  Text5 = 'Stab_lambda';
300  Text6 = 'T';
301  Text7 = 'Stab_T';
302  Text8 = 'deltaT (Methode 1)';
303  Text9 = 'lambda deltaT (Methode 1)';
304  Text10 = 'deltaT (Methode 2)';
305  Text11 = 'lambda deltaT (Methode 2)';
306  Text12 = 'deltaT (Methode 3)';
307  Text13 = 'lambda deltaT (Methode 3)';
308  Text14 = 'Abweichung lambda';
309  Text15 = 'Abweichung lambda 2';
310  TextK1 = 'Berechneter therm. Ausdehnungskoeffizient';
```

```
311  TextF1 = 'Polynomkoeffizienten';
312  TextF2 = 'c1';
313  TextF3 = 'c2';
314  TextF4 = 'd';

316  TextE1 = '[a.u.]';
317  TextE2 = '[A]';
318  TextE3 = '[T]';
319  TextE4 = '[microm/m]';
320  TextE5 = '[Â°C]';
321  TextE6 = '10E-6 [1/K]';

323  writematrix(Diagrammname, Name, 'Sheet',1,'Range','A1');
324  writematrix(TextK1, Name, 'Sheet',1,'Range','A3');
325  writematrix(Alpha, Name, 'Sheet',1,'Range','B3');
326  writematrix(TextE6, Name, 'Sheet',1,'Range','C3');
327  writematrix(TextF1, Name, 'Sheet',1,'Range','A5');
328  writematrix(TextF2, Name, 'Sheet',1,'Range','A6');
329  writematrix(TextF3, Name, 'Sheet',1,'Range','A7');
330  writematrix(TextF4, Name, 'Sheet',1,'Range','A8');
331  writematrix(c1, Name, 'Sheet',1,'Range','B6');
332  writematrix(c2, Name, 'Sheet',1,'Range','B7');
333  writematrix(d, Name, 'Sheet',1,'Range','B8');
334  writematrix(Text1, Name, 'Sheet',1,'Range','A10');
335  writematrix(Text2, Name, 'Sheet',1,'Range','B10');
336  writematrix(Text3, Name, 'Sheet',1,'Range','C10');
337  writematrix(Text4, Name, 'Sheet',1,'Range','D10');
338  writematrix(Text5, Name, 'Sheet',1,'Range','E10');
339  writematrix(Text6, Name, 'Sheet',1,'Range','F10');
340  writematrix(Text7, Name, 'Sheet',1,'Range','G10');
341  writematrix(Text8, Name, 'Sheet',1,'Range','H10');
342  writematrix(Text9, Name, 'Sheet',1,'Range','I10');
343  writematrix(Text10, Name, 'Sheet',1,'Range','J10');
344  writematrix(Text11, Name, 'Sheet',1,'Range','K10');
345  writematrix(Text12, Name, 'Sheet',1,'Range','L10');
346  writematrix(Text13, Name, 'Sheet',1,'Range','M10');
347  writematrix(Text14, Name, 'Sheet',1,'Range','N10');
```

```matlab
writematrix(Text15, Name, 'Sheet',1,'Range','O10');
writematrix(TextE1, Name, 'Sheet',1,'Range','A11');
writematrix(TextE2, Name, 'Sheet',1,'Range','B11');
writematrix(TextE3, Name, 'Sheet',1,'Range','C11');
writematrix(TextE4, Name, 'Sheet',1,'Range','D11');
writematrix(TextE4, Name, 'Sheet',1,'Range','E11');
writematrix(TextE5, Name, 'Sheet',1,'Range','F11');
writematrix(TextE5, Name, 'Sheet',1,'Range','G11');
writematrix(TextE5, Name, 'Sheet',1,'Range','H11');
writematrix(TextE4, Name, 'Sheet',1,'Range','I11');
writematrix(TextE5, Name, 'Sheet',1,'Range','J11');
writematrix(TextE4, Name, 'Sheet',1,'Range','K11');
writematrix(TextE5, Name, 'Sheet',1,'Range','L11');
writematrix(TextE4, Name, 'Sheet',1,'Range','M11');
writematrix(TextE4, Name, 'Sheet',1,'Range','N11');
writematrix(TextE4, Name, 'Sheet',1,'Range','O11');
writematrix (Matrix, Name, 'Sheet',1,'Range','A12');


end
```

Listing 8.5: Script for the data evaluation of magnetostriction measurements of the second measurement concept.

```matlab
function [Messpunkte, Matrix] = Auswertung_Orientierung(
    Steuerzeit, Magnetstrom, Magnetfeld, Winkel, Messzeit,
    Dehnung, Schrittweite, Offset, Breite, Messratenfaktor,
    StartoffsetD, Temperatur, StartoffsetT,AlphaProbeC1,
    AlphaProbeC2,C1,C2,AlphaReferenz, Dateiname,
    Diagrammname)

%% Calculation of the thermal expansion coefficients

AlphaDMS = 10.8;
AlphaProbe = (AlphaProbeC1 * C1) + (AlphaProbeC2 * C2);
AlphaProbe_neu = AlphaProbe - AlphaDMS;
AlphaReferenz_neu = AlphaReferenz - AlphaDMS;

Alpha = AlphaProbe_neu - AlphaReferenz_neu;

%% definition of variables

OffsetT = Offset;
BreiteT = Breite;
OffsetD = OffsetT * Messratenfaktor;
BreiteD = BreiteT * Messratenfaktor;

Laenge1 = length(Steuerzeit);
Messpunkte = Laenge1 / Schrittweite;
Laenge2 = length(Messzeit);
Laenge3 = length(Temperatur);
Tempzeit = (1:1:Laenge3);
Tempzeit = Tempzeit';

Matrix = zeros(Messpunkte, 16);

Messzeit1 = Messzeit - StartoffsetD;
Tempzeit1 = Tempzeit - StartoffsetT;
```

```
,31  %% Calculation of the mean values of strain and temperature
         at each specimen orientation

,33  a = 1;
,34  b = Schrittweite;

,36      for k = 1:Messpunkte

,38          I_Vektor = Magnetstrom(a:b,1);
,39          B_Vektor = Magnetfeld(a:b,1);
,40          W_Vektor = Winkel(a:b,1);

,42          mean_I = mean(I_Vektor);
,43          mean_B = mean(B_Vektor);
,44          mean_W = mean(W_Vektor);

,46          Matrix(k,1) = k;
,47          Matrix(k,2) = mean_I;
,48          Matrix(k,3) = mean_B;
,49          Matrix(k,4) = mean_W;
,50          MatrixD = zeros(Laenge2,1);
,51          MatrixT = zeros(Laenge3,1);

,53          for l = 1:Laenge2

,55              Zeit = Steuerzeit(a,1);
,56              Diff = abs(Zeit - Messzeit1(l,1));
,57              MatrixD(l,1) = Diff;

,59          end

,61          for m = 1:Laenge3

,63              Zeit = Steuerzeit(a,1);
,64              DiffT = abs(Zeit - Tempzeit1(m,1));
,65              MatrixT(m,1) = DiffT;
```

```
,67             end

,69             Minimum = min(MatrixD);
,70             Position = find(MatrixD == Minimum);

,72             MinimumT = min(MatrixT);
,73             PositionT = find(MatrixT == MinimumT);

,75             Beginn = Position + OffsetD;
,76             Ende = Position + OffsetD + BreiteD;

,78             BeginnT = PositionT + OffsetT;
,79             EndeT = PositionT + OffsetT + BreiteT;

,81             D_Vektor = Dehnung(Beginn:Ende,1);
,82             mean_D = mean(D_Vektor);
,83             stand_D = std(D_Vektor);

,85             T_Vektor = Temperatur(BeginnT:EndeT,1);
,86             mean_T = mean(T_Vektor);
,87             stand_T = std(T_Vektor);

,89             Matrix(k,5) = mean_D;
,90             Matrix(k,6) = stand_D;
,91             Matrix(k,7) = mean_T;
,92             Matrix(k,8) = stand_T;

,94             a = a + Schrittweite;
,95             b = b + Schrittweite;

,97         end

,99  x1 = Matrix(:,1);
,100 x2 = x1 - 1;

,102 VektorW = Matrix(:,4);
,103 VektorD = Matrix(:,5);
```

```matlab
,104  Vektor_stab_D = Matrix(:,6);
,105  VektorT = Matrix(:,7);
,106  Vektor_stab_T = Matrix(:,8);

,108  %% Temperature compensation

,110  Vektor_deltaT = zeros(Messpunkte,1);
,111  Vektor_deltaT3 = zeros(Messpunkte,1);

,113  % First method of the temperature compensation

,115  for n = 1:(Messpunkte-1)

,117      o = n + 1;

,119      Vektor_deltaT(o,1) = VektorT(o,1) - VektorT(n,1);

,121  end

,123  Vektor_deltaD = Vektor_deltaT * Alpha;

,125  VektorD_Korr = VektorD - Vektor_deltaD;

,127  Matrix(:,9) = Vektor_deltaT;
,128  Matrix(:,10) = VektorD_Korr;

,130  % Second method of the temperature compensation

,132  fit = polyfit(x2, VektorT, 2);
,133  c1 = fit (1,1);
,134  c2 = fit (1,2);
,135  d = fit (1,3);

,137  T_curve = (c1 * (x2.^2)) + (c2 * x2) + d;

,139  Vektor_deltaT2 = T_curve - d;
```

```
,141   Vektor_deltaD2 = Vektor_deltaT2 * Alpha;

,143   VektorD_Korr_2 = VektorD - Vektor_deltaD2;

,145   Matrix(:,11) = Vektor_deltaT2;
,146   Matrix(:,12) = VektorD_Korr_2;

,148   % Third method of the temperature compensation

,150   for j=1:Messpunkte

,152       Vektor_deltaT3(j,1) = VektorT(j,1) - VektorT(1,1);

,154   end

,156   Vektor_deltaD3 = Vektor_deltaT3 * Alpha;

,158   VektorD_Korr_3 = VektorD - Vektor_deltaD3;

,160   Matrix(:,13) = Vektor_deltaT3;
,161   Matrix(:,14) = VektorD_Korr_3;

,163   %% Error estimation

,165   Vektor_stab_D2 = Vektor_stab_T * Alpha;
,166   Vektor_stab_D3 = Vektor_stab_D + Vektor_stab_D2;
,167   Matrix(:,15) = Vektor_stab_D2;
,168   Matrix(:,16) = Vektor_stab_D3;

,170   %% Plots

,172   figure(1);

,174   subplot(2,3,1);
,175   errorbar(VektorW, VektorD, Vektor_stab_D, '-b');
,176   set(gca,'FontSize',15);
,177   xlabel('Winkel [Â°]');
```

```matlab
178  ylabel('\lambda [\mum/m]');
179  grid on
180  grid minor
181  box on
182  title(Diagrammname);

184  subplot(2,3,2);
185  [hLine3] = plot([VektorW, VektorW, VektorW, VektorW], [
         VektorD, VektorD_Korr, VektorD_Korr_2, VektorD_Korr_3]);
186  set(gca,'FontSize',15);title(Diagrammname);
187  xlabel('Winkel [°]');
188  ylabel('\lambda [\mum/m]');
189  grid on;
190  grid minor;
191  box on;
192  hLine3(1,1).Marker = 'diamond';
193  hLine3(1,1).Color = [0 0 1];
194  hLine3(2,1).LineStyle = '-.';
195  hLine3(2,1).Color = [1 0 0];
196  hLine3(3,1).LineStyle = '-.';
197  hLine3(3,1).Marker = 'o';
198  hLine3(3,1).Color = [0 0.7 0];
199  hLine3(4,1).LineStyle = '-.';
200  hLine3(4,1).Marker = 'o';
201  hLine3(4,1).Color = [0 0 0];
202  legend('\lambda', '\lambda mit \DeltaT-Korrektur (Methode
         1)', '\lambda mit \DeltaT-Korrektur (Methode 2)', '\
         lambda mit \DeltaT-Korrektur (Methode 3)')

204  subplot(2,3,3);
205  plot(VektorW, Vektor_stab_D2, '-diamondb', VektorW,
         Vektor_stab_D3, '-diamondr');
206  set(gca,'FontSize',15);
207  grid on
208  grid minor
209  box on
210  xlabel('Winkel [°]');
```

```
211  ylabel('\lambda [\mum/m]');
212  title('Schwankungsbreite \lambda');
213  legend('Schwankungsbreite T','Schwankungsbreite T + \lambda
        ');


215  subplot(2,3,4);
216  errorbar(x1, VektorT, Vektor_stab_T, '-b');
217  hold on
218  plot(x1, T_curve, '--', 'Color', [0 0.7 0], 'Linewidth',
        1.5);
219  set(gca,'FontSize',15);
220  grid on
221  grid minor
222  box on
223  xlabel('Messpunkte');
224  ylabel('T [Â°C]');
225  title('Temperaturverlauf');
226  legend('Temperaturverlauf','Temperaturverlauf des Polynoms'
        );


228  subplot (2,3,(5:6));
229  colororder({'k','k'})
230  yyaxis left
231  set(gca,'FontSize',15);
232  plot(x1, VektorT, 'LineStyle', '-', 'Marker', 'diamond', '
        Color', [0 0 1]);
233  hold on;
234  plot(x1, T_curve, 'LineStyle', '--', 'Marker', 'none', '
        Color', [0 0.7 0]);
235  xlabel('Messpunkte');
236  ylabel('Temperatur [Â°C]');
237  title('Temperaturverlauf');
238  grid on;
239  grid minor;
240  box on;
241  yyaxis right
242  plot(x1, Vektor_deltaT, 'LineStyle', ':', 'Marker', 'o', '
```

```
      Color', [1 0 0]);
243  plot(x1, Vektor_deltaT3, 'Linestyle', ':', 'Marker', 'o', '
      Color', [0 0 0]);
244  ylabel('\DeltaT [Â°C]');
245  legend('Temperaturverlauf', 'Temperaturverlauf des Polynoms
      ', '\DeltaT-Verlauf (Methode 1)', '\DeltaT-Verlauf (
      Methode 3)');
246  hold off;

248  figure(2);

250  subplot(2,2,1)
251  plot(VektorW, VektorD, '-diamondb')
252  set(gca,'FontSize',15);
253  grid on
254  grid minor
255  box on
256  xlabel('Winkel [Â°]');
257  ylabel('\lambda [\mum/m]');
258  title('Messwert');

260  subplot(2,2,2)
261  plot(VektorW, VektorD_Korr, '-diamondb')
262  set(gca,'FontSize',15);
263  grid on
264  grid minor
265  box on
266  xlabel('Winkel [Â°]');
267  ylabel('\lambda [\mum/m]');
268  title('Temperaturkorrektur Methode 1');

270  subplot(2,2,3)
271  plot(VektorW, VektorD_Korr_2, '-diamondb')
272  set(gca,'FontSize',15);
273  grid on
274  grid minor
275  box on
```

```matlab
276  xlabel('Winkel [°]');
277  ylabel('\lambda [\mum/m]');
278  title('Temperaturkorrektur Methode 2');

280  subplot(2,2,4)
281  plot(VektorW, VektorD_Korr_3, '-diamondb')
282  set(gca,'FontSize',15);
283  grid on
284  grid minor
285  box on
286  xlabel('Winkel [°]');
287  ylabel('\lambda [\mum/m]');
288  title('Temperaturkorrektur Methode 3');

290  %% Data output

292  Name = [Dateiname '.xlsx'];

294  Text1 = 'Messpunkt';
295  Text2 = 'I';
296  Text3 = 'B';
297  Text4 = 'Winkel';
298  Text5 = 'lambda';
299  Text6 = 'Stab_lambda';
300  Text7 = 'T';
301  Text8 = 'Stab_T';
302  Text9 = 'deltaT (Methode 1)';
303  Text10 = 'lambda deltaT (Methode 1)';
304  Text11 = 'deltaT (Methode 2)';
305  Text12 = 'lambda deltaT (Methode 2)';
306  Text13 = 'deltaT (Methode 3)';
307  Text14 = 'lambda deltaT (Methode 3)';
308  Text15 = 'Abweichung lambda';
309  Text16 = 'Abweichung lambda 2';
310  TextK1 = 'Berechneter therm. Ausdehnungskoeffizient';
311  TextF1 = 'Polynomkoeffizienten';
312  TextF2 = 'c1';
```

```
313  TextF3 = 'c2';
314  TextF4 = 'd';

316  TextE1 = '[a.u.]';
317  TextE2 = '[A]';
318  TextE3 = '[T]';
319  TextE4 = '[Â°]';
320  TextE5 = '[microm/m]';
321  TextE6 = '[Â°C]';
322  TextE7 = '10E-6 [1/K]';

324  writematrix(Diagrammname, Name, 'Sheet',1,'Range','A1');
325  writematrix(TextK1, Name, 'Sheet',1,'Range','A3');
326  writematrix(Alpha, Name, 'Sheet',1,'Range','B3');
327  writematrix(TextE7, Name, 'Sheet',1,'Range','C3');
328  writematrix(TextF1, Name, 'Sheet',1,'Range','A5');
329  writematrix(TextF2, Name, 'Sheet',1,'Range','A6');
330  writematrix(TextF3, Name, 'Sheet',1,'Range','A7');
331  writematrix(TextF4, Name, 'Sheet',1,'Range','A8');
332  writematrix(c1, Name, 'Sheet',1,'Range','B6');
333  writematrix(c2, Name, 'Sheet',1,'Range','B7');
334  writematrix(d, Name, 'Sheet',1,'Range','B8');
335  writematrix(Text1, Name, 'Sheet',1,'Range','A10');
336  writematrix(Text2, Name, 'Sheet',1,'Range','B10');
337  writematrix(Text3, Name, 'Sheet',1,'Range','C10');
338  writematrix(Text4, Name, 'Sheet',1,'Range','D10');
339  writematrix(Text5, Name, 'Sheet',1,'Range','E10');
340  writematrix(Text6, Name, 'Sheet',1,'Range','F10');
341  writematrix(Text7, Name, 'Sheet',1,'Range','G10');
342  writematrix(Text8, Name, 'Sheet',1,'Range','H10');
343  writematrix(Text9, Name, 'Sheet',1,'Range','I10');
344  writematrix(Text10, Name, 'Sheet',1,'Range','J10');
345  writematrix(Text11, Name, 'Sheet',1,'Range','K10');
346  writematrix(Text12, Name, 'Sheet',1,'Range','L10');
347  writematrix(Text13, Name, 'Sheet',1,'Range','M10');
348  writematrix(Text14, Name, 'Sheet',1,'Range','N10');
349  writematrix(Text15, Name, 'Sheet',1,'Range','O10');
```

```matlab
writematrix(Text16, Name, 'Sheet',1,'Range','P10');
writematrix(TextE1, Name, 'Sheet',1,'Range','A11');
writematrix(TextE2, Name, 'Sheet',1,'Range','B11');
writematrix(TextE3, Name, 'Sheet',1,'Range','C11');
writematrix(TextE4, Name, 'Sheet',1,'Range','D11');
writematrix(TextE5, Name, 'Sheet',1,'Range','E11');
writematrix(TextE5, Name, 'Sheet',1,'Range','F11');
writematrix(TextE6, Name, 'Sheet',1,'Range','G11');
writematrix(TextE6, Name, 'Sheet',1,'Range','H11');
writematrix(TextE6, Name, 'Sheet',1,'Range','I11');
writematrix(TextE5, Name, 'Sheet',1,'Range','J11');
writematrix(TextE6, Name, 'Sheet',1,'Range','K11');
writematrix(TextE5, Name, 'Sheet',1,'Range','L11');
writematrix(TextE6, Name, 'Sheet',1,'Range','M11');
writematrix(TextE5, Name, 'Sheet',1,'Range','N11');
writematrix(TextE5, Name, 'Sheet',1,'Range','O11');
writematrix(TextE5, Name, 'Sheet',1,'Range','P11');
writematrix (Matrix, Name, 'Sheet',1,'Range','A12');


end
```